Molecular Dynamics Simulations of Membranes and Membrane Proteins

A DISSERTATION
SUBMITTED TO THE FACULTY OF THE GRADUATE SCHOOL
OF THE UNIVERSITY OF MINNESOTA
BY

Jason David Perlmutter

IN PARTIAL FULFILLMENT OF THE REQUIREMENTS
FOR THE DEGREE OF
DOCTOR OF PHILOSOPHY

Dr. Jonathan N. Sachs, Adviser

July 2011

Acknowledgements

I would like to thank my advisor, Dr. Jonathan Sachs, for all of his guidance, encouragement, and inspiration. Without his patient support this thesis would not have been possible. Thanks are also in order to my labmates: Christopher Valley, William Drasler, Anthony Braun, Andrew Lewis, and Deepti Mudaliar, for the years of insights and stimulating discussions. I am grateful for all the support my family has given me, and I thank my parents and brother, as well as my wife, Melissa, to whom I dedicate this thesis.

Abstract

Membranes composed of a lipid bilayer and embedded proteins are ubiquitous in nature. They form the barrier which demarcates every cell from its environment and separates the distinct organelles within eukaryotic cells, implicating membranes in a wide range of biological processes. The function of membranes and membrane proteins are determined by their structure, and the central focus of this thesis is the use of computational molecular dynamics simulations to study experimentally inaccessible details of membrane structure. Firstly, we have simulated ternary lipid bilayers containing steroids with a range of headgroup hydrophobicities, observing a correlation between the membrane lateral organization and the orientation of the steroid. Based on these results we suggest a general framework to distinguish previously identified steroid domain promoters and inhibitors. Secondly, we investigate the role of interleaflet coupling in membrane structure. This includes describing a compositional dependence to the interleaflet organization of phase separated membranes, as well as investigating structural perturbations due to interleaflet differences in composition. Thirdly, we demonstrate a strategy for obtaining experimental verification through low angle X-ray scattering and discuss its potential application to complex phase separated mixtures. The second focus of this thesis is considering how the structural features of membranes affect the behavior of membrane proteins. The membrane protein α-Synuclein is of wide interest due to its association with Parkinson's Disease, but its physiological function remains unknown. A third focus of this thesis is the structure of membrane-mimetics, such as detergent micelles and amphipathic polymers, which are commonly used for the stabilization of membrane proteins. Their potential distinct influence on protein behavior currently remains an unresolved hindrance to experimental characterization. The simulations presented herein demonstrate a distinct effect of membrane curvature on α-Synuclein behavior and suggest a potential role in regulating vesicle fusion. Collectively, these simulations of model systems offer insight into the fundamental features which determine the behavior of complex biological membranes.

Table of Contents

List of Tables

List of Figures

1 Introduction

Membranes are ubiquitous in nature, as all cells are surrounded by a membrane and every eukaryotic cell contains many intra-cellular membranes. Therefore, all biological functions that involve communication between the cell and its environment or between different compartments of the cell necessarily involve membranes. This includes a diverse range of activities such as signal transduction, intra-cellular trafficking, endocytosis, and viral infection. In these processes the membrane is not just a passive platform for biology, but rather contains a precise composition and structure ostensibly optimized to promote functionality.

The lipid composition of a membrane is highly specific and varies between membranes in different organisms, membranes in different cells of the same organism, and even between different membranes of the same cell [1-3]. It is estimated that in eukaryotes 5% of genes are associated with lipid synthesis and regulation, and that a single cell may contain thousands of different lipids [1, 4, 5]. The emphasis placed on lipid compositional specificity strongly suggests its importance.

The lipid composition determines the structure, and accordingly the function, of a membrane. Broadly, all lipids contain a polar headgroup and a non-polar tail region. Bilayers and related structures form because the hydrophobic regions of the lipids are driven away from water while the polar regions interact favorably with water. However, as mentioned above, there are thousands of different lipids, each with a distinct chemical structure. These differences in lipid chemical structure determine the structure of the bilayer. For example, a bilayer containing lipids with longer hydrocarbon tails will be thicker (in the axis normal to the bilayer plane) than a bilayer containing lipids with shorter hydrocarbon tails [6]. Changes in bilayer structure in turn affect the function of the membrane; for example, thicker bilayers tend to be less permeable and are thought to have a larger energetic resistance to budding and fusion [7, 8].

The structure of the bilayer also determines the structure and function of membrane – membrane protein complexes. It well known that the structure and function of proteins are dependent on their environment, and the importance of water for determining the structure of soluble proteins is well recognized [9]. However, the

membrane is a considerably more complex environment, and numerous structural features of the membrane have been demonstrated to affect protein structure and function, including membrane thickness, fluidity, charge, curvature, and phase [10-12]. Therefore, a detailed characterization of the membrane environment is prerequisite to understanding the structure of membrane proteins,

In order to investigate the structure of membranes and membrane proteins, this thesis will make use of model systems. Biological membranes are heterogeneous mixtures containing potentially thousands of different lipids, densely populated with integral and peripheral membrane proteins [1, 13, 14]. Therefore, simplified model systems, such as purified lipid vesicles or bilayers, are used to understand how different components interact. In this thesis there is a careful progression from very simple models (such as used in Chapter 2), to models of greater complexity (such as in Chapter 4), in accordance with the larger goal of building towards the intricacy of biological systems. Furthermore, this thesis makes use of computational molecular modeling, a field which has grown markedly in the last decade with increases in computational power, allowing new insight into the structure and dynamics of molecular systems [15-19]. Maintaining a connection between the computational models and experimental systems is vital and is the focus of Chapter 2.

The outline for this thesis is as follows: the remainder of this chapter provides a brief introduction to the essential concepts of membrane and membrane protein biophysics and the modeling techniques to be used. The body of the thesis is then split into three sections, with the overarching theme being the structure of membranes and the potential effects of membrane structure on protein structure. The first section of the thesis (Section I) characterizes the structure of lipid bilayers, starting with the thickness of a simple, single component bilayer (Chapter 2), and progressing onwards to more complicated features like lateral heterogeneity (Chapter 3), asymmetry, and curvature (Chapter 4). Section II then investigates the relationship between membrane structure and membrane protein structure; specifically the effect of membrane curvature (a focus of Chapter 4) on the structure and dynamics of the protein α-Synuclein. The last section

expands the scope to include the effect of membrane-mimetics on membrane proteins, including detergent micelles (used in Section II) and amphipathic polymers (Section III).

1.1 Bilayer Thickness and Hydrophobic Mismatch

The thickness of a bilayer is an important feature when considering its interaction with other molecules. The formation of membranes is motivated by the hydrophobic effect, and interaction between hydrophobic and hydrophilic moieties confers a penalty to the free energy. Minimizing this interaction becomes more difficult in cases where the hydrophobic lengths of the components,either lipids or membrane proteins, are unequal. Figure 1-1 illustrates some of the possible ways through which a mismatch can be resolved [20]. The relative free energy penalty for each of these structural adaptations appears to be sensitive to the specific composition of the system, making it difficult to predict how a mixture might behave.

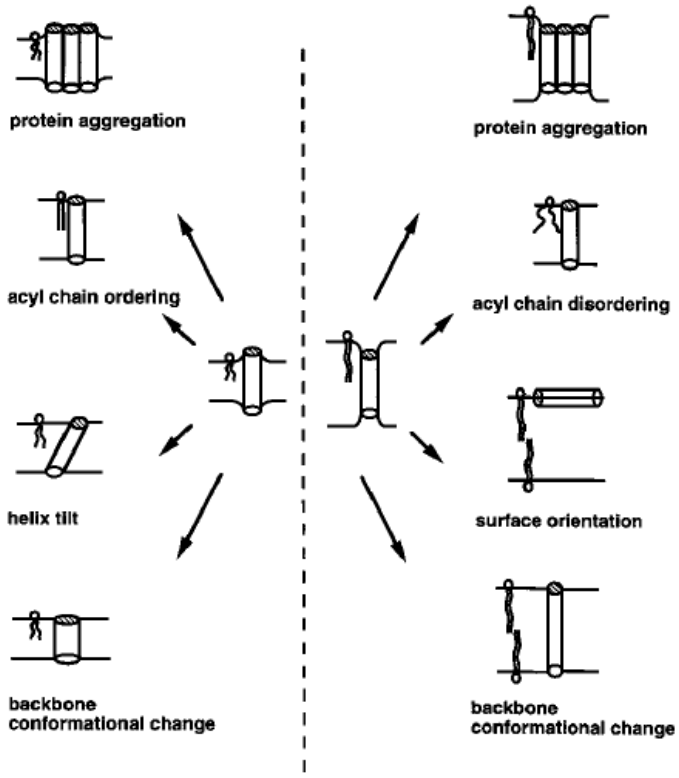

Figure 1-1 Hydrophobic Mismatch - Possible structural affects caused by hydrophobic mismatch (taken from [20]).

For mixtures of lipids with different thicknesses, structural adaptations include ordering (thickening), disordering (thinning), as well as changes in tilt. It is also possible that a mixture of lipids will laterally separate such that lipids with similar thicknesses co-localize (discussed further in the section 1.2).

For mixtures containing proteins, the structural changes induced by hydrophobic mismatch can have functional repercussions [11, 20, 21]. One example is that membrane proteins can preferentially localize to membranes which have a matching hydrophobic thickness [2, 22]. Alternatively, mismatch can be resolved through protein aggregation/oligomerization [23] or conformational changes [24]. These changes in structure can alter the function of the protein, as demonstrated through changes in enzymatic activity or rate of transport for a variety of membrane proteins [11]. These examples illustrate how a relatively simple structural feature, in this case membrane thickness, becomes more complicated in the case of mixtures and can ultimately affect functionality in ways which are difficult to predict, providing a role for computational molecular modeling. Characterizing the thicknesses of lipid bilayers and comparing computational and experimental models is the focus of Chapter 2.

1.2 Lipid Bilayer Phase Behavior and the Lipid Raft Hypothesis

An important idea in membrane biophysics today is that within biological membranes, regions of distinct phase form and recruit certain membrane proteins. Lipids are able to adopt a wide range of phases; however, the most important phases, when discussing biological membranes, are those categorized as either solid or liquid phases [1]. Solid phases are characterized as more ordered, more tightly packed, and with a lower degree of dynamic flexibility compared to liquid phases. The transition temperature (Tm) between the two depends on the lipid chemical structure, specifically the hydrocarbon chain length and degree of unsaturation. Depending on these properties, lipids can have Tm values above and below physiological temperature, though it is thought that biological membranes are primarily in the liquid phase [1].

A more recent observation is the existence of two distinct liquid phases, the liquid-disordered (L_d) and liquid-ordered (L_o) phases. The L_o phase is only formed by mixtures of lipid and cholesterol (typically above ~10-20% mol cholesterol). The L_o

phase is characterized by a slightly larger degree of order, including increased bilayer thickness, decreased permeability, and slower dynamics, though it is closer to the L_d phase than the solid phase.

Experiments mapping the phase diagrams of lipid mixtures have often found co-existence regions, where two distinct phases are in equilibrium. For binary lipid mixtures, solid-liquid co-existence has been thoroughly characterized [25, 26]. However, the more recent and intriguing observation is co-existence between the two liquid phases. In ternary mixtures, cholesterol will co-localize with lipids containing saturated hydrocarbon tails and form L_o regions, distinct from the lipids containing unsaturations in their hydrocarbon tails, which form L_d regions. Figure 1-2 presents a ternary phase diagram, in particular showing the co-existence between the L_d and L_o phases [27]. This was determined using fluorescent microscopy, fluorescence resonance energy transfer (FRET), and wide angle X-ray scattering, and is broadly in agreement with similar ternary mixtures [28-31].

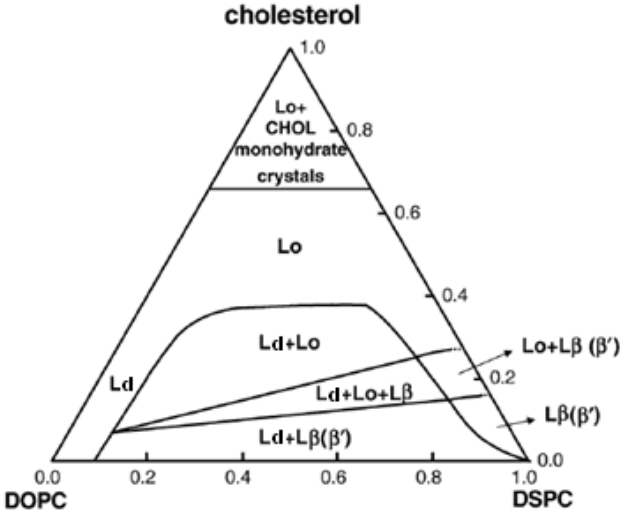

Figure 1-2 - Ternary Phase Diagram – Phase diagram for a ternary mixture of unsaturated lipid (DOPC), saturated lipid (DSPC) and cholesterol. Note, Lβ and Lβ' are solid phases (taken from [32]).

The interactions that lead cholesterol to preferentially associate with saturated lipids and promote the liquid-ordered phase remain unclear [33, 34]. A number of potential mechanisms have been suggestions, including the "umbrella effect" [35, 36], the formation of condensed complexes with defined stoichiometry [37, 38], perhaps related to a specific

hydrogen bonding pattern [36, 39], differences between the two sides of the cholesterol molecule [40], and differences in cholesterol orientation [41-43]. In general, it is thought that cholesterol interacts favorably with lipids with saturated chains, and that the relative rigidity of the cholesterol molecule confers an increase in order in the neighboring lipids. The lipid – cholesterol interactions that favor formation of the L_o phase is the subject of Chapter 3.

The lipid raft hypothesis states that biological membranes contain nanometer scale lateral heterogeneity in composition and structure [44], in contrast to the classic fluid mosaic model [45]. It is thought that small domains of L_o phase form in the membrane, serving as enrichment points for certain membrane proteins, promoting protein co-localization and functionality. This is supported by model studies, such as the phase diagram in Figure 1-2, and though the evidence from biological systems is tantalizing, this remains a controversial hypothesis.

Observation of phase separation in model systems is complicated by the range of sizes observed during domain formation. Earlier examples of liquid-liquid phase separation were observed using fluorescent microscopy on the macroscopic size scale (>200nm) [46]; however, rafts of this size were not detected in cellular membranes. More recent studies in model bilayers using FRET, AFM, and NMR have identified L_o domains on the size scale of nanometers and tens of nanometers (or ~tens – hundreds of lipids) [47-52]. The size of the L_o domains is dependent on the lipid composition [29], and specifically the magnitude of the line tension between neighboring phases. Where line tension is low, a larger interface (many small domains rather than one large domain) is possible, though it is unclear what force acts opposite line tension (though entropy, curvature, electrostatic repulsion, and other phenomenon have been suggested [29]). Model systems therefore provide an opportunity to determine what causes bilayer heterogeneity at length and timescales that are perhaps biologically relevant.

The evidence for heterogeneity in cellular membranes comes from numerous independent methods [53]. The most widely used method, detergent fractionation, isolates membrane regions which correlate in composition and structure with the L_o phase from model systems [54-57]. However, interpretation of this method is hindered by

inconsistencies and concerns about the unintended effects of the detergents [58-60]. More direct evidence of structural heterogeneity comes from observation of clustering of established raft markers, such as glycophosphatidylinositol anchored proteins (GPI-AP), and the use of FRET, fluorescence correlation spectroscopy (FCS), and other methods [61-65]. These experiments collectively suggest the existence of domains on the length-scale of ~tens of nm and the subnanosecond timescale. Direct observation of lipid heterogeneity is more difficult, though recently FCS and electron spin resonance have suggested domains similar to that observed through GPI-AP [66, 67].

There appear to be several mechanisms by which proteins localize to rafts. The most clearly understood case is for GPI-AP, which have been shown to associate with the L_o phase in model bilayers [68-71] and the L_o-like regions of cellular membranes through detergent fractionation [72, 73], and have been directly observed forming clusters [61-64]. Other post-translational modifications, particularly palmitoylation, also appear to be important [74-79]. Numerous mutagenesis studies suggest that specific amino acids can determine localization, though no consistent explanation has emerged [76, 80-87]. Additional factors, such as hydrophobic thickness [88-91] and oligomerization [78] are hypothesized to be important. A complete description of the factors which determine protein localization remains unresolved, suggesting the need for model studies of membrane heterogeneity.

1.3 Bilayer Asymmetry

An unresolved aspect of lipid raft structure is the relationship between the two leaflets of the bilayer. It is well established that lipids which neighbor each other laterally have an (intraleaflet) effect on structure; for example, cholesterol promoting ordered states in neighboring lipids [36]. However, the extent to which the two leaflets of the bilayer are coupled together remains an unresolved issue. This question is particularly intriguing with regards to raft function. For example, if rafts were to align in opposing leaflets, this would allow co-localization of integral and peripheral membrane proteins on both sides of the membrane, rather than on just one. Several experiments in model systems have observed L_o domains to overlap, or register, in opposing leaflets [92-95], though exceptions have also been observed [96-98].

The potential importance of interleaflet interactions is emphasized by the differences in lipid composition between the two leaflets of biological membranes [1, 99-104]. In particular, it appears that the composition of the outer leaflet would favor phase separation, while the composition of the inner leaflet would be uniformly L_d [51, 105, 106]. Experiments in model bilayers which mimic this behavior have generally observed two possible results, depending upon the precise lipid composition and experimental setup. In some cases, an L_o domain in one leaflet can induce the opposite leaflet to form an L_o domain, even though in isolation that leaflet would be uniformly L_d [95, 105, 107-109]. However, in other cases L_o phase regions have no apparent effect on an opposing L_d leaflet, resulting in phase asymmetry. In these cases it is hypothesized that there may be interleaflet structural effects, but this has been difficult to resolve experimentally [108, 110, 111]. Therefore, model systems may be useful for understanding the structure of lipid rafts, by identifying the circumstances which favor domain registration and describing the structural effects of phase asymmetry. These questions will be the focus of Chapter 4.

1.4 Membrane Curvature

An important concept in membrane biophysics is the role of membrane curvature. As Figure 1-3 illustrates, lipids may have either positive (curving outwards) or negative spontaneous curvature (curving inwards) [112]. Biologically occurring lipids have a wide range of spontaneous curvature values, including values so positive and negative that the lipids no longer favor bilayers (e.g. short-chained PC lipids form micelles and PE lipids form the inverted H_{II} phase [113]). These non-lamellar lipids are particularly important during bilayer fusion, during which there are intermediate states which have a large negative curvature. Lipids with a near zero spontaneous curvature resist adopting these negatively curved states (which would confer a curvature stress), while lipids with a negative curvature will localize to the regions of negative curvature, promoting the rate of bilayer fusion [113].

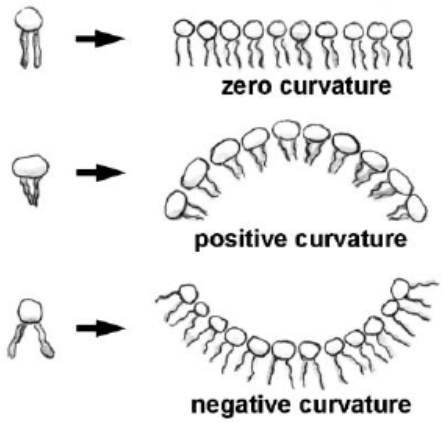

Figure 1-3 Spontaneous Curvature – Lipids have an innate curvature due to their chemical structure (taken from [112]).

The curvature of a membrane is thought to be an important factor when considering the behavior of membrane proteins. Membrane curvature has been suggested to be a mechanism which determines the localization of membrane proteins to specific intra-cellular membranes [114-118]. Furthermore, experiments in model systems have demonstrated that some of these proteins are not just passively localized to membranes with specific curvatures, but they are in fact actively shaping the curvature of the membrane [116, 118-120]; however, the mechanism by which this occurs remains a subject of interest [121]. Some proteins are thought to assemble into a rigid scaffold which has an intrinsic curvature which the membrane, being more flexible, is forced to match. Other proteins are thought to induce curvature by inserting partially into one leaflet, either inducing a curved deformation or altering the local area of one leaflet relative to the other [117, 121].

In this thesis, the relationship between membrane curvature and the behavior of the protein α-Synuclein is the focus of Chapter 5. Though the function of α-Synuclein is unknown, it has been suggested that it has a role in synaptic vesicle regulation [122-126]. Since synaptic vesicles are small, they have a positive curvature which is thought to be larger than the intrinsic curvature of the composite lipids. Therefore, the lipids are thought to be under a curvature stress which is relieved by fusion with the relatively flat presynaptic terminal membrane (which allows the release of the vesicle contents into the

synapse). It has been suggested that α-Synuclein's role is to alter the curvature of the membrane, relieving that stress, and thus regulating vesicle fusion [127-129].

1.5 Membrane-mimetics

A focus of this thesis is the complexity of membrane structure and specifically, those features that affect membrane protein behavior. However, the subtlety of membrane structure poses a difficulty when considering experimental characterization of membrane proteins. Typically, experiments utilize membrane-mimetics, and in particular detergent micelles. However, the environment formed by detergent micelles is obviously different than that of a lipid bilayer, for example having a larger degree of curvature and a larger variability in hydrophobic thickness [130]. The structure that membrane proteins adopt in a lipid bilayer can be substantially different from that formed in a micelle, for example α-Synuclein appears to undergo a conformational change depending on the environment (see Chapter 5) [129, 131]. Understanding the structure of membranes and membrane-mimetics is the motivation behind Chapter 6, where the structure of a membrane protein–stabilizing polymer is characterized. Developing membrane-mimetics which reproduce the membrane environment is essential for structural study of membrane proteins.

1.6 Molecular Dynamics Simulations

Molecular Dynamics (MD) simulations are a computational method for modeling the structure and dynamics of molecular systems. MD simulations utilize Newtonian physics to relate the forces (F) on each atom in the system (i) with the changes in position (r) over time (t). These forces are calculated from the gradient of a potential energy function (V).

$$-\nabla_i V = F_i = m_i a_i = m_i \frac{d^2 r_i}{dt^2} \qquad \textbf{Eq 1-1}$$

A typical potential energy function is presented as Eq 1-2. The first set of terms in the potential energy function are the bonded terms, which describe the potential energy due to the geometry of atoms covalently bound together, including the length of bonds, the angles formed by three consecutive atoms, and dihedrals angles of four consecutive atoms. Bond lengths, angles, and proper dihedrals (e.g. gauche vs. trans dihedrals) are

described by a harmonic potential. Improper dihedrals, which are used to enforce planarity, are also included for certain molecules.

$$V = \sum_{Bonds} \frac{1}{2} K_{Bond} (R - R_{Bond})^2 + \sum_{Angles} \frac{1}{2} K_{Angle} (\theta - \theta_{Angle})^2 +$$
$$\sum_{ProperDihe\ drals} K_{Dihedral} \left[1 + \cos(\Phi - \Phi_0)\right] + \sum_{ImproperDih\ edrals} \frac{1}{2} K_{IP} (w - w_{IP})^2 +$$
$$\sum_{Non-Bonded} \left\{ 4\varepsilon_{ij} \left[\left(\frac{\sigma_{ij}}{r_{ij}} \right)^{12} - \left(\frac{\sigma_{ij}}{r_{ij}} \right)^{6} \right] + \frac{q_i q_j}{D r_{ij}} \right\}$$

Eq 1-2

The last summation models the interactions between atoms which are not bonded together. The first non-bonded term is the Lennard Jones potential, which describes the non-covalent interaction between atoms. In this formulation, ϵ is depth of the energy minima, σ is the particle diameter (nearest distance at which the potential energy is zero), and r is the distance between the two particles. The electrostatic interactions are defined using a Coulomb potential, where q is the charge of each atom, and D is the effective dielectric. In the case where the solvent is explicitly represented, D is omitted. Note that each atom is represented as a single point, with a set mass and charge, explicitly neglecting higher resolution features such as the electronic structure and hence changes in covalent bonding.

In practice, there are numerous modifications made to this scheme in order to increase the rate of calculation. The primary computational cost is due to calculating the non-bonded interactions between every pair of atoms (N), or N^2 number of interactions. The calculation of the non-bonded interactions can be reduced by using an implicit solvent, where the effective dielectric constant is set (for water typically to 80), greatly reducing the number of non-bonded pairs. Alternatively, the calculation of the Lennard-Jones interaction can be limited to small distances, since the magnitude of the interaction is near zero at larger distances (a typical cutoff would be ~1 nm). Similarly, long-range electrostatics are more efficiently calculated through the Ewald summation, which

performs the calculation in Fourier-space. Finally, periodic boundary conditions minimize the role of non-physical boundary artifacts in small systems.

1.7 All-atom and Coarse-grained MD

Different representations are possible within the MD scheme. In section 1.6, the components of the simulations were referred to as atoms for conceptual simplicity. This is referred to as the All-Atom (AA) representation. Alternatively, in the coarse-grained (CG) representation, multiple atoms (in this thesis ~10 [132, 133]) are grouped together into multi-atomic "beads". These models seek to maintain the essential features of the molecules while simplifying the calculation to allow for simulation of larger systems and longer timescales.

There are broadly two methods for defining a CG force-field. In the first, the CG representation comes directly from AA simulation, such that probability density of states observed for the CG simulation matches an AA simulation [134, 135].

$$H(x^n, p^n) = \sum_{i=1}^{n}\left(\frac{p_i^2}{2m_i}\right) + V(x^n)$$

$$\Pr(x_{AA}, p_{AA}) \propto \exp\left(-H_{AA}(x_{AA}, p_{AA})/k_B T\right) \qquad \textbf{Eq 1-3}$$

$$\Pr(x_{CG}, p_{CG}) \propto \exp\left(-H_{CG}(x_{CG}, p_{CG})/k_B T\right)$$

$$\Pr(x_{AA}, p_{AA}) \approx \Pr(x_{CG}, p_{CG})$$

Eq 1-3 states this idea in the language of statistical mechanics. The first line presents the Hamiltonian, or the sum of the kinetic and potential energies for a system of *n* particles defined by their momenta (*p*) and coordinates (*x*). The first line applies to both the AA and CG representations, though the form of the potential energy function may differ. The probability distribution of states (i.e. atomic coordinates and momenta) for an AA or CG system is related to the relative energies of the possible states. The normalization factor which would allow us to state lines 2 and 3 as equalities rather than proportionalities is the partition function, which is inaccessible from an MD simulation. If the probability distribution of a CG simulation matches that of an AA force-field (i.e. if line 4 of Eq 1-3 were an exact equality) the two force-fields would be consistent. Therefore, CG force-fields can be designed such that the approximation in line 4 is as close to an equality as

possible, specifically by altering the form and parameters of the CG potential energy function [134, 135]. The formulation of this potential energy function is complicated by the need to compensate for entropic effects from the degrees of freedom that have been removed in the transfer to a CG representation [134, 136]. While this strategy allows the most rigorous connection between representations, it is specific to a thermodynamic state and may not be transferable to other states.

Alternatively, CG force-fields can be developed which utilize relatively simple potential energy functions, similar to those described for AA force-fields in section 1.6. These CG force-fields are typically parametrized based on a combination of experiments and AA simulations. Numerous force-fields of this nature have been used to investigate many molecular systems, including membranes and membrane proteins [132, 133, 137-139]. For example, in the Martini CG force-field (used in this thesis), the potential energy function is the same as in Eq 1-2, with the Lennard Jones parameters optimized to match experimental oil/water partitioning and the bonded interactions based on AA simulation [132, 133]. Force-fields of this nature are intended to be more generally applicable, but their consistency with AA simulation is not necessarily optimized (as in Eq 1-3).

The increase in accessible timescale afforded by the use of the CG resolution is necessary to model the phenomena of interest in this thesis. AA simulations on the nanosecond timescale are sufficient for equilibrating structural features on the angstrom length-scale, such as bilayer thickness or rotation of protein sidechains leading to the formation of hydrogen bonds. However, CG simulations allow access to nanometer scale phenomenon, such as lateral phase separation [140, 141], flip-flop of cholesterol between leaflets [41, 142], and polymer complex self-assembly. This thesis uses MD simulations of both representations in order to model the structure and dynamics of membranes and membrane proteins.

I Computational Modeling of Lipid Bilayers

Preface

The contents of Section I trace a path from very simple to relatively complex models of lipid bilayers. Chapter 2 describes the simulation of small, single component lipid bilayers, with a focus on characterizing the bilayer thickness. Chapter 3 contains simulations of ternary mixtures, in order to determine what features of membrane steroids promote or inhibit lateral heterogeneity. Chapter 4 further investigates laterally heterogeneous ternary mixtures which also include differences in content and structure within the two leaflets of the bilayer, describing interleaflet organization and structural perturbations. This progressive increase in complexity allows us to build towards the intricacy of biological membranes and begin to unravel the many factors which determine their structure and function.

The different levels of complexity demand differences in methods. For our simplest systems, as in Chapter 2 we can use the more precise all-atom force-field and compare our results with experimental small angle X-ray scattering (SAXS). This process is similar to that used in a recent project of ours, completed prior to work in this thesis [36]. Figure 0-1 summarizes this strategy, showing the experimental result (A), the simulation result (B), and the agreement between the two (C). This experiment is sensitive to the thickness of the bilayer, and by adjusting the thickness of our simulated system we can determine an experimentally verified bilayer thickness. The original aspect of Chapter 4 is the inclusion of the lower resolution coarse-grained force-field, allowing longer time- and length-scale equilibration, prior to experimental comparison. This multi-scale strategy is necessary for modeling larger-scale features, and is applied to a non-bilayer system in Chapter 6. However, our efforts to apply it to more complicated bilayer systems have not yet been successful.

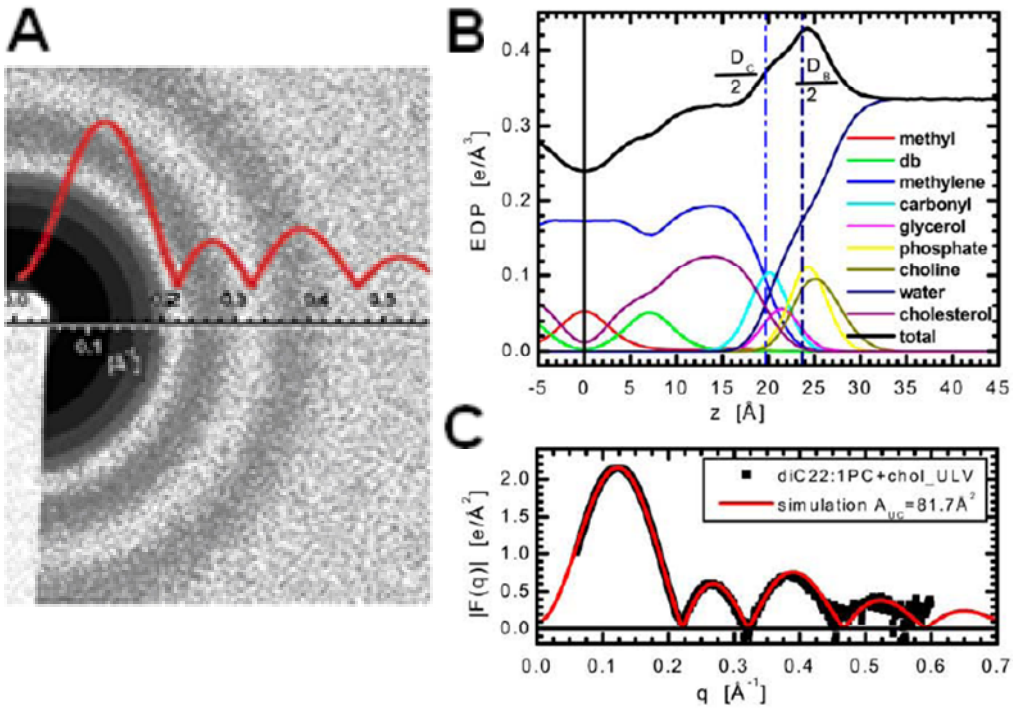

Figure 0-1 – MD simulation and SAXS A) Experimental SAXS and F(q) obtained from radial integration. B) Electron density profile obtained from simulation. Fourier transform of the electron density profile yields the simulated F(q), (C) allowing comparison between experiment and simulation (Figure taken from [36]).

In Chapters 3 and 4 we investigate more complex features of lipid bilayers, necessitating the use of the coarse-grained representation. Specifically, in Chapters 3 and 4, we consider bilayers containing lateral heterogeneity, i.e. bilayers containing a thicker L_o region and a thinner L_d region. However, SAXS is sensitive to the average thickness, and we find that simulation of heterogeneous and homogeneous mixtures leads to the same calculated SAXS profile (Figure 0-2), and is therefore inadequate for describing this feature. While it is possible that we might use SAXS to detect subtle changes in thickness, such as we predict to occur in asymmetric bilayers (see Chapter 4), our preliminary measurements suggest that this is a more difficult experiment.

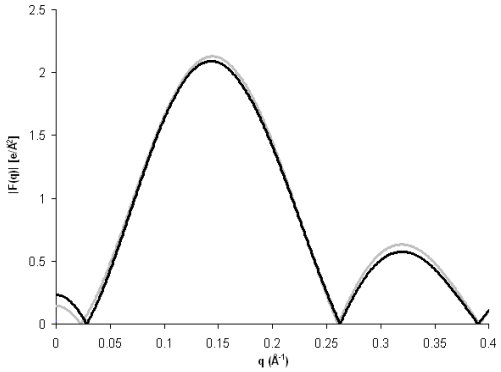

Figure 0-2 – SAXS of phase separated bilayers. Comparison of SAXS calculated from simulation of a laterally homogeneous bilayer (gray) and a laterally heterogeneous bilayer (black).

What we have been able to obtain in this thesis is a quantitative experimental verification of bilayer thickness, as well as insight into the behavior of more complicated systems. Where quantitative experimental verification is not yet obtainable, such as for the system described in profile Figure 0-2, we can often discuss a qualitative relationship between our simulations and previous experimental results. For example, in Chapter 3, we relate previous experimental observations of domain inhibition and promotion to our simulations which predict these same behaviors for molecules which resemble those used in the experiments. Obtaining quantitative verification of these features is the goal of future research.

Each chapter of this section is based on a published manuscript. Supplemental information and figures are available through the respective journals.

- Chapter 2: Reproduced with permission from Perlmutter, J. D.; Sachs, J. N. *Biochim Biophys Acta* **2009,** *1788*, 2284-90. Copyright 2009 Elsevier B.V. [143].

- Chapter 3: Reprduced with permission from Perlmutter, J. D.; Sachs, J. N. *J Am Chem Soc* **2009,** *131*, 16362-3. Copyright 2009 American Chemical Society [144].

- Chapter 4: Reproduced with permission from Perlmutter, J. D.; Sachs, J. N. *J Am Chem Soc* **2011,** *133*, 6563-6577. Copyright 2011 American Chemical Society [145].

- Figure 1 in this preface reproduced with permission from Kucerka, N.; Perlmutter, J. D.; Pan, J.; Tristram-Nagle, S.; Katsaras, J.; Sachs, J. N. *Biophys J* **2008,** *95*, 2792-805. Copyright the Biophysical Society Published by Elsevier Inc [36].

2 Experimental Verification of Lipid Bilayer Structure using Multi-scale Modeling

2.1 Introduction

Elucidating the structures of fluid-phase lipid bilayers has had a growing impact on our understanding of membrane biology and biophysics [6, 142, 146, 147]. In particular, recent studies have been geared toward understanding the connection between a membrane's molecular composition and its structure. For example, the presence of cholesterol can increase a membrane's thickness, which is frequently measured by the lipid headgroup-to-headgroup distance (D_{HH}) in the bilayer's electron density profile [148-150]. In the case of single component lipid bilayers, the thickness is inversely related to a key structural parameter, namely the cross-sectional area-per-lipid molecule (A_L) [146].

X-ray scattering of lipid assemblies such as MLVs, ULVs and oriented stacks is a widely used experimental technique that can yieL_d the EDP via Fourier transformation of the scattering intensity (or, more precisely, the form-factor, F(q)) [146]. In particular, small-angle x-ray scattering (SAXS) gives low-resolution information regarding overall molecular size; low-angle x-ray scattering (LAXS) has been used to determine thickness and the overall shape of the EDP; and wide-angle scattering (WAXS) has been used to study features in the plane of the bilayer, for example micro-domains, or rafts [146, 151].

Recently, we and others have used computational all-atom molecular dynamics simulations (AAMD) in conjunction with LAXS as an alternative approach for determining lipid bilayer structure, in particular for determining thickness and A_L in single-phase bilayers composed of either a single lipid or binary mixtures of lipid and cholesterol or lipid and protein [149, 152-154]. In this approach, the Fourier transform of the EDP (which is calculated directly from simulation) yieL_ds the predicted $F^{sim}(q)$, which is then compared directly to the experimentally derived $F^{expt}(q)$. This approach treats A_L as an adjustable parameter, wherein multiple simulations of membranes are run at constant area (in the NP_NAT ensemble) until a match to experiment is determined. Two important aspects of single-phase bilayers make this multiple-simulation approach tractable. First, simulations of small bilayer patches are sufficient to get the EDP, making the simulations reasonably inexpensive and fast to run. Second, compression or expansion of a pre-

equilibrated bilayer can proceed quickly if brief equilibration (≈10 ps) is allowed at multiple intervening areas. Full equilibration at a target area can be achieved in no more than five to ten nanoseconds.

The computational problem becomes significantly more complicated when trying to determine structures of bilayers containing ternary mixtures that are known to undergo macroscopic, lateral phase separation. Currently, AAMD simulations are not able to access the time- and length-scales necessary to model lateral separation. To overcome this problem, great progress has been made in the study of complex membranes through coarse grained molecular dynamics (CGMD) simulations [155]. CGMD simulations, in which groups of atoms are treated as a single bead, can access phenomena on time- (> 10 μs) and length-scales (> 1000 lipids) still inaccessible to AAMD simulations [134]. In particular, using the Martini CGMD force fieL_d [156], large-scale phenomena including vesicular fusion [157], monolayer collapse [158], phase transition [159], and lateral domain formation [25, 158] have been successfully simulated. Therefore, CGMD is a promising tool for determining the structure of complex membranes, where the lateral organization of the bilayer's components is not known *a priori*.

Despite these recent achievements, a detailed comparison between lipid bilayer structures obtained from CGMD and experiment, namely LAXS, has not yet been performed, and is the focus of this current study. Comparisons have been made between the component density profiles of AAMD and CGMD simulated bilayers [25], and it has been noted that these densities are not perfectly matched. In particular, Martini CGMD lipid bilayers are thicker, and there is ambiguity when comparing water penetration into the bilayer's headgroup region [25, 160]. Though such discrepencies are not present in all CGMD formulations [161], they may be an inevitable result of coarse graining, and do not undermine the general utility of the approach in generating equilibrated structures of complex membrane mixtures. These discrepancies do, on the other hand, necessitate further effort if the CGMD simulations are to be useful in high-resolution bilayer structure determination.

Testing the equilibrated structures obtained through long time- and length-scale CGMD simulations is best done through a process of reverse coarse-graining (rCG),

whereby an all-atom model is superimposed onto the CG structure, minimized and equilibrated through a brief AAMD simulation. How brief this equilibration period must be depends upon the system, and also likely depends upon the scale of structural resolution being tested. Recently, Shih et al. utilized a rCG scheme to test the structure of a lipoprotein complex against SAXS data, and showed reasonable agreement in the small q-regime, reflecting agreement in the overall size and shape of their simulated particles [162]. In this case, the authors determined that only 0.5 ns of AAMD simulation was enough to equilibrate the SAXS data, while in a separate rCG study water permeation through oligomeric peptide pores required 50 ns [160].

In the case of lipid bilayer structure at the resolution of LAXS (F(q) and the EDP), the necessary length of equilibration of a rCG structure has not been established, and is a focus of this study. Equilibration of the EDP depends upon dynamic sampling of multiple structural features, for example water penetration into the headgroup region and bilayer thickness. Our algorithm, which tests for equilibration of each of these features, starts by selecting a variety of snapshots from the CGMD trajectories that are then reverse coarse grained. Unlike our AAMD simulations, in which the lateral dimensions of the simulation cell are fixed in time, each CGMD simulation operates under the NPT ensemble, and thus samples a range of lateral areas. By starting from snapshots at varying areas, our rCG AAMD simulations can be used to test for equilibration times and to test the resulting structures directly against the LAXS experimental data, hence determining A_L and providing additional structural information.

We present results for both 1-Palmitoyl-2-Oleoyl-*sn*-Glycero-3-Phosphocholine (16:0-18:1PC or POPC), which has been studied previously through CGMD and AAMD, and 1,2-Dierucoyl-*sn*-Glycero-3-Phosphocholine (di-22:1PC), which we have recently investigated using all-atom MD and LAXS [149], but has not been studied with CGMD. We demonstrate that using our multi-scale rCG algorithm, which allows for equilibration on both large and small length scales, we are able to accurately match LAXS experimental data for both lipid types. Our method lays the foundation for future efforts to obtain experimentally verified, detailed structural information from CGMD simulations of more complex multi-component, multi-phase lipid bilayer systems.

2.2 Methods

2.2.1 CGMD Simulations

Parameters for the Martini CGMD force fieL_d and coordinates for other lipid bilayers adapted for the starting configurations were obtained from http://md.chem.rug.nl/~marrink/coarsegrain.html. Parameters for di-22:1PC were created following the conventions used for other lipids. Both the 16:0-18:1PC and di-22:1PC systems contained 128 lipids and 1500 coarse grain waters.

CGMD simulations were run using Gromacs version 3.3.3 [163]. Simulations were performed using periodic boundary conditions and a constant number of particles (N), pressure (P), and temperature (T). Bilayers were in the liquid phase, run at a temperature of 303 K for di-22:1PC and 311 K for 16:0-18:1PC, above the T_M for these lipids [164]. We applied the Berendsen temperature and pressure coupling scheme with relaxation times of 0.1 ps and 0.2 ps respectively, using a reference pressure of 1 bar. The pressure scheme was applied in a semi-isotropic manner resulting in a tensionless bilayer. We utilize the convention of describing the effective time sampled as a four-foL_d increase over the simulation time, due to a "smoothing" of the energy profile in coarse grain simulation [156]. Simulations were run with a time step of 30 fs for a duration of 120 ns effective time, and we considered timepoints after 20 ns for our analysis of CG bilayer structural properties.

2.2.2 AAMD Simulations

Bilayer structures generated through CGMD simulation were converted to an all atom representation in the CHARMM force fieL_d using the CHARMM software package (version 32) [165]. The coordinates of the coarse grain beads were used as coordinates for selected atoms in the lipid. These mapped atoms were then restrained using a harmonic potential while the rest of the system was minimized, creating a structure that maintains the geometric features of the coarse grain model, but allowing energy minimization of the new atomistic features, similar to the strategy used in a previous study [162]. CG waters were not included in this part of the process. The all-atom lipids were then placed in a pre-equilibrated water box and overlapping water molecules within 2.6 Å of any non-hydrogen atom were then removed. AAMD simulations were performed in NAMD (version 2.6) [166], using periodic boundary conditions, and a constant number of particles

(N), lateral area (A), normal pressure (P_N), and temperature (T). These NAP_NT ensembles were run at a temperature of 303 K for di-22:1PC and 311 K for 16:0-18:1PC. A cutoff of 10 Å was used for van der Waals interactions and particle mesh $EwaL_d$ summation was used for long range electrostatic interactions. The time step was 2 fs and all bonds involving hydrogens were fixed using the SHAKE algorithm. Both CGMD and atomistic structures were visualized using VMD [167].

2.2.3 Low Angle X-ray Scattering Experiments

The di-22:1PC scattering has been presented previously, and additional details of the methods used can be found therein [149]. For both lipid types, synthetic lipids in chloroform were purchased from Avanti Polar Lipids (Alabaster, AL) and used without further purification. All other chemicals were reagent grade. Before preparation of unilamellar vesicles (ULVs), chloroform was evaporated under a stream of nitrogen gas, followed by vacuum pumping. The lipid film was then dispersed in 18 MΩ-cm water (Millipore, Billerica, MA) at a total lipid concentration of 20 mg/mL. The lipid dispersions were extruded using two polycarbonate filters with pore diameters of 500 Å to produce ULVs. X-ray data on ULVs were taken at the Cornell High Energy Synchrotron Source (CHESS).

Corresponding form factors were calculated from the MD simulations through the equation:

$$|F(q)|^2 = \left(\int_{-D/2}^{D/2} [\rho^*(z) - \rho^*_W]\cos(qz)dz\right)^2 + \left(\int_{-D/2}^{D/2} [\rho^*(z) - \rho^*_W]\sin(qz)dz\right)^2 \qquad \textbf{Eq 2-1}$$

where ρ^* is the simulated electron density, ρ^*_W is the electron density of water, and D is the average dimensions of the simulation box. The contribution of the sine component is zero in the case of symmetric bilayers, such as we describe in this study. The experimental form factors are scaled to the calculated form factors through a least squares fitting algorithm. The quality of the fit between the experimental and calculated LAXS profiles is quantified through the root mean square deviation using the equation:

$$RMSD = \sqrt{\sum (|F^{sim}(q_i)| - k|F^{expt}(q_i)|)^2} \qquad \textbf{Eq 2-2}$$

where $F^{sim}(q)$ is the form factor from simulation, $F^{expt}(q)$ is the form factor from experiment, and k is the scaling factor determined through least squares fitting.

2.3 Results

The first step in our multi-scale strategy for bilayer structure determination is to run a CGMD simulation. For both 16:0-18:1PC and di-22:1PC, we have run 120 effective ns of CGMD dynamics, which is more than sufficient time for relaxation of A_L, as shown in Figure 2-1. Large fluctuations in A_L are typical of both CGMD and AAMD bilayer simulations run in the NPT ensemble. The trajectory averaged values of A_L are similar to values observed previously for both lipids. In the case of di-22:1PC, the CGMD mean A_L (67.5 $Å^2$) is very similar to our recent report using AAMD and LAXS (68.3 $Å^2$) [36]. For 16:0-18:1PC, there is a slightly larger discrepancy between the CGMD mean area (65.5 $Å^2$) and that determined by a recent experimental study (68.3 $Å^2$) [168], though experimental refinement is still evolving [149]. In the case of another lipid, di14:1PC, the CGMD values are significantly different (a discrepancy of > 5 $Å^2$/lipid, data not shown).

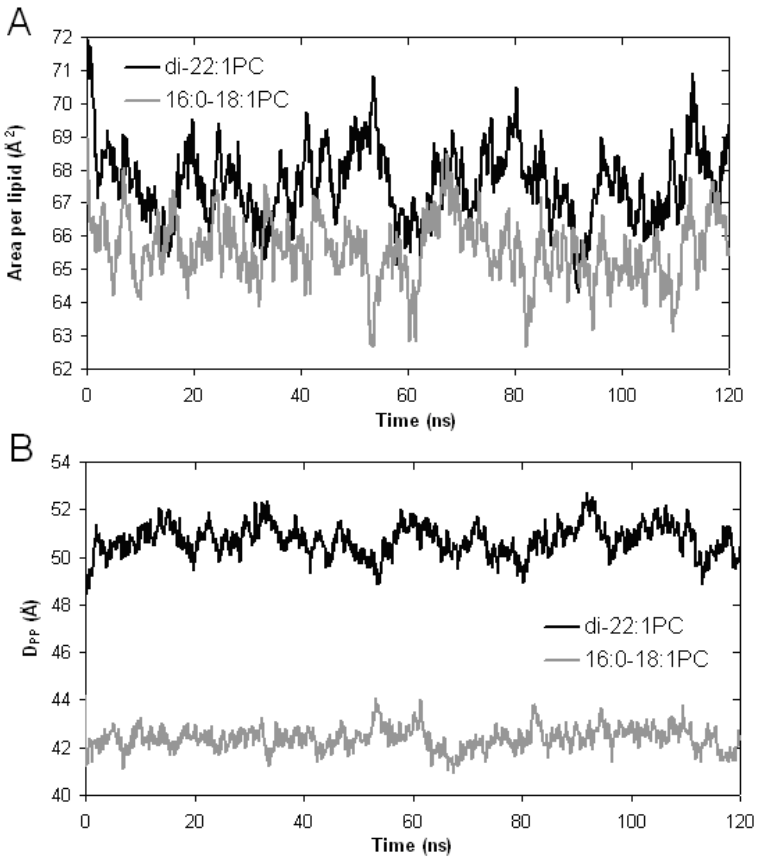

Figure 2-1 CGMD Thickness and Area – A) Variations in the lateral area per lipid for di-22:1PC and 16:0-18:1PC CGMD simulations. B) Variations in the bilayer thickness in CGMD simulations, as measured through the mean distance between phosphate groups in opposing leaflets.

Figure 2-1B shows the time-series for bilayer thicknesses, in this case measured as the distance between the average phosphate bead position in the upper and lower leaflets (D_{PP}), which equilibrates to mean values of 50.8 Å (di-22:1PC) and 42.4 Å (16:0-18:1PC). Direct comparison of the thickness between CGMD and either AAMD or experiment is complicated by the inherent coarseness of the model. For example, a CG chain consisting of 4 beads, is considered an approximate model for a chain of 15-18 carbons. Therefore, it is unreasonable to expect a precise match between the thickness of the CGMD model and an AAMD palmitoyl chain which consists of precisely 16 carbons. Indeed, we observe that the CGMD D_{PP} values are significantly larger than reported in a recent experimental study, which found D_{PP} of 45.0 Å (di-22:1PC) and 37.6 Å (16:0-18:1PC) [168], as indicated in Table 2-1. Therefore, in order to obtain experimentally

verifiable structures, it is necessary to convert from a CGMD representation to an AAMD representation.

	di-22:1PC	**16:0-18:1PC**
A_L (Experiment) [Å^2]	69.3	68.3
A_L (CGMD) [Å^2]	67.5	65.5
A_L (AAMD) [Å^2]	67.6	68.5
D_{PP} (Experiment) [Å]	45.0	37.6
D_{PP} (CGMD) [Å]	50.8	42.4
D_{PP} (AAMD) [Å]	45.1	37.2

Table 2-1 Structural Parameters - Comparison of bilayer structural parameters area per lipid (A_L) and distance between phosphate groups in opposing leaflets (D_{PP}), obtained through previous X-ray scattering experiments [168], our CGMD simulations, and our AAMD simulations which best match the $F^{expt}(q)$. Note that the experiments were performed at room temperature, and the simulations performed at 303 K (di-22:1PC) and 311 K (16:0-18:1PC). Temperature differences of this magnitude can cause slight changes in bilayer structure [169].

Figure 2-2 illustrates our reverse coarse graining process, which is done to a single frame extracted from the CGMD trajectory. That frame, once reverse coarse-grained, acts as the starting configuration for an AAMD simulation. Figure 2-2A shows a typical snapshot taken from the di-22:1PC CGMD simulation. Figure 2-2B illustrates the rCG process for a single lipid, overlaying the CG beads and the AA lipid structure. Figure 2-2C shows the snapshot of the entire bilayer produced by the rCG process, before waters have been added back. The rCG atomistic structure is invariably far from equilibrium, as details at atomic-scale resolution (e.g. bond lengths and angles, and torsion angles) are absent in the CG representation and there is no physical basis upon which to base a unique mapping strategy. At this stage of the rCG process, all that can be fairly stated is that the overall positions of the lipids are correct. That is, the lateral

organization is consistent with that generated by the CGMD simulation. In order to equilibrate this AA bilayer, energy minimization and AAMD must then be performed.

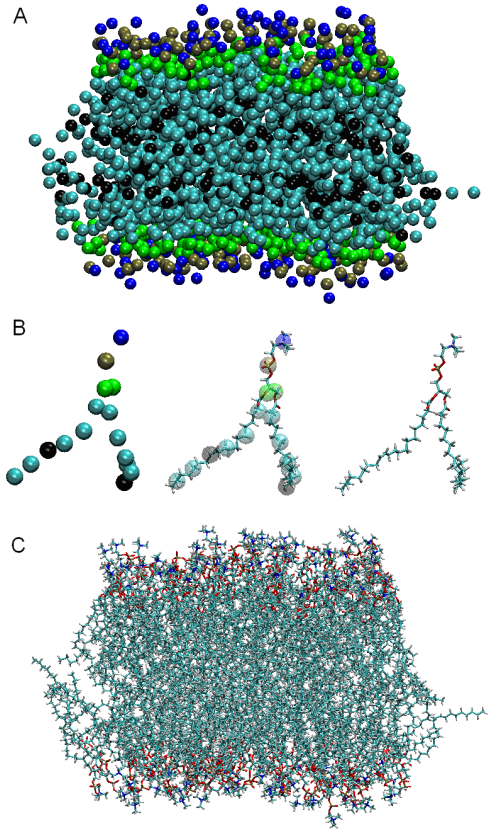

Figure 2-2 Reverse Coarse-Graining – A) CGMD di-22:1PC bilayer after 30 ns of dynamics. B) Overlay of minimized atomistic lipid ("licorice" representation) with CGMD lipid (transparent spheres) demonstrates that the reverse coarse grained structure reproduces the geometry of the CGMD structure. C. Atomistic bilayer obtained from reverse coarse graining. CGMD structure is represented as: Choline group=Blue, Phosphate group=Brown, Glycerol Backbone group=Green, Methylene and Methyl Chain group=Light Blue, Double Bond group=Black. Atomistic structure is represented as: Hydrogen=White, Carbon=Light Blue, Oxygen=Red, Phosphorous=Brown, Nitrogen=Blue. Water is omitted from both representations.

In this study, we have reverse coarse grained structures from three CGMD timepoints for each lipid-type. These structures were chosen to span the range of A_L values seen in Figure 2-1A, using the highest, lowest and median values. For di-22:1PC these corresponded to timepoints at t = 92ns (A_L = 64.3 Å^2), t = 89 ns (A_L = 67.6 Å^2) and t = 54 ns (A_L = 70.8 Å^2). For 16:0-18:1PC, these corresponded to t= 82 ns (A_L = 62.7

Å^2), t=23 ns (A_L = 65.6 Å^2) and t=67 ns (A_L = 68.5 Å^2). The resulting rCG structures were then energy minimized (via steepest descent minimization) and used as starting configurations for constant area, AAMD simulation.

Before calculating the EDP and comparing $F^{sim}(q)$ and $F^{expt}(q)$, it was necessary to determine the length of post-reverse coarse graining equilibration. An important structural feature of these AAMD bilayers that has a substantial affect on the EDP, and that must be monitored for full equilibration, is the water density distribution in the headgroup region. Though there is some ambiguity in assigning water positions that could be somewhat ameliorated by assuming a Gassusian distribution, we and others have observed that CG waters in this force fieL_d do not penetrate deeply enough (as measured by the centers of the four-water beads) into simulated PC bilayers, (data not shown, [160, 170]). Therefore, our rCG procedure starts with the lipids only: all CG waters are removed. After the lipids are reverse coarse grained, they are placed in a pre-equilibrated AA water box and overlapping waters are removed. Figure 2-3 shows a representative time-series of the number of water molecules (defined by the oxygen atom) within 5 Å of the different regions of the lipid. For both lipids, the results show that our water removal scheme initially left too great a density of water in the hydrophobic core of the bilayer. However, this problem was resolved by a short period of dynamics for each of the rCG simulations (on the order of several ns) as seen in the timeseries.

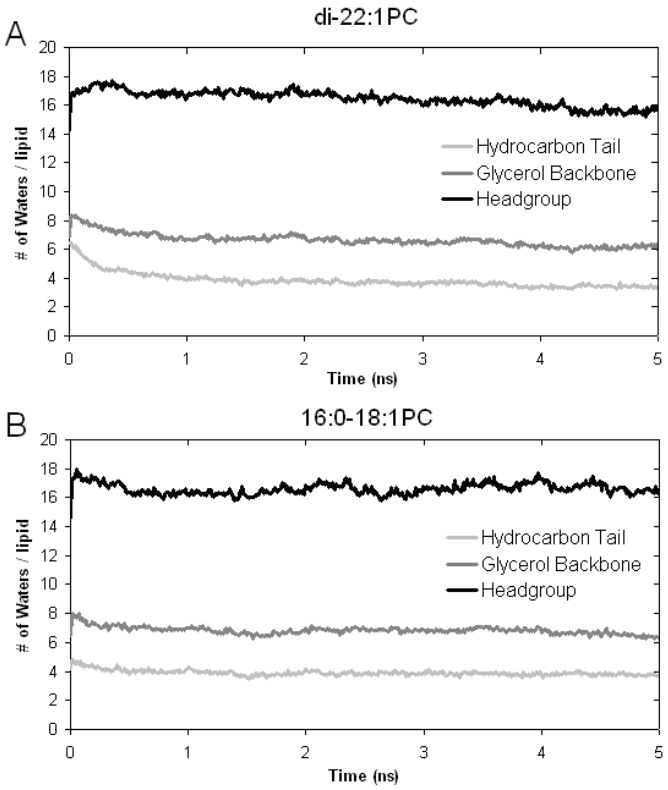

Figure 2-3 Water Equilibration - Number of water molecules within 5 Å of different lipid sections for both di-22:1PC (A) and 16:0-18:1PC (B). Slight changes in the water shell are observed at the beginning of the simulation for both bilayers.

Figure 2-4 plots the relevant time-series for evaluating the equilibration of the bilayer structure in comparing to LAXS experimental data. Figure 2-4A plots D_{PP} *vs.* time for each of the three simulated areas and, as expected, smaller areas correspond to larger thicknesses. In each AAMD bilayer simulation the thickness decreases from the CGMD thickness (compare to Figure 2-1B) and appears to relax to a stable value in the first 5 ns, though we do observe a continued decrease for the smallest area of 16:0-18:1PC. Figure 2-4B shows the progression of the first minima of the calculated LAXS form factor (equation 1), as a measure of form factor relaxation (other choices, for example the position of the other minima and maxima in F(q) show similar relaxation rates). In agreement with the decrease in D_{PP} (Figure 2-4A), the minima move outwards in q-space and are equilibrated by the end of the 5 ns simulation. Most importantly, Figure 2-4C shows the RMSD between $F^{sim}(q)$ and $F^{expt}(q)$, calculated based upon **Eq 2-2**. This describes the changes of the entire form factor over the course of the simulation

and again shows a similar rate of relaxation. Based on these data, we conclude that the thickness/LAXS profiles are fully equilibrated within 3 ns of atomistic simulation.

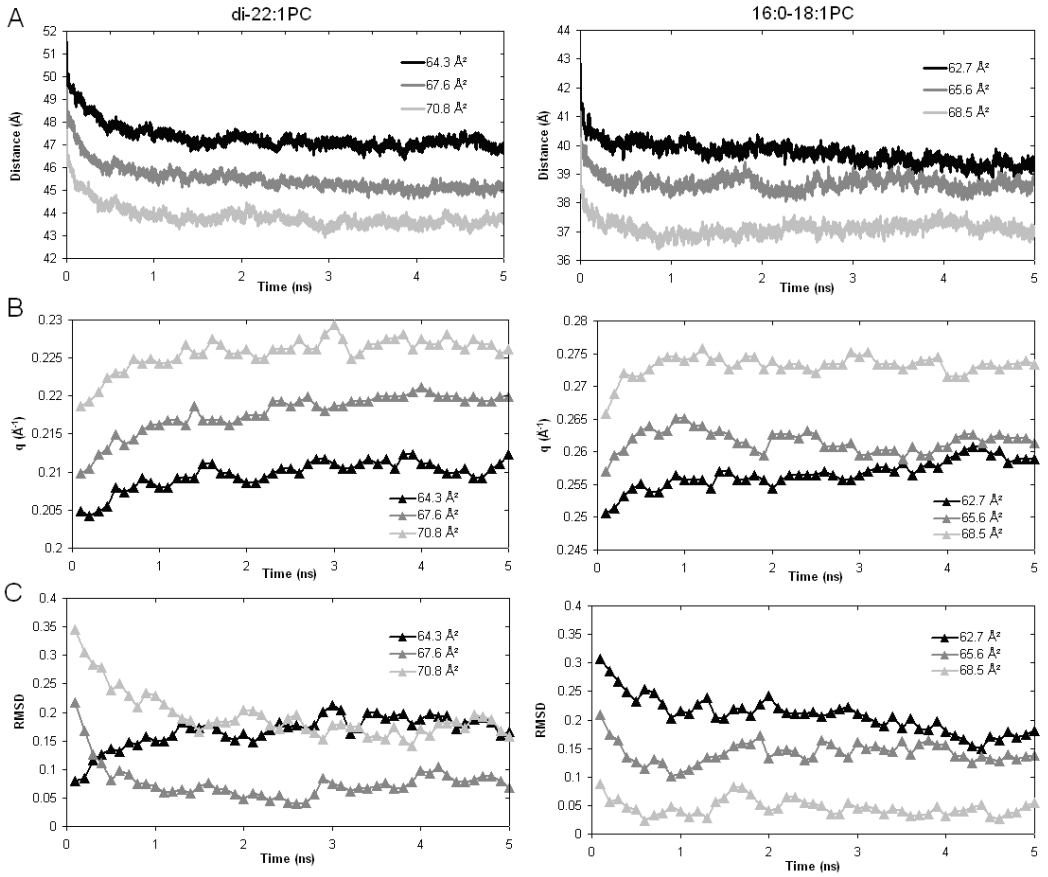

Figure 2-4 Post-rCG Equilibration – A) Decrease in thickness following reverse coarse graining over the course of a 5 ns atomistic simulation (di-22:1PC left and 16:0-18:1PC right). B) Increase in position in q space of the first minima of $F^{sim}(q)$ during 5 ns of atomistic simulation. C. RMSD of $F^{sim}(q)$ from $F^{expt}(q)$ during 5 ns of atomistic simulation.

Figure 2-5 shows the $F^{sim}(q)$ for each constant area AAMD simulation, calculated over the final 2 ns of the 5 ns simulations. As expected, increasing A_L (decreasing thickness) shifts $F^{sim}(q)$ to higher values in q-space. Similarly, the thicker di-22:1PC has features shifted lower in q-space than 16:0-18:1PC. We note that it is unlikely that 2 ns of simulation is able to completely sample the structure of a lipid bilayer, which is only describable as density functions. However, at length scale of interest here, our results suggest convergence of the $F^{sim}(q)$ and accurate matching to experiment. Figure 2-6 overlays $F^{sim}(q)$ and $F^{expt}(q)$ from the rCG AAMD simulations that have the lowest

RMSD from experiment, showing excellent agreement. For di-22:1PC, the best agreement results in A_L = 67.6 Å^2 (RMSD = 0.076); for 16:0-18:1PC, the best agreement gives A_L = 68.5 Å^2 (RMSD = 0.038). The areas determined match previous results [36, 168] as shown in Table 2-1.

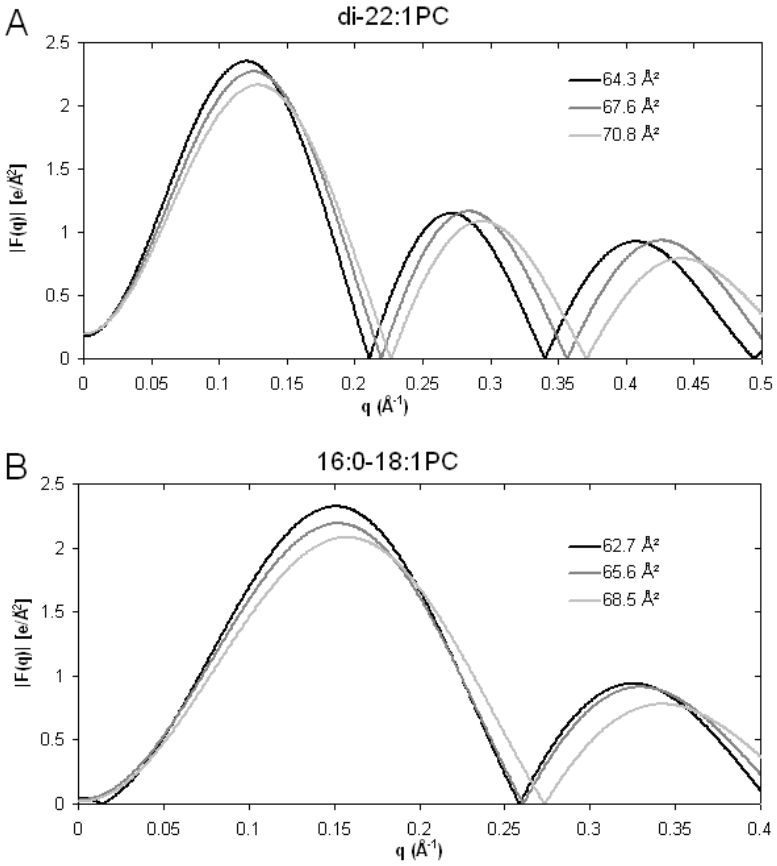

Figure 2-5 rCG Form Factors - Comparison between $F^{sim}(q)$ calculated from constant area, atomistic simulations for di-22:1PC (A) and 16:0-18:1PC (B) using timepoints from 3-5ns.

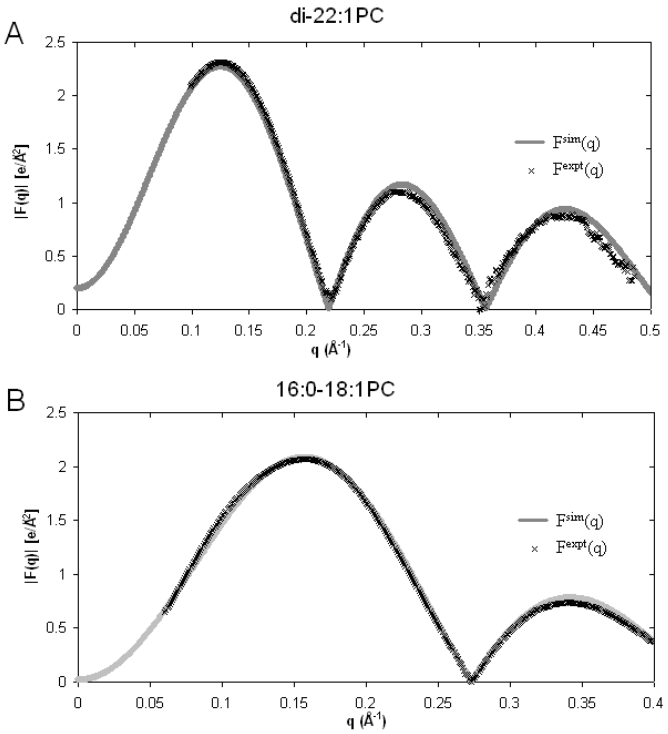

Figure 2-6 Experimental Verification - Overlay of $F^{expt}(q)$ and best fitting $F^{sim}(q)$ from atomistic simulations for di-22:1PC [A_L = 67.6 Å^2] (A) and 16:0-18:1PC [A_L = 68.5 Å^2] (B).

2.4 Discussion

We have developed a strategy for experimentally verifying bilayer structures generated from CGMD simulation. To achieve this, we have utilized a multi-scale approach that starts with CGMD simulation for equilibrating large-scale structural features. This is followed by a conversion to an atomistic representation and a period of AAMD simulation which equilibrates the atomistic structural features and, hence, the EDP and $F^{sim}(q)$. Our results indicate that equilibration of the LAXS profile occurs primarily within the first few nanoseconds of atomistic simulation, and that we are able to match our rCG bilayers to experiment with equal accuracy as we have done in our recent study which used only AAMD and LAXS [36].

An ultimate goal of molecular simulations of membranes is to be able to calculate their structures at multiple length-scales, thus matching SAXS, LAXS and WAXS scattering profiles. Experimentally, multi-scale structure determination has advanced considerably over the past several years, with significant strides in interpreting scattering

data in terms of the molecular organization in the dimensions normal to (LAXS) and lateral to (WAXS) the bilayer surface [146, 151]. Computationally, while structure determination is not trivial for single-phase systems, it too has progressed rapidly [171]. On the other hand, computational structure determination is particularly challenging for complex mixtures where the lateral distributions of component molecules is not known, making rational assignment of starting configurations impossible and necessitating long equilibration times. Therefore, the strategy most likely to be successful in the future is to make use of longer duration CGMD simulations for equilibrating macro-scale features (e.g. lateral distribution). However, in coarse graining, what is gained in computational efficiency is necessarily lost in chemical, and hence structural, detail. The relevance of that lost detail depends upon the scale of structure being probed. In calculating structures at a scale that is sensitive to atomic-scale organization (e.g. LAXS and WAXS) the CG structures must be converted to an atomistic representation in order to obtain accurate, highly resolved structures. Equilibrated AAMD structures can then be used to accurately match the scattering data and then to determine structural parameters with high resolution.

Because the different regimes of X-ray scattering (SAXS, LAXS and WAXS) that need to be matched by simulation access structural features at different length-scales, comparison of the experimental and simulated scattering profiles requires different degrees of resolution in the modeling of electron densities. While there has been moderate debate [36, 152, 172, 173], it is generally accepted that accurate calculation of SAXS and LAXS from AAMD simulation data can be achieved by assigning all of an atom's electrons to the center of the atomic bead. In the case of CGMD simulations, this strategy results in an even lower resolution structural description; diminishing both our ability to match to experimental data and to precisely determine structural features such as D_{PP}, D_{HH} (the headgroup thickness), D_C (the hydrocarbon thickness) and D_B (the Luzzati thickness) [146]. While there may be ways to more rationally assign the electron positions than this, the most efficient and robust approach is simply to reverse coarse grain as we have demonstrated in this paper. Unlike simulated LAXS, it is not sufficient to assign

electrons to atom centers when calculating the 2-dimensional WAXS profile [172] and developing the best algorithm for this calculation is a subject of our ongoing research.

There are several aspects of our approach that bear further discussion. The mean A_L of the CGMD simulation is correct for di-22:1PC (as well as several other lipids [170]), but not for 16:0-18:1PC. However, our strategy is still successful for 16:0-18:1PC because the CGMD simulation samples the correct area. As seen in Figure 2-1A, A_L for 16:0-18:1PC is at times as large as 68.5 $Å^2$, which is slightly larger than the experimental value of 68.3 $Å^2$. Therefore, the CGMD simulation samples the experimentally determined A_L for both lipid types presented in this paper. This is an essential condition for our algorithm, since accurate matching between $F^{sim}(q)$ and $F^{expt}(q)$ would not be obtainable at an incorrect area. As one example where this condition was not met, we have also tested our algorithm for a single-component di-14:1PC bilayer. The CGMD simulation did not sample the A_L we recently determined (A_L = 70.2 $Å^2$; data not shown) [36]. The mean A_L from the CGMD simulation was 64.8 $Å^2$, with a range of sampled areas of 62.6-67.6 $Å^2$. One possible solution to this problem would be to use this comparison to experiment in order to aid in reparameterization of the CGMD lipid force-fieL_d. A second, and more efficient, possibility would be to artificially manipulate the CGMD pressure coupling scheme in order to sample a wider range of lateral areas.

We have shown that, in the case of single-component bilayers, equilibration of the LAXS form factor occurs primarily within a few nanoseconds of the rCG procedure. Application of our algorithm to complex lipid mixtures, for example ternary mixtures that undergo lateral phase separation, will inevitably require additional scrutiny, in particular as regards the equilibration time of the rCG structures. For example, it is likely that in cholesterol containing systems, the equilibration time for thickness and both cholesterol and lipid rotational dynamics will be longer than 3 ns.

A final aspect of our approach that should be considered is our choice to change the ensemble between the CGMD (NPT) and atomistic (NP_NAT) simulations. There is a long standing debate over the optimal ensemble for modeling lipid bilayers, and how the ensemble choice affects the structural and dynamic properties of the system (for review see [171, 174]). Therefore, this change in ensemble could be a source of discrepancy between

the CGMD and AAMD structures. However, this seems unlikely to be a significant factor, as a previous study showed that structures generated using these two ensembles are similar when their areas are in agreement [175].

We conclude that our multi-scale approach is a potent method for obtaining experimentally verifiable structures from CGMD simulation. In the first step, the larger scale features of the system, such as bilayer formation, phase transition, or lateral separation can be equilibrated using CGMD. During this CGMD simulation the parameter of interest (e.g. A_L) is quantified as a basis for selecting structures for reverse coarse graining. The structures are then converted to an atomistic representation, and relaxed in order to allow for comparison to the relevant experimental data. Here, we have used LAXS, which is an appropriate experiment for the purposes of verifying bilayer lateral area and thickness, but not an effective way of verifying other structural features, such as lateral separation. However, using a similar multi-scale strategy, we will ultimately be able to obtain atomistic representations of phase separated bilayers, from which the WAXS profile will be calculated and compared to experiment. Implementing this strategy on more complex systems will be the goal of future investigations.

3 Inhibiting Lateral Domain Formation in Lipid Bilayers: Simulations of Alternative Steroid Headgroup Chemistries

3.1 Introduction

There is a growing amount of evidence that laterally segregated domains of lipids are an integral part of biological membrane structure and function. These domains, referred to as lipid rafts, are now appreciated as a vitally important functional component of signaling and organization in the cell [176-178]. Experimental models of rafts have been studied extensively through synthetic lipid bilayers, with an emphasis on the biophysical interactions between low- and high-melting lipids and cholesterol [27, 32, 33, 104]. The role of steroids in promoting domain formation in these model systems has received a great deal of attention. Cholesterol decreases chain entropy in neighboring lipids due to its rigid ring structure, and associates more readily with ordered, saturated chains than with disordered, unsaturated chains. Chemical alterations to the steroid rings and hydrocarbon tail of cholesterol can lead to a decrease in domain formation [179-190].

The role of the polar headgroup is a less well understood aspect of steroid-induced domain formation. Removing the hydroxyl headgroup altogether or substituting it with more bulky groups has a detrimental effect on phase separation [179, 181, 182, 188], while replacing it with a charged group has a variety of effects [179, 189]. Of great interest is the difference between cholesterol and its oxidation product, cholestenone (4-cholesten-3β-one). This reaction is catalyzed in certain bacteria and its affect on the host membrane is postulated as necessary for pathogenesis [191]. Though cholesterol and cholestenone differ only in the replacement of the hydroxyl group with a keto group and in the shift in position of one double bond (from the B ring Δ^5 to the A ring Δ^4 position), cholestenone's propensity to form ordered domains is substantially reduced [179, 181, 182, 187, 188, 192]. In fact, it has been demonstrated that cholestenone can *inhibit* domain formation, making it one of the few identified domain inhibiting steroids [179, 188] and worthy of deeper study. It is unknown why this small chemical change leads to such a substantial difference in behavior, or if there is a common mechanism that operates amongst these domain-inhibiting steroids.

Atomistic computational molecular dynamics (MD) simulations have been used extensively to characterize the effect of steroids on lipid bilayers[36, 193, 194]. More recently, coarse-grained MD simulations have been developed to extend the access of computational techniques, allowing larger systems and simulations on the microsecond timescale. For example, using the Martini coarse grain force fieL_d[133], cholesterol flip-flop[41, 142] and lateral phase separation[195] have been studied. By their very nature, however, coarse-grained simulations are limited as a strategy for studying the effects of small changes in chemistry, as is the case in comparing cholesterol and cholestenone. In this current work, we have overcome this by systematically changing the properties of the steroid headgroup as a means of modeling the effects of altered chemistry. By isolating single physical variables (e.g. headgroup hydrophobicity), our computational strategy allows us to make fundamental connections between physical phenomena (e.g. domain formation) and basic chemical characteristics.

In the Martini coarse-grain force-fieL_d, multiple atoms are represented as single beads, with each falling into one of four categories: non-polar (further classified from most non-polar [C1] through least non-polar [C5]), intermediately polar (including either hydrogen bond donating [Nd] or accepting [Na]), polar (from most polar [P5] through least polar [P1]), and charged. Standard parameterization of cholesterol represents the hydroxyl group as type P1[133]. Here, we have run a series of simulations in which we have changed the cholesterol headgroup type in order to represent a range of hydrophobicities, modeling the physical differences with cholestenone. The geometry of the molecules, namely the bonds lengths and angles, was not altered from the cholesterol parameterization presented previously[133]. The bilayers we use here are similar to those previously shown to exhibit lateral phase separation[195], consisting of 256 di-16:0PC lipids, 256 di-18:2PC lipids, and 128 steroids at full hydration. Each of the eight systems were simulated for 3.5 μs, and the final 1.5 μs used for analysis.

3.2 Methods

Parameters for the Martini CGMD force fieL_d were used as previously presented [133, 170], except for the modified steroids. In order to create these modified steroids, the headgroup of cholesterol was changed from a type SP1 bead, the S denoting it as a ring

type bead and the P1 denoting it as a polar bead, to a range of other bead types. These include the non-polar beads (from most non-polar to least) SC1, SC3, and SC5, the intermediately polar beads SNa (hydrogen bond accepting) and SNd (hydrogen bond donating), and the polar bead SP1 and the more polar SP4. For simplicity, we omit the S in the bead type name. In each of these steroids, the geometry of the molecule, specifically the bonds and angles, was unchanged from the cholesterol parameters[133]. Figure 3-1A illustrates the steroid molecule and steroid headgroup in this CG representation.

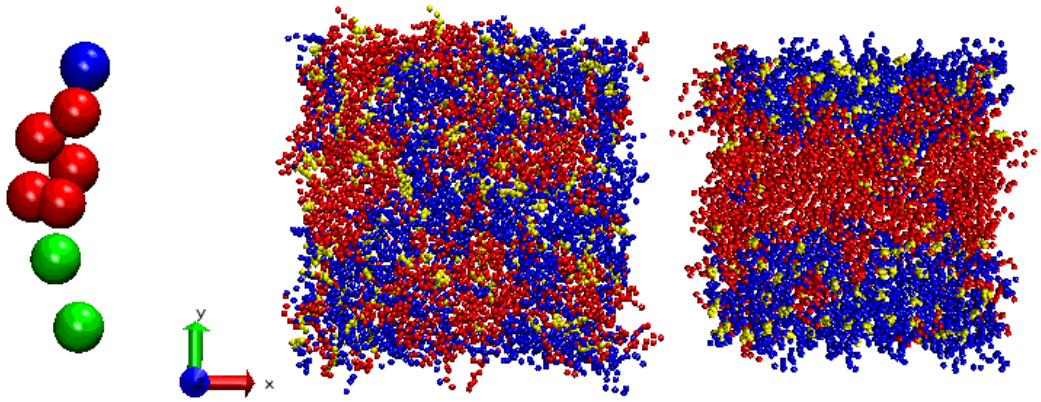

Figure 3-1 Cholesterol and Domain Formation - A) Steroid molecule (green=tail, red=steroid rings, blue=headgroup). In this set of simulations we alter the hydrophobicity of the headgroup bead to observe changes in domain formation. B) Starting configuration, obtained from a 400 ns simulation at 400 K, designed to remove lateral separation, though some degree of self-association remains. Note that the steroid does not co-localize preferentially with either lipid. C) This is in contrast with a bilayer that does display lateral separation and steroid-saturated lipid co-localization at 298K.

Each of the steroid containing systems consisted of 256 di-18:2PC, 256 di-16:0PC, 128 steroids, and 9,941 water beads. Using a similar system, and the P1 type bead to represent the cholesterol headgroup, phase separation and preferential co-localization of the steroid with the saturated lipid was recently observed [195]. In order to obtain a starting configuration without separation, we performed a simulation for 400 ns at 400 K.The resulting structure is show in Figure 3-1B. Though there is still some degree of self-association (the saturated lipid interacts with the saturated lipid, and the di-unsaturated lipid interacts with the di-unsaturated lipid), it is much more mixed than the separated system, found using the P1 type steroid headgroup, shown in Figure 3-1C.

Additionally, note that in the starting configuration the steroid does not preferentially co-localize with either of the lipid types, while in the phase separated system the cholesterol is associated with the saturated lipid. From this starting configuration, substitutions to the steroid headgroup were made and production simulations run. For the system without steroid, the same starting configuration was used, with the steroids removed.

Simulations were run using Gromacs version 3.3.3 [163]. Simulations were performed using periodic boundary conditions and a constant number of particles (N), pressure (P), and temperature (T). We applied the Berendsen temperature and pressure coupling scheme with relaxation times of 0.1 ps and 0.5 ps respectively, at a temperature of 298 K and a reference pressure of 1 bar. The pressure scheme was applied in a semi-isotropic manner resulting in a tensionless bilayer. We utilize the convention of describing the effective time sampled as a four-foL_d increase over the simulation time, due to a "smoothing" of the energy profile in coarse grain simulation [133]. Simulations were run with a time step of 30 fs for a duration of 3,500 ns effective time, with coordinates recorded every 1.2 ns.

3.3 Results

Equilibration of the bilayers is first analyzed by the lateral area, as presented in Figure 3-2. Relaxation of the lateral dimensions occurs in two steps. The first is a rapid decrease from the initial box length of 14.8 nm, which occurs over the first few nanoseconds. The initial configuration was attained from a high temperature simulation at 400 K, which leads to an increased lateral area, which quickly decreases during the production simulations at 298 K. There is then a gradual decrease in box size, which occurs over hundreds of nanoseconds, most noticeably in the bilayers containing polar and intermediately polar steroid headgroups. Steroids that are able to interact closely with the saturated lipid, like cholesterol, cause the formation of a more ordered phase laterally separated from the rest of the bilayer, characterized by increased thickness and decreased lateral area. Therefore, a smaller area may correlate to a larger degree of phase separation. Using timepoints after 2 microseconds, the steroids with non-polar headgroups have average box lengths of 13.44 nm (C1=13.43 nm, C3=13.47 nm, C5=13.42 nm), while the polar and intermediately polar headgroups have an average of

13.31 nm (Na=13.35 nm, Nd=13.26 nm, P1=13.31 nm, P4=13.34 nm), which is a 2% decrease in area. The bilayer without any steroid has a smaller area and though it exhibits phase separation, the smaller area is predominantly due to the fact that it has less molecules (13.16 nm).

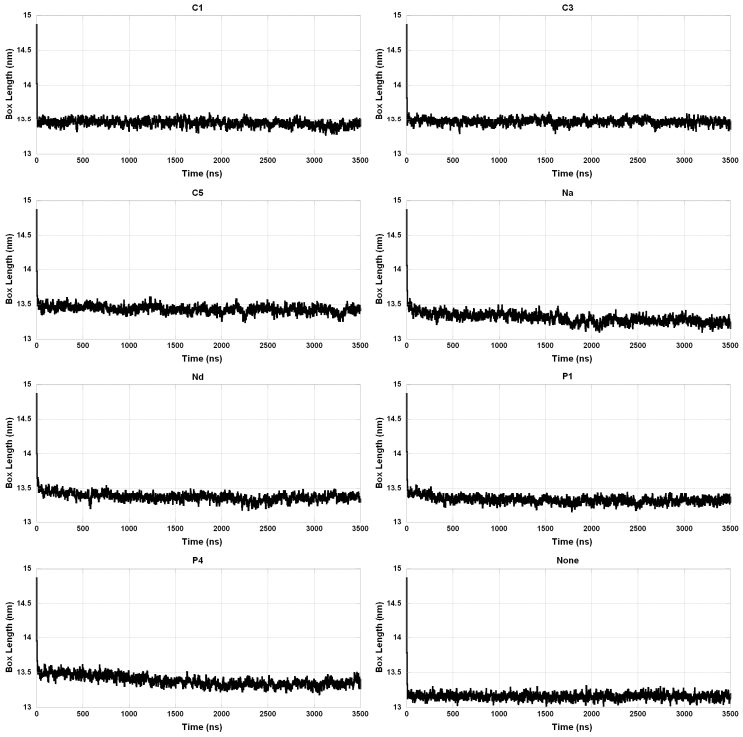

Figure 3-2 CGMD Area Equilibration - The lateral area of the box dimensions reveals both a rapid decrease over the course of nanoseconds, and a longer, gradual decrease over hundreds of nanoseconds. The two lateral axes have equal lengths for each of these simulations.

Figure 3-3 directly quantifies the size of the largest disordered domain in each of the systems. This is done by counting the number of di-unsaturated lipids which are in contiguous contact with each other, defined by a 1.2 nm cutoff using the phosphate groups. In each bilayer, the initial domain size is low: 44 lipids for the top leaflet and 35 lipids for the bottom leaflet. However, the degree of lateral separation increases rapidly over the first few hundred nanoseconds, from the initial high-temperature derived configuration. Each system appears to have equilibrated after ~2 microseconds of dynamics. However, the bilayers clearly equilibrate at different values, depending on the steroid headgroup. Figure 3-4 provides the average values of the domain sizes, for

timepoints after 2 microseconds. The polar and intermediately polar steroid headgroups cause nearly complete lateral separation, in which almost all of the 128 di-unsaturated lipids per leaflet are in the domain. The bilayer with the type C5 steroid headgroup (the most polar of the non-polar group) clearly displays less than complete separation. The type C1 and C3 steroid headgroups, the most non-polar headgroups, lead to an even smaller degree of separation, with an average amount of 2/3 of the lipids participating in the domain. However, these bilayers with non-polar steroid headgroups show a wider range of domain sizes, with at times higher and lower degrees of lateral separation being observed. The system without any steroid does exhibit lateral separation, with an average size slightly less than the bilayer with steroids with type C5 headgroups and greater than the type C1 and C3 headgroups. That these non-polar steroid headgroups appear to cause less separation than the system without any steroid, suggests that they model the behavior of the experimentally observed steroid domain inhibitors, such as cholestenone [179, 188].

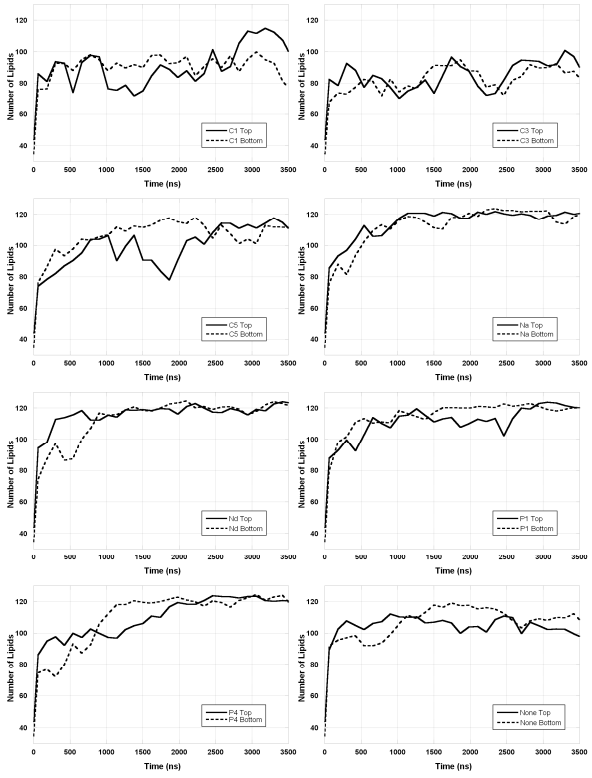

Figure 3-3 Domain Formation Timeseries - The extent of domain formation is quantified, by calculating the number of unsaturated lipids in contiguous contact. Each timepoint in this figure is the average of 100 frames. Lateral behavior appears approximately converged after 2 microseconds.

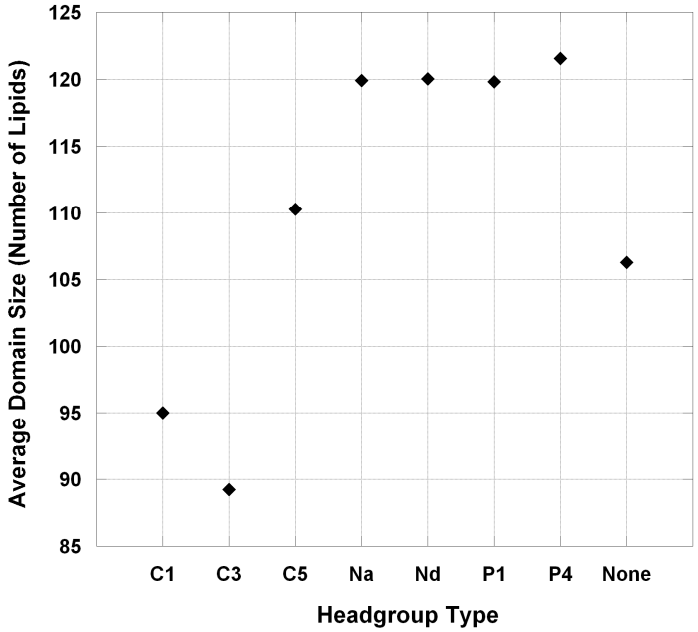

Figure 3-4 Steroid Headgroup and Domain Size - The average size of disordered domains, using all timepoints after 2 microseconds. Differences in steroid headgroup lead to differences in the extent of domain formation.

Figure 3-5 presents a more complete view of the lateral localization of the bilayer components. The system which contains no steroids shows lateral separation between saturated and di-unsaturated lipid. However, in agreement with Figure 3-3 and Figure 3-4, those bilayers which contain polar (P1 and P4) and intermediately polar (Nd and Na) headgroups show an even more distinct separation between the saturated and di-unsaturated lipid than the steroid free bilayer. Those bilayers also show strong co-localization of the steroid with the saturated lipid. The bilayer containing the steroids with C5 headgroups shows separation between lipids, but weaker co-localization of the steroid and saturated lipid. The bilayers containing the steroids with C3 and C1 headgroups show considerably less separation between the saturated and di-unsaturated lipids and far weaker co-localization of the steroid with the saturated lipid. Again, these bilayers show less separation than the system without any steroid, suggesting that the steroids with non-polar headgroups are functioning as domain inhibitors.

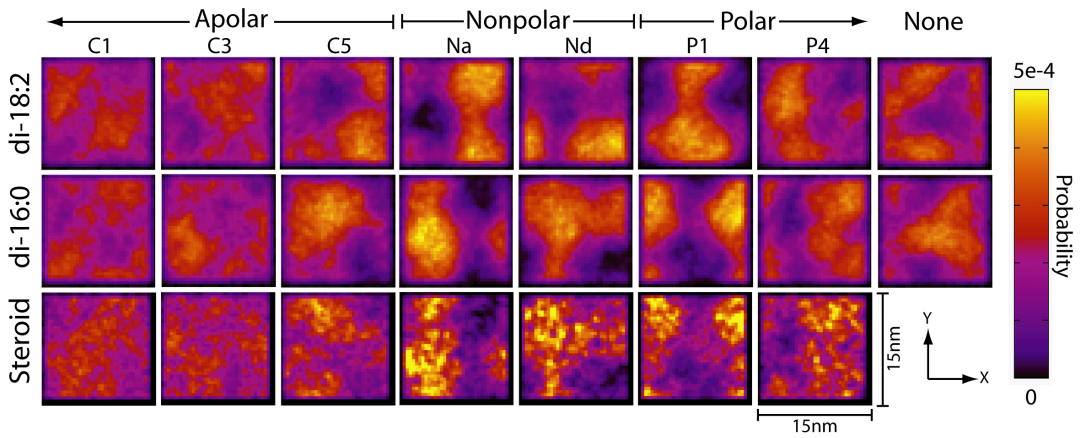

Figure 3-5 Lateral Densities showing Domain Formation/Inhibition - Density showing lateral localization of di-16:0PC, di-18:2PC, and steroids, illustrating in certain cases lateral separation of lipids and co-localization of steroid with the saturated lipid, using timepoints after 2 microseconds. Indentations on axes indicate lengths of 2 nm.

These differences in domain formation result from differences in the steroid molecule orientation. Until recently, it was thought that the upright orientation of cholesterol, where the molecule is parallel to the lipid tails and the headgroup is at the lipid-water interface, was the only favorable steroid conformation. However, cholesterol has been shown to favor an orientation perpendicular to the bilayer normal axis, buried in the hydrophobic core while in poly-unsaturated lipid bilayers, using neutron diffraction [42] and coarse-grain MD [41, 142]. Additionally, in a single component, non-phase separated simulation, a keto-sterone (closely related to cholestenone) was also shown to adopt a perpendicular orientation [196]. As shown in Figure 3-6, our results demonstrate that in bilayers containing saturated and di-unsaturated lipid, an increase in headgroup hydrophobicity triggers a switch to this buried, perpendicular orientation. Those steroids with polar and intermediately polar headgroups have lower tilt values, with an average of 21°, similar to that of cholesterol in di-16:0PC found through experiment [197] and computation [198]. These steroids also each have maximal headgroup density at the lipid-water interface, though the steroid with the intermediately polar, hydrogen bond donating headgroup may favor slightly deeper bilayer penetration. Steroids with the C5 headgroup display a tri-modal headgroup distribution, thus maintaining an equilibrium between the upright and perpendicular orientations.

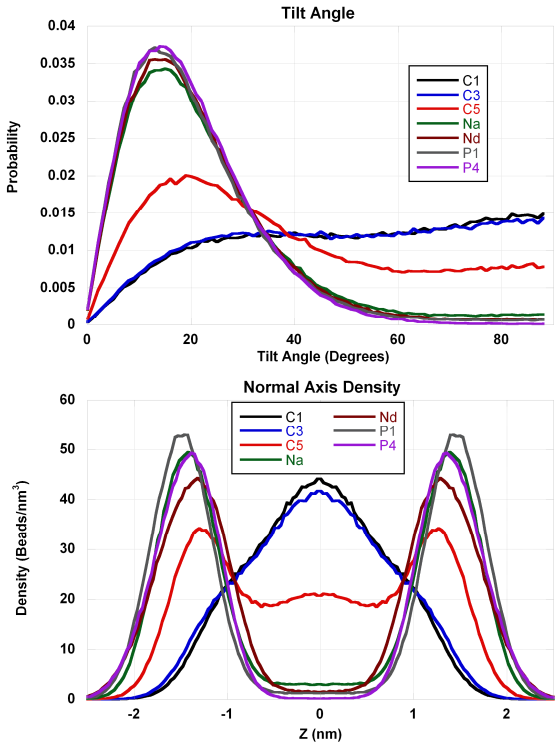

Figure 3-6 Steroid Orientation - Increasing headgroup hydrophobicity shifts the bilayer normal axis tilt (top) and headgroup depth (bottom), from the typical sterol orientation to a buried perpendicular orientation.

Figure 3-7 presents snapshots from the P1 and C1 simulations illustrating the differences in steroid orientation and lateral organization. In the top panel, the steroid has a polar headgroup, and is in the upright orientation, promoting phase separation. In the lower panel, steroids with hydrophobic headgroups insert in the bilayer center and inhibit phase separation.

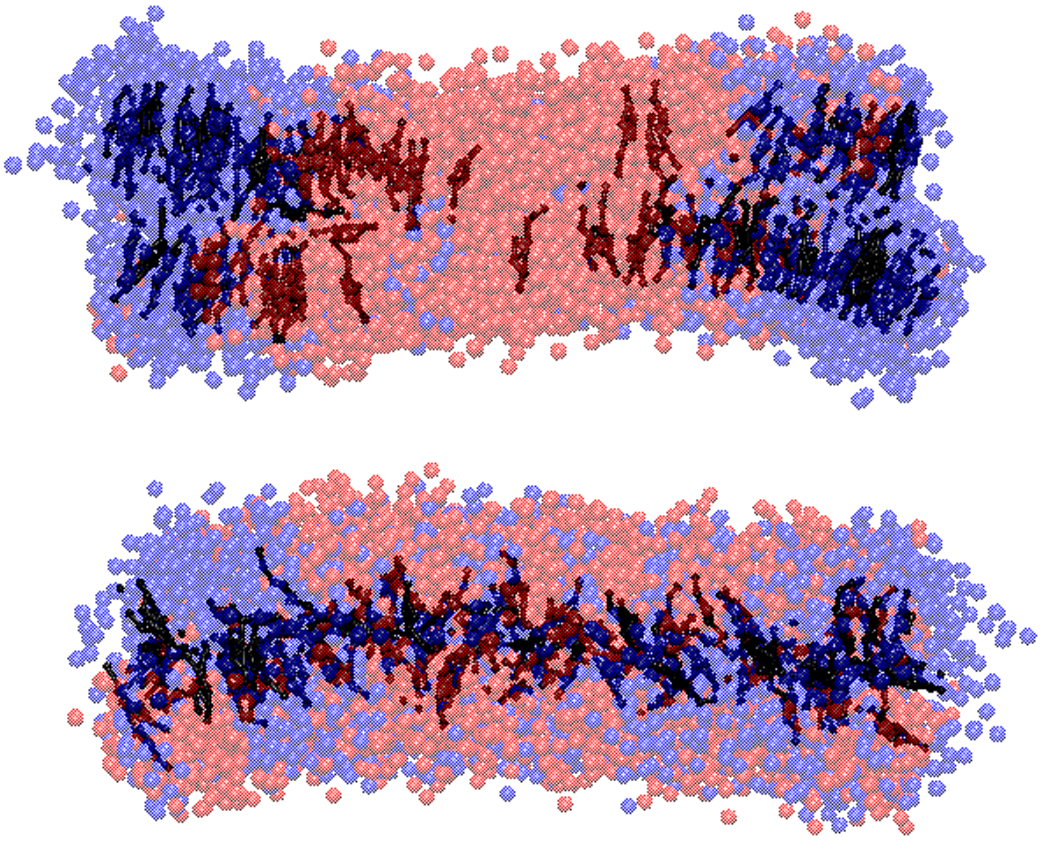

Figure 3-7 Steroid Orientation Snapshots – Snapshots illustrating differences in bilayers containing a polar (type P1, top panel) and apolar (type C1, lower panel) steroid headgroup. Saturated lipid = blue, unsaturated lipid = red, steroid = black, water omitted for clarity.

3.4 Discussion

We have used coarse grain molecular dynamics simulations in order to investigate the relationship between steroid headgroup hydrophobicity and lateral domain formation. We find that steroids with polar headgroups orient parallel to the lipid tails with their headgroups at the lipid-water interface. This allows the stiff, steroid rings to order the neighboring lipid tails, promoting formation of liquid-ordered domains. As the hydrophobicity of the steroid headgroup increases, we see a distinct transition from domain enhancing to domain inhibiting. The more hydrophobic headgroups lead to deeper insertion into the bilayer center and a more tilted orientation. These changes in orientation are correlated with changes with the bilayer lateral organization, suggesting

that steroid orientation determines the molecule's ability to promote or inhibit domain formation.

Until recently, it was thought that the canonical orientation of cholesterol was the only favorable steroid conformation. However, cholesterol has been shown to favor a buried, perpendicular orientation while in poly-unsaturated lipid bilayers using neutron diffraction [42, 43] and coarse-grained molecular dynamics [41]. An all-atom molecular dynamics simulation showed that replacing the hydroxyl in cholesterol with a ketone, creates a steroid which is relatively unstable in a lipid bilayer and was observed to rapidly insert into the bilayer center and flip-flop during a brief 50 ns simulation [196].

Our results suggest that the steroid orientation determines whether the steroid is domain promoting or domain inhibiting, rather than a chemically specific mechanism. For example, it has been suggested that cholesterol forms complexes with lipids with a defined stoichiometry [37, 38]. Our results suggest that the specific chemical interactions between cholesterol and its lipid neighbors, such as through hydrogen bonding, are unnecessary for explaining the ability of the steroid to promote phase separation. Interestingly, a series of brief all-atom simulations suggestion a correlation between steroid tilt and its ability to order neighboring lipids [198].

Similarly, steroid domain inhibition does not require a chemically specific mechanism. This is in agreement with experiments, which have found that steroid domain inhibitors have a wide range of structures, differing from cholesterol in their tails, rings, and headgroups [179, 188]. Rather than distinct specific mechanisms for these differing molecules, their ability to inhibit domain formation stems from a lack of stability in the upright orientation.

In conclusion, our results, which take advantage of a reductionist, computational strategy, demonstrate that the role of cholesterol's headgroup is to anchor the steroid in the upright orientation, allowing the stiff, steroid rings to order the neighboring lipid tails, and thus promoting formation of lateral domains. Changing the physico-chemical properties of the headgroup, mimicking the difference between cholesterol and cholestenone, causes the steroids to favor a fully inserted, perpendicular orientation. Our results demonstrate that steroids in this conformation inhibit lateral domain formation,

likely by disrupting the interactions between neighboring lipid chains that would otherwise favor domain formation. We suggest that the destabilization of the upright orientation is a common mechanism of domain inhibiting steroids.

4 Interleaflet Interaction and Asymmetry in Phase Separated Lipid BilayersIntroduction

Biological membranes are far from homogeneous, and the list of ways in which they differ from the canonical fluid mosaic model [45] is ever expanding [13]. Of these, two appear to have particular significance in dictating how cells organize their membrane bound protein machinery. First, phase separation in the plane of the bilayer is now thought to be an important functional feature of biological membranes [176, 178, 199-201]. Biophysical experiments and computational studies of synthetic model systems (e.g. lipid vesicles) have shown unambiguously that cholesterol preferentially associates with saturated lipids and that this induces a phase separation of liquid-ordered (L_o) and disordered (L_d) domains [27, 32, 33, 51, 72, 104, 195].

A less-well understood aspect of biological membranes is the consequence of different lipid and cholesterol compositions in the two leaflets [1, 99-104]. For example, in mammalian plasma membranes the majority of sphingomyelin is found in the outer leaflet [105]. Since sphingomyelin is thought to be the primary component of lipid rafts [202], its asymmetric distribution has raised a set of important questions: how does the compositional asymmetry affect the phase behavior of the inner leaflet? That is, if the outer leaflets of biological membranes contain L_o domains, while the inner leaflet composition is such that in isolation it should be uniformly disordered [51, 106], then what thermodynamic characteristics does that inner leaflet actually posses? How are the two leaflets coupled? Does *compositional* asymmetry lead to *phase* asymmetry (i.e. L_o and L_d domains directly opposite one another in the two leaflets), or conversely, are domains induced in the inner leaflet resulting in phase symmetry?

That biological membranes are compositionally asymmetric has been repeatedly verified [1, 99-104]. However, experiments on domains in biological membranes rely upon methods such as detergent extraction that are unable to resolve the phases of the individual leaflets. Therefore, validating the existence of phase asymmetry in biological membranes remains very difficult, making critical the insights available from experiments on model, synthetic lipid bilayers. Among the first such experiments that addressed this question—if and how one leaflet affects the structure and thermodynamic

phase behavior of an apposed leaflet—used asymmetric ion distributions to investigate how the two leaflets of a bilayer are coupled. The results were ambiguous: in some cases an interleaflet structural perturbation could be observed by an altered phase transition temperature [203, 204]; in other cases no effect was observed [205].

More recently, fluorescence microscopy experiments using synthetic lipid bilayers with an asymmetric lipid composition, along with dyes that favor either the L_o or L_d phases, have yie$L_d$ed significant insight, though again no clearly consistent picture has emerged. Some experiments have suggested that an L_o domain in one leaflet can induce an L_o domain in an opposing leaflet that would, on its own, be L_d [95, 105, 107-109]. Thus, while these bilayers are compositionally asymmetric, they were suggested to be phase symmetric. For example, one experiment studied the effect of an L_o/L_d phase separated leaflet composed of a 2:2:1 mixture of DOPC:DPPC:Cholesterol on an opposing leaflet composed of a mixture of solely unsaturated lipids (DOPC, DOPE and DOPS) [109]. Visual inspection of the partitioning of one L_o-favoring dye and another L_d-favoring dye led to the conclusion that an L_o domain had been induced in the leaflet composed solely of unsaturated lipids. On the other hand, alteration of phase-state across leaflets of asymmetric bilayers appears to be highly sensitive to the lipid constituents. A separate experiment on a compositionally asymmetric bilayer containing a domain forming mixture of brain PC, brain SM, and cholesterol in one leaflet, failed to alter dye partitioning in an opposing leaflet composed of DOPC, meaning that this particular compositionally asymmetric bilayer remained phase asymmetric [109].

While striking qualitative results, these findings left open the possibility that intermediate levels of L_o-favoring dye partitioning indicate the existence of an intermediate phase in the regions opposite an L_o domain. This possibility was further elaborated in the experiments of Collins et al. [107]. Again using dye partitioning experiments in compositionally asymmetric bilayers, three levels of intensity were observed. Using an elegant free-energy model, the study identified three corresponding configurations of bilayer-spanning phases across the two leaflets: L_o/L_o, L_d/L_d and L_o/L_d. The latter, identified in the experiments as regions with an intermediate intensity between

L_o and L_d, was termed a bilayer-spanning 'mixed' phase, where the lipid components are likely more ordered than L_d, but less ordered than L_o [107].

One important clarification regarding these experiments on asymmetric bilayers that has direct bearing on the simulation strategy employed here is that they were all performed under non-equilibrium conditions. Specifically, all measurements were made immediately after formation of the asymmetric bilayers, ensuring that over the time-scale of the experiments there is no phospholipid flip-flop between the leaflets[95, 107-109]. That is, as Collins et al [107] pointed out, in experiments under these conditions the lipid chemical potentials are not necessarily equal in the two leaflets. Performing the experiments in this way most closely models the thermodynamic state of biological membranes, where the lipid asymmetry is established by enzymes called flipases, which utilize ATP in maintaining the non-equilibrium, asymmetric distributions of lipids [206].

A second important issue regarding phase asymmetry is the observation that in compositionally symmetric bilayers there is a tendency for L_o domains in opposing leaflets to overlay, or register (that is, to be phase symmetric) [92-95], though again a number of exceptions have been observed [96-98]. Similar inconsistencies have been observed in the case of solid domains, which showed registration for one lipid mixture, but not for another [207]. Theoretical treatments have explored the energetic underpinnings of domain registration (phase symmetry) *vs.* anti-registration (phase asymmetry), suggesting that a fine balance between an interleaflet line tension at the bilayer mid-plane and an intraleaflet tension at the interface of domains within each leaflet plays a central role [208-212]. Nevertheless, despite the technically elegant accomplishments of recent experiments and theoretical treatments, it currently remains undetermined exactly how leaflets of a bilayer are coupled together, why certain mixtures induce domain formation across the bilayer and others do not, and whether biological membranes are phase symmetric or asymmetric [208, 213].

In order to examine the interactions between leaflets in bilayers with at least one phase separated leaflet, we make use of computational molecular dynamics (MD) simulations. Previously, all-atom MD simulations have been used to study the structure of single phase lipid bilayers with a compositional asymmetry of lipids and ions, for

example observing the effects on the bilayer electrostatic potential [36, 214-223]. However, domain formation requires time- and length-scales inaccessible to all-atom simulations. To address this, coarse-grained MD (CGMD) force fieL_ds have been developed. In CGMD, atoms are grouped together into multi-atomic units, reducing the computational cost and allowing investigation of longer time- and length-scales. In particular, using the Martini CGMD force fieL_d [133], bilayers with compositional asymmetry were found to be stable over a multi-μs simulation [224] and *de novo*, registered L_o domain formation in a compositionally symmetric bilayer has been observed [195]. Additionally, CGMD simulations have studied possible interleaflet effects due to anti-registered (phase asymmetric) solid domains [225] and solid supported lipid bilayers [226]. The success of these simulations suggests that this type of computational modeling is a potent strategy for understanding the effects of compositional asymmetry on bilayer structure and phase behavior.

In this study, we have used CGMD to model phase separated, compositionally symmetric and asymmetric lipid bilayers. The asymmetric bilayers are initiated with a single-component, single phase (L_d) top leaflet opposing a three-component, laterally phase separated (L_o/L_d) bottom leaflet. Over the course of the simulations, we find an increase in the degree of lipid order in the region of the top leaflet that is opposite an L_o domain, as quantified through lipid chain tilt angle and average lipid chain order parameter. We have also found a decrease in order in the region of the single-component, top leaflet opposite an L_d domain. Further, we report a novel finding regarding the induction of local curvature in the single-component leaflet of the asymmetric bilayers that may be correlated with this change in order.

We have also found an intriguing connection between lipid chain-length and phase symmetry in compositionally symmetric bilayers. Early models of isolated L_o and L_d domains that were based upon NMR measurements suggested the importance of the relative lengths of acyl chains and cholesterol in dictating the mid-plane organization of the molecular constituents, with a focus on the ability of the molecules to inter-lock [39, 227]. Inspired by this paradigm, we have run a series of simulations in which we have varied the length of the saturated lipid in only the L_o domains, and show that in compositionally

symmetric bilayers L_o domains containing lipids with shorter chains are in register (phase symmetric), whereas those containing lipids with longer-chains are anti-registered (phase asymmetric). By varying the mole ratios of the constituent lipids, we have further explored the extent of this registration phenomenon and suggest a fine balance between bilayer curvature stress and domain mixing. These findings highlight how a height-mismatch between the L_o and L_d domains within a leaflet can impact interleaflet organization. Collectively, our findings expand upon the current understanding of how compositional asymmetry is coupled to the phase behavior and structure of individual leaflets, offering a revised and higher-resolution picture of the biophysics of interleaflet coupling.

4.1 Methods

4.1.1 System Construction

Bilayer systems were built using the Martini CGMD force fieL_d [133], which uses an approximate mapping of 4 non-hydrogen atoms per bead. In addition to cholesterol, we have used four different lipids: CG di-4:0 roughly corresponds to the all-atom structure of di-16:0; di-5:0 corresponds to di-20:0; di-6:0 corresponds to di-24:0; and di-4:2 corresponds to di-18:2. First, we simulated three compositionally symmetric, ternary bilayers, all of which phase separated over the course of the simulations. These 2:2:1 systems consisted of 256 unsaturated lipids (di-4:2PC), 256 saturated (either di-4:0PC, di-5:0PC, or di-6:0PC) lipids, 128 cholesterols, and ~10,000 water beads. The bilayer containing di-4:2PC, di-4:0PC and cholesterol is identical to the one we used previously to model L_d/L_o domain formation [144]. The starting configuration for each of the symmetric systems was obtained through a 400 ns simulation of a 2:2:1 mixture of di-4:2PC, di-4:0PC, and cholesterol, at an increased temperature (400 K) which randomized the lateral distribution of lipids in order to avoid starting configuration bias. Symmetric bilayers containing longer-chain lipids as the saturated lipid component used the same starting configuration, with the only modification being the addition of either 1 (di-5:0PC) or 2 (di-6:0PC) acyl chain groups (type C1) onto the *sn*-1 and *sn*-2 chains of the di-4:0PC. Symmetric bilayers containing a different molar ratio, either 1:2:1 or 4:2:1, were built such that they maintain as closely as possible the same number of total lipids

as in the other symmetric bilayers. As described below, based on visualization and quantitative analysis we conclude that each saturated lipid forms the L_o phase with cholesterol, rather than the gel phase [140].

In order to buiL_d asymmetric bilayers, it was necessary to ensure that each leaflet of the bilayer would have the same lateral area. Pairing together leaflets with different areas could lead to a compression or expansion, an artifact which would alter the structure of the bilayer [121, 223, 228] and possibly cause buckling. That we were successful in avoiding this artifact is detailed below. Thus, in order to assemble a bilayer containing a ternary, laterally separated leaflet opposite a single-phase, single-component leaflet we first needed to perform a series of compositionally symmetric simulations. This was done so as to determine the appropriate number of lipids to include in each leaflet of the asymmetric bilayers. Then, using the areas determined from these equilibrated symmetric bilayer simulations, we built asymmetric bilayers that consist of one ternary leaflet and one single-component (di-4:2PC), single-phase leaflet. In order to determine the size (i.e. number of lipids) of this di-4:2PC leaflet needed to match the equilibrated areas of the ternary leaflets, a series of relatively brief (500 ns) simulations of single-component, di-4:2PC bilayers were run in order to test how the area depends upon system size. This series of simulations resulted in an average area per di-4:2PC of 0.742 nm^2. Based on this analysis, a leaflet composed of 237 di-4:2PC lipids matched the area of the compositionally symmetric bilayers containing di-4:0 PC; 233 di-4:2PC lipids matched the compositionally symmetric bilayer containing di-5:0PC; and 232 di-4:2PC lipids matched the compositionally symmetric bilayer containing di-6:0. Each asymmetric bilayer was then built by joining the corresponding top leaflet of the single component, di-4:2PC bilayer with the bottom leaflet of the symmetric, ternary bilayer (using its starting configuration, which was not yet phase separated), and then solvating in a water box of ~10,000 water beads. A symmetric, single-component bilayer containing two leaflets each composed of 237 di-4:2PC lipids was also simulated. Additional systems were built, in which 10, 20, or 30 cholesterol molecules were added to this bilayer, in order to provide a control that was necessary for handling the analysis of systems in

which cholesterols were found to flip-flop between leaflets. The set of simulated bilayers along with their leaflet lipid and cholesterol distributions are summarized in Table 4-1.

Top Leaflet	Bottom Leaflet
Symmetric Simulations	
di-4:2, di-4:0, Chol (128:128:64)	di-4:2, di-4:0, Chol (128:128:64)
di-4:2, di-5:0, Chol (128:128:64)	di-4:2, di-5:0, Chol (128:128:64)
di-4:2, di-6:0, Chol (128:128:64)	di-4:2, di-6:0, Chol (128:128:64)
Symmetric Simulations (Altered Ratios)	
di-4:2, di-5:0, Chol (80:160:80)	di-4:2, di-5:0, Chol (80:160:80)
di-4:2, di-5:0, Chol (184:92:36)	di-4:2, di-5:0, Chol (184:92:36)
Asymmetric Simulations	
di-4:2 (237)	di-4:2, di-4:0, Chol (128:128:64)
di-4:2 (233)	di-4:2, di-5:0, Chol (128:128:64)
di-4:2 (232)	di-4:2, di-6:0, Chol (128:128:64)
Control Simulations	
di-4:2 (237)	di-4:2 (237)
di-4:2 + 5 Chol (237:5)	di-4:2 + 5 Chol (237:5)
di-4:2 + 10 Chol (237: 10)	di-4:2 + 10 Chol (237: 10)
di-4:2 + 15 Chol (237:15)	di-4:2 + 15 Chol(237:15)
di-4:2, di-4:0 (128:128)	di-4:2, di-4:0, Chol (128:128:64)
di-4:2 (227)	di-4:2, di-4:0, Chol (128:128:64)

Table 4-1 Symmetric and Asymmetric Bilayer Simulated - Lipid and cholesterol composition of the top and bottom leaflets in each simulation.

It is important to clarify that the lipid distribution in the simulated bilayers is intentionally in a non-equilibrium state. Though equilibration is typically an important criterion for convergence of particle-based molecular simulations, in this case the simulations are modeling a set of non-equilibrium experiments where lipid redistribution between the leaflets is not the appropriate convergence criterion. More specifically, in biological membranes compositional asymmetry is maintained by enzymes which

frequently require energetic input in the form of ATP [206]. In the absence of this enzymatic machinery, numerous experiments which have constructed model bilayers with compositional asymmetry have been careful to avoid phospholipid flip-flop, which leads to a loss of the asymmetry on a time-scale of hours to days [95, 97, 107-110, 229]. Therefore, in order to study the biologically relevant asymmetry in a simple biophysical model, experiments have been performed before the phospholipids have a chance to flip and equilibrate [95, 97, 107-110, 229]. Cholesterol, which flips much more quickly, does redistribute in the experimental time-frame. Our simulations therefore follow the strategy used in these experiments: we artificially create a compositionally asymmetric bilayer and describe its structure after equilibration of all structural features except for re-distribution of phospholipids between the leaflets. Convergence of these properties, which include alterations in local curvature, is described below. It is therefore appropriate that, on the time-scale of the simulations, no instances of phospholipid flip-flop are observed, and the leaflet phospholipid compositions do not change from the starting configurations through the duration of each simulation. Also appropriate to the experiments we are modeling, cholesterol redistribution between the leaflets is observed, and convergence of that aspect is carefully monitored and controlled for as described above and explained below.

4.1.2 Simulation Details

Simulations were run with Gromacs version 3.3.3 and 4.0.7 [230], using periodic boundary conditions and a constant number of particles (N), pressure (P), and temperature (T). The Berendsen pressure coupling scheme was applied in a semi-isotropic manner resulting in a tensionless bilayer, where the *xy*-axes define the lateral plane of the bilayer and the *z*-axis is normal to the global bilayer surface. We utilize the convention of describing the effective time sampled as a four-foL_d increase over the simulation time, due to a "smoothing" of the energy profile in coarse grain simulation [133]. Simulations were run with a time step of 30 fs for a duration of 12 μs effective time, at a temperature of 295 K [195]. The results presented here total more than 150 μs of simulation.

4.1.3 Analysis Details

Analysis of these simulations was performed using Gromacs [230], VMD [167], and a set of in-house Perl scripts. Based on equilibration of the lateral structure (Figure 4-1), all analysis was performed on timepoints starting after 2.4 μs, unless otherwise noted.

Analysis of per-leaflet density distributions required non-trivial assignment of cholesterol molecules. Cholesterol has been shown to flip-flop rapidly between leaflets, as well as to stably occupy intermediate states at the bilayer midplane, and thus in these instances ascribing a cholesterol to one of the leaflets can be somewhat ambiguous [41, 142]. For each cholesterol, we identified the closest lipid in the *xy*-plane in both leaflets (based on the position of the first bead in the acyl chain), and then used the minimum of the two distances in *z* between the cholesterol hydroxyl group and those lipids to assign it to a leaflet. In order to preserve the information on the relative density of cholesterol in the two leaflets, the density of cholesterol is normalized for the bilayer, while the lipid density is normalized per leaflet.

To analyze the degree of lipid order, we utilize the lipid chain segmental order parameter:

$$P_2 = \frac{1}{2}(3\cos^2\langle\theta\rangle - 1) \qquad \textbf{Eq 4-1}$$

Where θ is the angle formed by the bond segment and the global bilayer normal (*z*) axis. Data presented is the average of each bond segment, as in [195].

A parameter we have used for analyzing the dynamics is the lipid rotational autocorrelation function, defined as:

$$C(\tau) = \frac{\langle \vec{C}_i(t) \cdot \vec{C}_i(t+\tau) \rangle}{\langle \vec{C}_i(t) \cdot \vec{C}_i(t) \rangle} \qquad \textbf{Eq 4-2}$$

where $\vec{C}$ is the vector connecting the lipid backbone groups, τ is the lag time, and the brackets indicate an average over time (*t*) and lipids (*i*). The resulting function was approximated as an exponential decay:

$$C(\tau) \approx e^{(-\tau/\chi)} \qquad \textbf{Eq 4-3}$$

where χ is the characteristic decay time. Fitting using a larger number of terms, such as through a double [231] or triple [232] exponential function yieL$_d$s more accurate fitting.

However, using Eq 4-3 provided reasonable agreement (R^2>0.94) and allowed us to succinctly communicate the change in structure induced by interleaflet communication.

A second parameter we have used to analyze the bilayer dynamics is the lateral diffusion coefficient, defined as:

$$\left\langle r^2 \right\rangle = 4Dt \qquad \text{Eq 4-4}$$

where $\left\langle r^2 \right\rangle$ is the 2-dimensional mean squared displacement, *D* is the diffusivity, and *t* is time. The MSD is linear in the long time limit, and thus the slope of the MSD plotted against time was used to determine *D*.

4.2 Results

4.2.1 Compositional Asymmetry

In this section we present results on how lipid compositional asymmetry affects the structure and dynamics of bilayers containing a single-component leaflet opposite a three-component, phase separated leaflet. As controls, we have run compositionally symmetric bilayers as well. As described in detail in the Methods section, the top leaflet of each of the simulated, compositionally asymmetric bilayers is composed of di-4:2PC, a coarse-grained model of di-18:2PC which on its own (in a compositionally symmetric, single-component di-4:2PC bilayer) is in the L_d phase at the simulated temperature [195]. The bottom leaflets of the compositionally asymmetric bilayers are composed of a ternary mixture of di-4:2PC, cholesterol, and a saturated lipid: either di-4:0PC (a CG representation of di-16:0PC), di-5:0PC (representing di-20:0PC), or di-6:0PC (representing di-24:0PC). The di-4:2PC, di-4:0PC and cholesterol mixture has been shown to phase separate in previous simulations of compositionally symmetric bilayers, with the di-4:2 lipids segregating into an L_d phase region, and the saturated lipid and cholesterol collectively forming an L_o phase region [144, 195]. Throughout the text, bilayers are identified by citing the lipid content of the top and bottom leaflets as [top]/[bottom]. For example, [di-4:2]/[di-4:2, di-4:0, Chol] indicates a single-component leaflet on top, and a ternary, phase separated leaflet on the bottom. Table 4-1 provides a summary of the simulated bilayers.

In order to ensure convergence of domain structures within each leaflet, we have quantified both the bilayer lateral area and the domain size. As a representative example, Figure 4-1 presents results from the symmetric [di-4:2, di-4:0, Chol]/[di-4:2, di-4:0, Chol] and the asymmetric [di-4:2]/[di-4:2, di-4:0, Chol] bilayers, showing nearly complete L_o/L_d phase separation in the leaflets containing ternary mixtures within the first 2 μs of the simulations [144, 195]. The rate and extent of domain formation was quantified by the largest number of di-unsaturated lipids in contact with each other (defined by a 1.2 nm cutoff between phosphate groups [144]). Figure 4-1 also shows the equilibration of the bilayer lateral area (*xy*-dimensions), a parameter that needed to be carefully monitored in the case of the asymmetric bilayers (as described in section 4.1 Methods). In the symmetric, single phase bilayers ([di-4:2]/[di-4:2], and in the control simulations containing cholesterol) the lateral areas equilibrate within the first 10 ns of the simulations. Slower area convergence in the ternary mixtures (~2 μs) is due to the co-localization of cholesterol with the saturated lipid and resultant area condensation [36, 148, 233-235]. The equilibration of domains and bilayer areas in the simulations containing longer-chain lipids is similar (data not shown). We conclude that the time-scale of our simulations is sufficient to observe converged behavior, and we have utilized time-points after 2.4 μs for all analysis. Other properties that we discuss below (lipid tilt, diffusion and local curvature) are also converged on this time-scale.

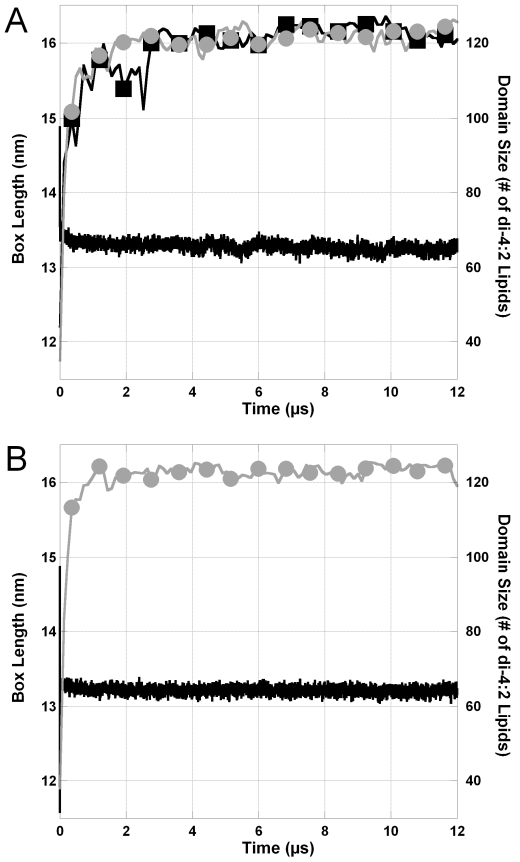

Figure 4-1 Lateral Equilibration - Representative timeseries showing equilibration of the simulations on the μs timescale. (A) [di-4:2, di-4:0, Chol] / [di-4:2, di-4:0, Chol]. (B) [di-4:2] / [di-4:2, di-4:0, Chol]. Box length (black line) and size of the disordered domain (top leaflet = black squares; bottom leaflet = gray circles).

Figure 4-2 shows the core results for our questions regarding compositional asymmetry. In this initial analysis, we restrict our attention to the simulations with di-4:0 saturated lipid, reserving analysis of the longer-chain lipids for the next section. The first 3 columns of Figure 4-2 show the densities of the various lipid components (di-4:2, di-4:0 and cholesterol) in the plane of each leaflet. As expected, in the compositionally symmetric control [di-4:2]/[di-4:2] bilayer, the lipid is evenly distributed throughout each leaflet. In each of the ternary leaflets, including both leaflets of the symmetric [di-4:2, di-4:0, Chol]/[di-4:2, di-4:0, Chol] bilayer and the bottom leaflet of the asymmetric [di-4:2]/[di-4:2, di-4:0, Chol] bilayer, the di-4:2 phase separates from the di-4:0 and cholesterol, as was previously indicated in Figure 4-1. In the symmetric bilayer, the L_o domains (consisting of di-4:0 and cholesterol) in the two leaflets overlay, indicating that

they are in register (phase symmetric), as has been previously reported for a similar system [195].

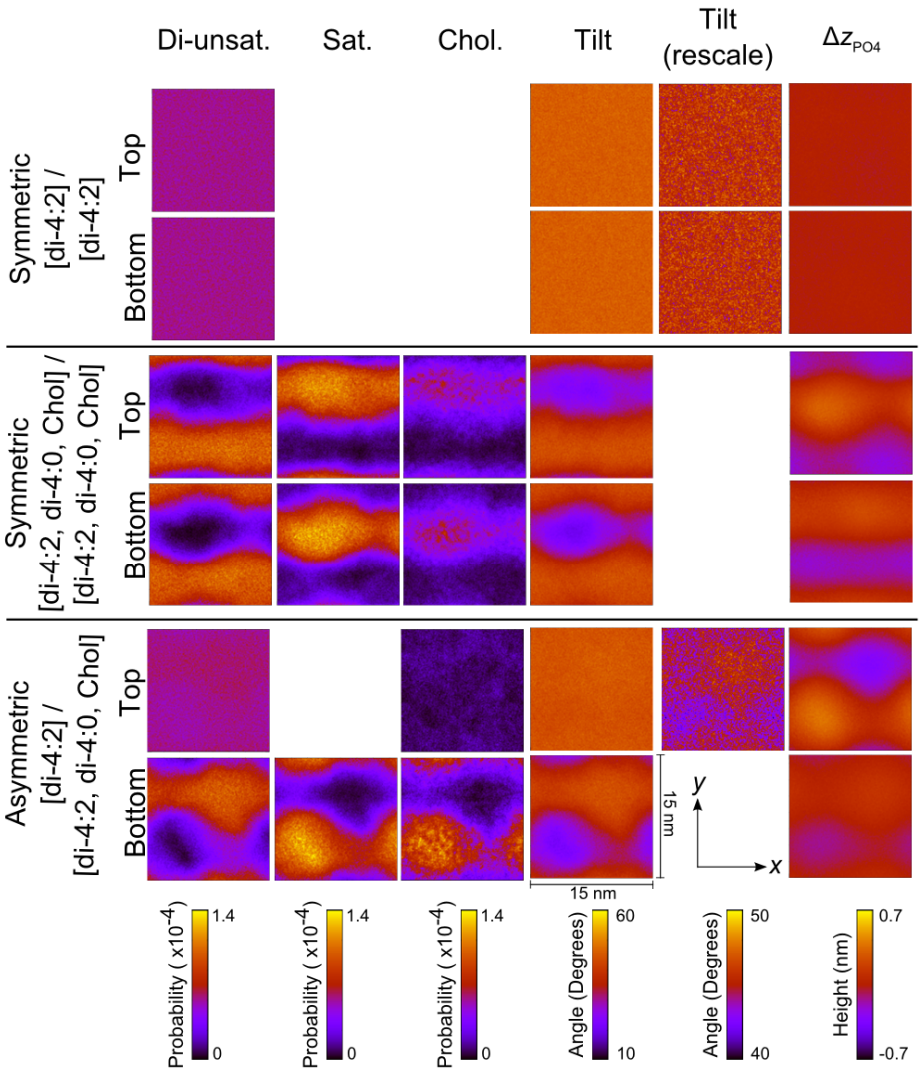

Figure 4-2 Lateral Structure in Symmetric and Asymmetric Bilayers - The effect of phase asymmetry on per-leaflet component distributions (di-unsaturated, saturated, and cholesterol), lipid tilt, and surface curvature (Δz_{PO4}) for the [di-4:2] / [di-4:2], [di-4:2, di-4:0, Chol] / [di-4:2, di-4:0, Chol], and [di-4:2] / [di-4:2, di-4:0, Chol] bilayers. Periodic images have been included so that each panel is 15 x 15 nm.

The third column of Figure 4-2 demonstrates the lateral localization of cholesterol into regions that overlap neatly with the di-4:0 distributions. Because cholesterol is known to flip-flop rapidly between leaflets on the time-scale of the

experiments we are modeling [41, 142], its equilibrium distribution should be independent of the starting configuration. As expected, in the symmetric bilayer cholesterol distributes evenly between the two leaflets as indicated by the same intensity in the cholesterol panels. However, in the asymmetric bilayer ~15% of the cholesterol redistributes to the top (di-4:2) leaflet. The cholesterol distributions converged within the first 200 ns of each simulation, remaining approximately unchanged throughout the remainder of the simulations, despite the fact that individual cholesterol molecules continued to flip-flop between the leaflets throughout. The small amount of cholesterol that ends up in the top (di-4:2) leaflet of the asymmetric bilayer (~10 cholesterol molecules) may itself have an internal effect on that leaflet's structure that is independent of the effect of compositional asymmetry. In order to address any potential effects of this, we have run a series of control simulations containing symmetric distributions of di-4:2 and increasing amounts of cholesterol.

The fourth and fifth columns of Figure 4-2 begin to address the question of whether the L_o domains in the bottom leaflet of the compositionally asymmetric simulations alter the properties, or even induce a phase transition, in the single-component, top leaflet. Assigning a phase based upon the dynamic and structural properties of lipids in a simulated bilayer is non-trivial. Our efforts to do so for the top leaflet of the asymmetric bilayers are based upon di-4:2 lipid tilt and the corresponding average lipid chain order parameter, rotational autocorrelation and diffusion, each of which is quantitatively different in the L_o and L_d phases (Table 4-2). We define lipid tilt by the angle made by the vector connecting the first and last beads of the lipid chain and the global bilayer normal. As reported in Table 4-2, in the [di-4:2]/[di-4:2] bilayer the average lipid tilt is 45.7°. In the symmetric phase separated bilayer ([di-4:2, di-4:0, Chol]/[di-4:2, di-4:0, Chol]), the bilayer averaged di-4:2 lipid tilt is reduced by 2.2°. This intraleaflet effect has been previously attributed to the fact that as unsaturated lipids enter, or neighbor, an ordered domain they adopt a more ordered state [195, 236].

Bilayer	Mean Tilt° (degrees)	Approximate Rotation Decay Time (ns)	Diffusion Coefficient (10^{-7} cm^2/s)
	di-4:2 lipids from the top leaflet		
Single Component [di-4:2] / [di-4:2]	45.8 ± 0.01	4.22 ± 0.003	2.07 ± 0.02
Symmetric [di-4:2, di-4:0, Chol] / [di-4:2, di-4:0, Chol]	43.8 ± 0.13	6.50 ± 0.02	0.74 ± 0.01
Symmetric [di-4:2, di-5:0, Chol] / [di-4:2, di-5:0, Chol]	43.3 ± 0.43	6.63 ± 0.12	0.79 ± 0.06
Symmetric [di-4:2, di-6:0, Chol] / [di-4:2, di-6:0, Chol]	42.4 ± 0.06	6.42 ± 0.11	0.68 ± 0.03
Asymmetric [di-4:2] / [di-4:2, di-4:0, Chol]	44.4 ± 0.05	4.71 ± 0.01	1.94 ± 0.05
Asymmetric [di-4:2] / [di-4:2, di-5:0, Chol]	44.9 ± 0.03	4.62 ± 0.01	1.84 ± 0.11
Asymmetric [di-4:2] / [di-4:2, di-6:0, Chol]	45.0 ± 0.05	4.66 ± 0.02	1.89 ± 0.07
	di-4:0 lipids from the top leaflet		
Symmetric [di-4:2, di-4:0, Chol] / [di-4:2, di-4:0, Chol]	22.6 ± 0.24	35.80 ± 1.80	0.39 ± 0.05
	di-5:0 lipids from the top leaflet		
Symmetric [di-4:2, di-5:0, Chol] / [di-4:2, di-5:0, Chol]	25.2 ± 0.30	54.79 ± 2.41	0.32 ± 0.01
	di-6:0 lipids from the top leaflet		
Symmetric [di-4:2, di-6:0, Chol] / [di-4:2, di-6:0, Chol]	25.1 ± 0.19	78.13 ± 2.00	0.18 ± 0.01

Table 4-2 Asymmetric Structural Effects- Lipid tilt, rotational autocorrelation, and lateral diffusion.

The effect of compositional asymmetry on di-4:2 lipid tilt in the entirety of the top leaflet of the [di-4:2]/[di-4:2, di-4:0, Chol] bilayer—an interleaflet effect—is only slightly less than the intraleaflet effect, where the average di-4:2 lipid tilt is reduced by 1.4° relative to the [di-4:2]/[di-4:2] bilayer. However, the experimental findings suggest that the focus should be on the region directly opposing the L_o domain. In the fifth column of Figure 4-2, we have readjusted the color scale in order to highlight the effect of tilt in that region alone, where the calculated tilt angles are reduced by as much as 2.2° in the region directly opposite the L_o domain, relative to the [di-4:2]/[di-4:2] bilayer.

Based on the set of cholesterol control simulations, we are able to attribute this reduction in tilt primarily to the effect of phase asymmetry, as the presence of small amounts cholesterol in that leaflet itself causes a reduction in tilt of <1°.

In Figure 4-3 we further describe the interleaflet ordering effect as quantified through the lipid chain order parameter, which has been used previously to describe the behavior of saturated and unsaturated lipids in both L_o and L_d domains [195]. This order parameter, shown in two-dimensions in Figure 4-3A, describes the alignment of each bond vector with the bilayer normal axis, with larger values indicating a more aligned, and more ordered state (Eq 4-1). In simulations of a related, compositionally symmetric ternary mixture, the di-4:2 order parameter was found to increase by ~30% when the lipid is in the L_o domain rather than its more probable location (i.e. in the L_d domain) [195]. Likewise, the di-4:0 order parameter was found to decrease by ~25% when in the L_d domain. From our simulations, we consider the value of 0.21 obtained from the single component [di-4:2]/[di-4:2] bilayer as a baseline for evaluating the magnitude of changes in ordering. Within the L_o domain of the bottom leaflet of the [di-4:2]/[di-4:2, di-4:0, Chol] bilayer, the di-4:2 order parameter increases in magnitude by as much as ~33% (to 0.28). In the opposite leaflet, in particular directly across from the center of the L_o domain, the interleaflet effect increases the di-4:2 order by as much as ~10% (to 0.23). The magnitude of this interleaflet effect is non-negligible, though perhaps less than expected if that region of the leaflet had been induced to have full L_o-character. As evident in Figure 4-3B, the magnitude of the interleaflet ordering effects are greatest at the domain centers, though there are still substantial effects observed at the domain peripheries. The effect extends out radially by ~4nm from the center of the region directly opposite the L_o domain, corresponding to an area of ~50nm2 (or that of ~70 lipids). Thus the interleaflet effect is felt in a region of the top leaflet of ~55% the total extent of the domain. There is also a weaker disordering effect in the region of the top leaflet that is opposite the L_d domain in the bottom, ternary leaflet, which will be described in more detail below. Also included in the figure is the di-4:2 order parameter from the cholesterol control simulation which, as with tilt, confirms that the interleaflet effect on lipid order is not due solely to the presence of the small number of cholesterols which

flipped into the leaflet. We have also calculated the effects of the compositional asymmetry on lipid rotational dynamics (by way of a rotational autocorrelation function) where we find an effect on the same order as the tilt and order parameter (~10%, see Table 4-2). On the other hand, we find little effect of asymmetry on lipid diffusion (Table 4-2).

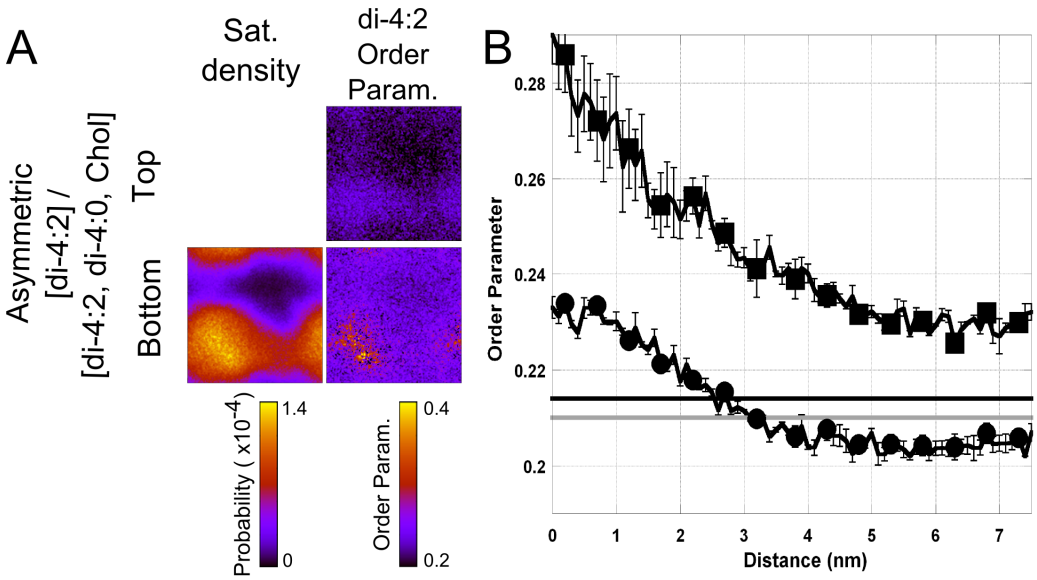

Figure 4-3 Interleaflet Ordering Effect - The segmental order parameter of di-4:2 in the [di-4:2] / [di-4:2, di-4:0, Chol] bilayer in the *xy* plane (A) and averaged in 1-dimension with the L_o domain center at *x*=0 (B). The asymmetric bilayer shows an intraleaflet effect in the bottom leaflet (squares) and an interleaflet effect in the top leaflet (circles). Di-4:2 single component (gray) and +20 cholesterols (black) are provided for comparison.

4.2.2 L_o/L_d domain-height mismatch

Our simulations comparing compositionally symmetric, phase separated bilayers where we varied the length of the saturated lipid reveal how a mismatch in L_o/L_d domain height, within a leaflet, impacts the communication between leaflets. Figure 4-4 presents the lateral distributions from these simulations (the di-4:0 data is the same as presented in Figure 4-2). Whereas in the short-chain, symmetric [di-4:2, di-4:0, Chol]/[di-4:2, di-4:0, Chol] bilayer the domains are in register, domains in the symmetric bilayers containing longer-chained saturated lipids ([di-4:2, di-5:0, Chol]/[di-4:2, di-5:0, Chol] and [di-4:2, di-6:0, Chol]/[di-4:2, di-6:0, Chol]) adopt an anti-registered, phase asymmetric

configuration. Figure 4-5 shows representative snapshots and highlights the near-perfect anti-registration of domains in the two leaflets. Also apparent in Figure 4-4, increasing the chain-length of the saturated lipid changes the domain morphology. First, there is a change in domain shape from rounder to straighter stripes, which reduces the contact area between the two domains. Second, the intensity of the profiles in the domains increases as the constituents become more fully segregated into their respective domains. Both of these observations, reduced domain perimeter and increased cohesiveness, indicate that the line tension at the L_o/L_d phase boundary is increased by the height-mismatch.

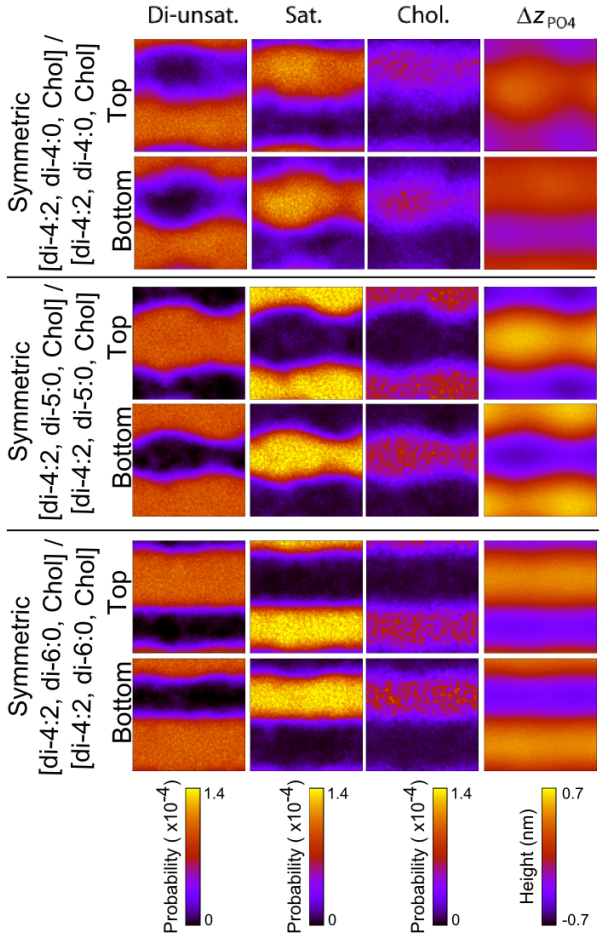

Figure 4-4 Registration and Anti-Registration - The effect of height mismatch on per-leaflet component distributions (di-unsaturated, saturated, and cholesterol) and surface curvature for the [di-4:2, di-4:0, Chol] / [di-4:2, di-4:0, Chol], [di-4:2, di-5:0, Chol] / [di-4:2, di-5:0, Chol], and [di-4:2, di-6:0, Chol] / [di-4:2, di-6:0, Chol] bilayers.

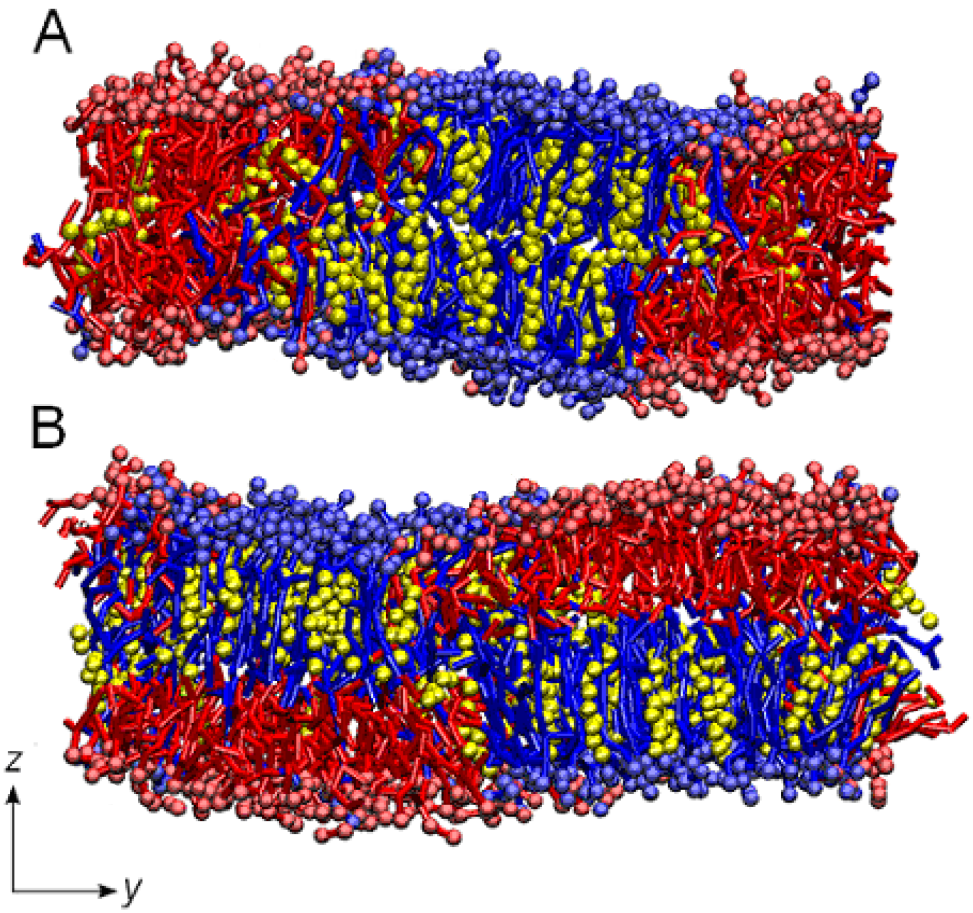

Figure 4-5 Registration and Anti-Registration Snapshots - Snapshots illustrating (A) domain registration in the [di-4:2, di-4:0, Chol] / [di-4:2, di-4:0, Chol] bilayer and (B) anti-registration in the [di-4:2, di-5:0, Chol] / [di-4:2, di-5:0, Chol] (2:2:1) bilayer. Color Scheme: Saturated lipids – blue, di-unsaturated lipids – red, cholesterol – yellow. Water has been removed for clarity.

In Table 4-2 we present the results for tilt, rotational autocorrelation and diffusion for these L_o domains containing the longer-chained saturated lipids. Increasing the length from 4:0 to 5:0 increases the saturated lipid tilt by ~10%, though further increasing to 6:0 has little effect. Increased chain-length also decreases the rotational freedom and diffusion of the saturated lipids. Importantly, the magnitudes of each of these averaged lipid properties is still within a range characteristic of the L_o phase, rather than the solid phase [140]. In these symmetric, longer-chained anti-registered bilayers, the di-4:2 lipid is slightly more ordered than in the symmetric bilayer containing the shorter-chained di-4:0.

As Table 4-2 shows, there is an increased effect on the lipid tilt (an additional decrease of ~1°), lateral diffusion (~10-20%), along with a small effect on rotational dynamics.

Anti-registration of domains across the bilayer is expected to reduce the energetic penalty associated with hydrophobic exposure of the L_o domain lipids in the case of domain-height mismatch, as has been predicted by theory [208]. However, the near-perfect anti-registration observed in Figure 4-4 and Figure 4-5 for the symmetric, long-chained bilayers is only possible because the lateral areas of the two domains are roughly equal at the 2:2:1 mole ratio. It is tantalizing to try to understand the balance of forces that appears to favor an L_o/L_d interface at the bilayer center over the penalty associated with domain-height mismatch in these longer-chain bilayers. To do so, we simulated an additional set of compositionally symmetric [di-4:2, di-5:0, Chol]/[di-4:2, di-5:0, Chol] bilayers where we altered the lipid molar ratios (and hence domain area ratios) in order to see what happens if we force regions of registration. The top two rows of Figure 4-6 present the results from the 2:2:1 mixture showing the near perfect anti-registered configuration (same data as in Figure 4-4). The middle two rows present a 1:2:1 mixture which we built expecting twice as much L_o/L_o (registration) as L_d/L_o (anti-registration) overlay between the leaflets. Figure 4-6 shows that, unlike the 2:2:1 mixture, there are small regions of L_o/L_o overlap, most clearly observed in the corners of the saturated lipid density panels. It appears, however, that despite the proportional doubling of the L_o domain components, L_o/L_o overlap is largely avoided. Instead of overlaying, the data suggest that the domains become more diffuse via changes in the lateral packing within each leaflet (compare intensities in the 2:2:1 and 1:2:1 mixtures in Figure 4-6). Additionally, and again in contrast to the 2:2:1 bilayer, there are regions with increased mixing, even regions that appear entirely mixed (seen as hazy purple in the figure, most notably at the domain peripheries).

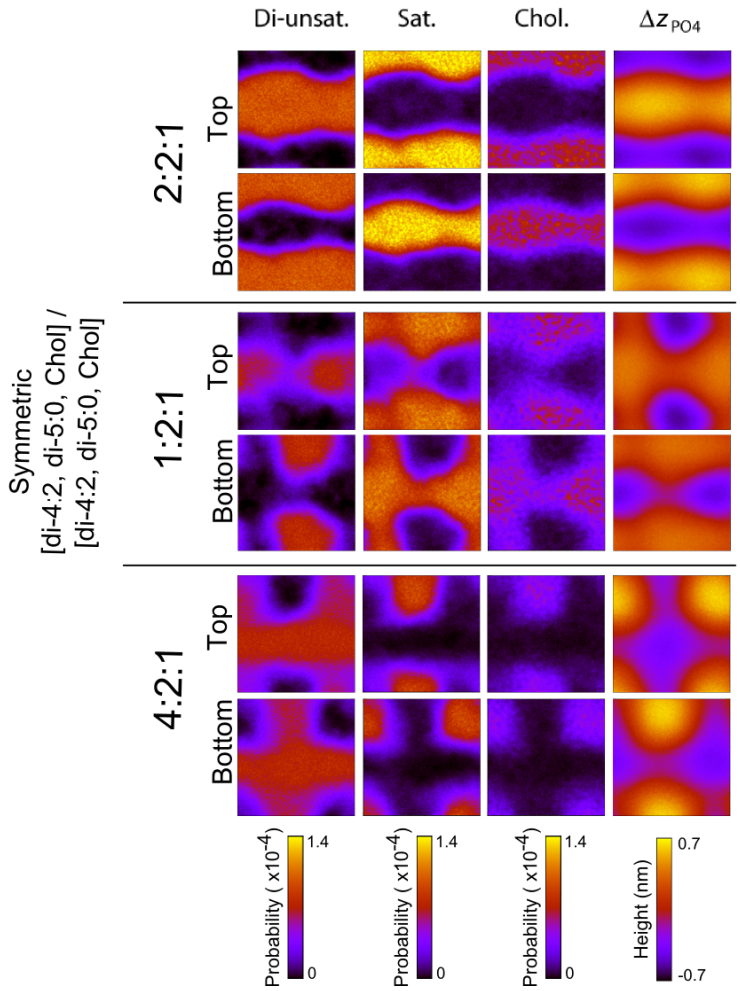

Figure 4-6 Anti-Registration and Altered Ratios - The effect of molar ratios on compositionally symmetric [di-4:2, di-5:0, Chol] / [di-4:2, di-5:0, Chol] bilayers. The near perfectly anti-registered 2:2:1 bilayer is the same as presented above, while the bilayers with different ratios of L_o:L_d show different extents of registration.

The lowest two rows of Figure 4-6 present the results of a 4:2:1 mixture, where we had intended to force a substantial degree of L_d/L_d overlap, which in this case is indeed what we observed. The contrast in the extent of L_d/L_d overlap here, as compared to the lack of L_o/L_o overlap at the 1:2:1 ratio, raises an intriguing question regarding the relative energetic penalties of domain-height mismatch and lipid-mixing, namely how the relative compressibility moduli of the two domain-types (greater in the L_o case) dictate the likelihood of domain registration.

Increasing the saturated lipid chain-length also has an effect on the compositionally asymmetric bilayers. Figure 4-7 presents results for three simulations of asymmetric bilayers containing a top leaflet of di-4:2, and bottom leaflets containing 2:2:1 ternary mixtures where we have varied the chain-length of the saturated lipid. As in Figure 4-4, increased chain-length causes the domains in the bottom leaflet to become denser and change from rounded to striped. As in the asymmetric bilayer containing di-4:0, there is an interleaflet ordering effect, observed as a reduction in tilt in the region opposite the L_o domains. However, there is also a disordering effect: increased chain-length increases the population of di-4:2 lipids in the top leaflet with higher tilts (hotter colors), in particular in regions of the top leaflet that are directly opposite the L_d phase. This may be why there is a slight increase in average tilt values compared to the di-4:0 case (Table 4-2). There was weak evidence of this type of disordering across from L_d domains in the asymmetric [di-4:2]/[di-4:2; di-4:0; Chol] bilayer as well, seen as a decrease in order parameter (Figure 4-3B, distances > 5nm), though in that case the effect was small compared to the ordering opposite the L_o domain.

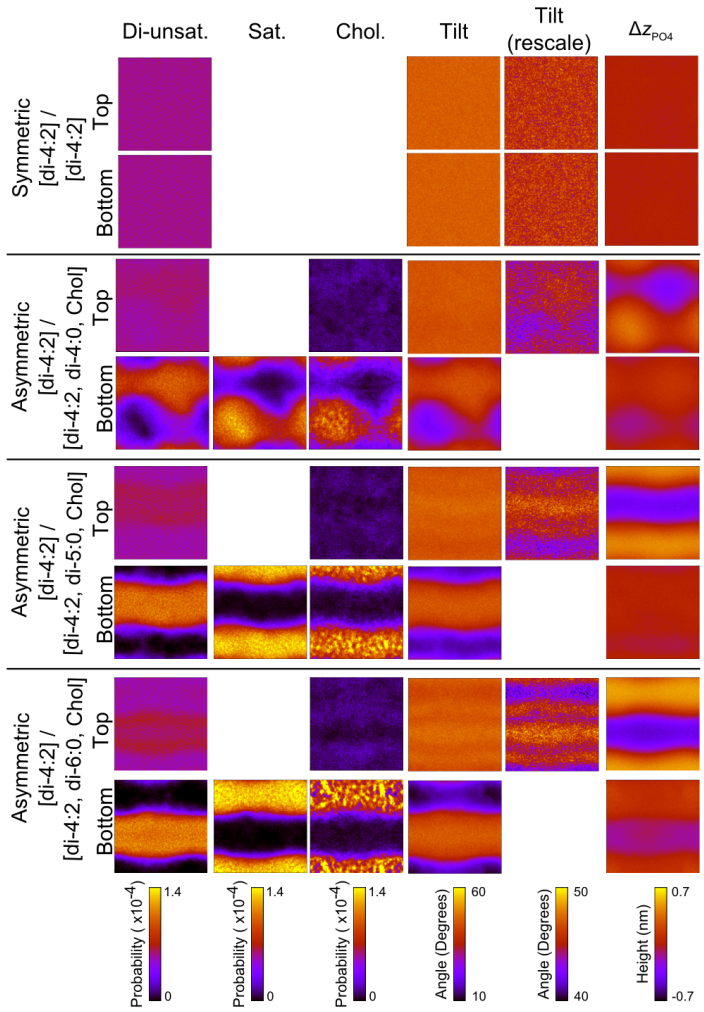

Figure 4-7 Lipid Chain Length and Asymmetry - The coupled effect of asymmetry and chain length on per-leaflet component distributions (di-unsaturated, saturated, and cholesterol), lipid tilt, and surface curvature for the [di-4:2] / [di-4:2], [di-4:2] / [di-4:2, di-4:0, Chol], [di-4:2] / [di-4:2, di-5:0, Chol], and [di-4:2] / [di-4:2, di-6:0, Chol] bilayers.

Figure 4-8 more fully describes this interleaflet ordering effect in the bilayers containing long-chain lipids, with comparison to the short-chain case. Figure 4-8A gives the average order parameter of di-4:2 lipids in the top leaflets of the asymmetric bilayers as a function of distance from the position within the leaflet that is directly opposite the center of the L_o domain in the opposing, phase separated leaflet. As was the case in the [di-4:2]/[di-4:2; di-4:0; Chol] bilayer, and consistent with the tilt data, the ordering effect is greatest in the region directly opposing the center of the L_o domain. The maximal

degree of ordering is increased with chain-length, reaching an ~12% increase over control levels, but the ordering falls off much more quickly, perhaps a consequence of the more highly segregated/denser L_o domains (cf Figure 4-7). Again consistent with the tilt data, in the regions of the top leaflet directly opposite an L_d domain, there is a striking disordering effect (decrease in order relative to control of as much as, remarkably, ~12%, nearly the exact magnitude of the ordering effect seen opposite the L_o domain).

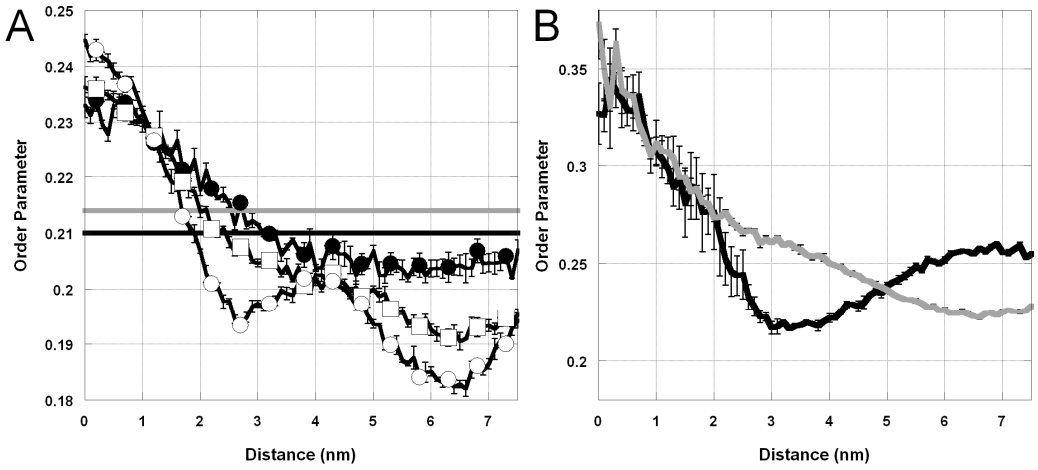

Figure 4-8 Chain Length and Ordering Effects - A) The di-4:2 order parameter in the top leaflets of [di-4:2] / [di-4:2, di-4:0, Chol] (black circle), [di-4:2] / [di-4:2, di-5:0, Chol] (open squares) and [di-4:2] / [di-4:2, di-6:0, Chol] (open circles), as well as the control simulations [di-4:2] / [di-4:2] (black) and [di-4:2, 10 Chol] / [di-4:2, 10 Chol] (gray). B) The di-4:2 order parameter in the top leaflet of [di-4:2, di-5:0, Chol] / [di-4:2, di-5:0, Chol] (black) and bottom leaflet of [di-4:2] / [di-4:2, di-5:0, Chol] (gray).

Figure 4-8B confirms that, as expected, in the long-chain, compositionally symmetric anti-registered bilayers, there is both an inter- and intraleaflet ordering effect (refer back to Figure 4-4 for corresponding density profiles). The figure presents the order parameter data for the [di-4:2, di-6:0, Chol]/[di-4:2, di-6:0, Chol] bilayer, though similar trends are found in the di-5:0 containing bilayer as well. In this case, the appropriate control for distinguishing the inter- from intraleaflet effects is the order parameter for the di-4:2 lipid in the bottom leaflet of the asymmetric [di-4:2]/[di-4:2, di-6:0, Chol] bilayer, in which case there is an intraleaflet effect on the lipid order (due to the ordering imposed by the L_o domain within the bottom leaflet), but no interleaflet effect (the opposing leaflet contains only di-4:2). In the plot, the L_o domain from both

simulations is centered at ~6.5nm. In the control, the di-4:2 is highly ordered (maximum of ~0.45) in the L_o domain, which is also the case in the symmetric, anti-registered bilayer. Outside of the L_o domain, the di-4:2 order parameter drops off sharply, though in quite different ways in the two different cases. The profile is as expected in the control case, where the intraleaflet effect is gradually, and fully screened as the lipid moves further from the domain (in the plot distances approaching zero), reaching a minimum of ~0.22 which is roughly the value of di-4:2 in the single-component L_d bilayer (Figure 4-8A). In the anti-registered, symmetric bilayer, outside the L_o domain the di-4:2 lipid experiences both this diminishing intraleaflet effect as well as the interleaflet effect due to the opposing, anti-registered L_o domain. The profile drops off much more sharply in this case (to a minimum of again ~0.22 at a distance of ~3.5nm). This particular feature of the order parameter profile is quite surprising, but in the next section may be explained by a correlation between lipid order and local bilayer curvature. Finally, far from the L_o domain, where the intraleaflet effect is no longer felt, the interleaflet effect takes over (present here because of the anti-registered configuration), and the di-4:2 order increases to ~0.26. This is very similar to the extent of ordering that we see in the L_d domain opposite an L_o domain in the single-component leaflet of the asymmetric bilayer (Figure 4-8A).

4.2.3 Induction of curvature in asymmetric bilayers

The last columns of **Figure 4-2**, **Figure 4-4**, **Figure 4-6**, and **Figure 4-7** present what are perhaps our most novel findings, namely the effects of compositional asymmetry and domain-height mismatch on the curvature of individual leaflet surfaces. To measure curvature, for each leaflet we defined the average phosphate height, and then calculated a Δz_{PO4} for each lipid's phosphate bead relative to that average, binning the data in the *xy*-plane. Positive values (hot colors) indicate outward projections from the bilayer center (for either leaflet). In the [di-4:2]/[di-4:2] bilayer, both leaflets are uniformly flat, as indicated by the value of zero throughout the surface. It is important to note that flatness does not reflect an absence of the normal dynamic motions in the *z*-axis (undulations) [237], but is rather a consequence of the time average of those undulations being zero. The magnitude of these fluctuations is described by the root mean square

deviation for the distance from each phosphate group to an average flat surface, which for each leaflet of the [di-4:2]/[di-4:2] bilayer is ~0.3nm. That is, at any individual timepoint there are thermal fluctuations of this magnitude away from a flat surface, however in the [di-4:2]/[di-4:2] case there is no time-averaged surface curvature.

Quite in contrast, all of the simulated bilayers containing at least one phase separated leaflet are curved. Figure 4-9 recasts the two-dimensional ΔzPO4 data presented earlier in one-dimension, presenting a clarifying view of how curvature is communicated from one leaflet to the other in these complex mixtures. As already noted, there is no time-averaged curvature in the single component [di-4:2]/[di-4:2] bilayer (Figure 4-9A). The calculation of these surfaces is based upon the center of each coarse-grained bead, so that despite the apparent gap at the center of the bilayer (between the terminal methyl surfaces from each leaflet) there is in fact no empty space. Figure 4-9B shows that in the symmetric [di-4:2, di-4:0, Chol]/[di-4:2, di-4:0, Chol] bilayer, the L_o domains extend further outwards than the L_d domains in both leaflets. That this is the case suggests a degree of domain-height mismatch even in the case of L_o domains composed of the shorter-chain saturated lipids. Figure 4-9C shows that in the compositionally symmetric [di-4:2, di-6:0, Chol]/[di-4:2, di-6:0, Chol] bilayer, increasing the domain-height mismatch increases surface curvature. The curvature profile in the compositionally symmetric di-5:0 bilayer is similar. In both of the anti-registered bilayers, the L_o domains curves inwards, and appear to push out the L_d domains (opposite of what is seen in the registered [di-4:2, di-4:0, Chol]/[di-4:2, di-4:0, Chol] bilayer). In all of the phase separated, symmetric bilayers the curvature is apparent at both the headgroup and terminal methyl surfaces. In the di-5:0 and di-6:0 cases, the headgroup surface is quite curved, but the methyl surfaces are significantly more so, allowing for a striking ‘inter-locking’ of these anti-registered domains at the bilayer center.

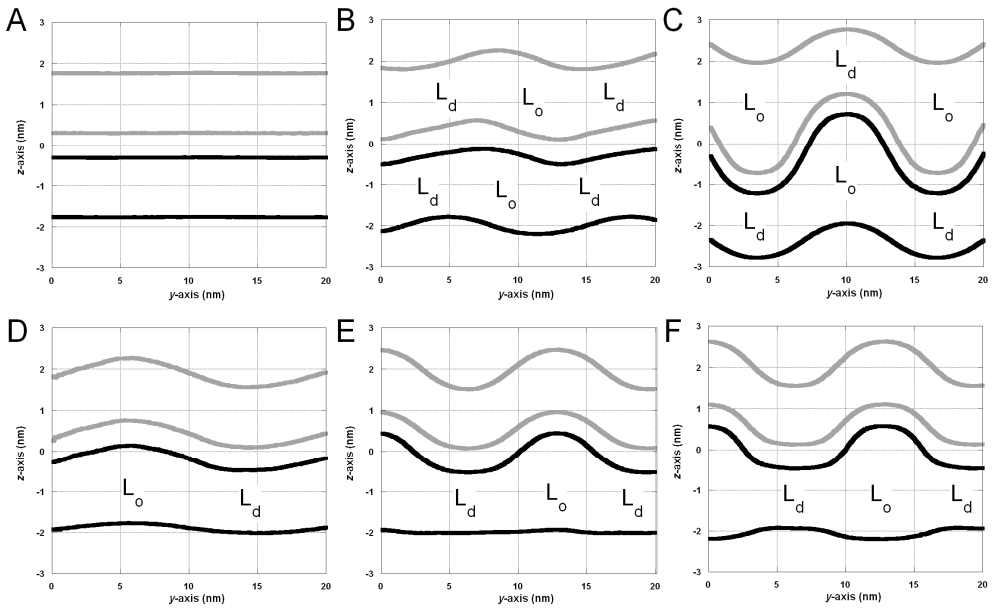

Figure 4-9 Bilayer Curvature - The height of the surfaces composed either of the top leaflet phosphate or terminal tail groups (gray) and bottom leaflet phosphate or terminal tail groups (black) for both saturated and di-unsaturated lipids. (A) [di-4:2] / [di-4:2] (B) [di-4:2, di-4:0, Chol] / [di-4:2, di-4:0, Chol] (C) [di-4:2, di-6:0, Chol] / [di-4:2, di-6:0, Chol] (D) [di-4:2] / [di-4:2, di-4:0, Chol] (E) [di-4:2] / [di-4:2, di-5:0, Chol] (F) [di-4:2] / [di-4:2, di-6:0, Chol]. Note that the x- and y-axes have a different relative scale in order to emphasize the curvature.

This 'inter-locking' effect reflects a drive to avoid domain height-mismatch (and resulting curvature strain). Registration of di-5:0 or di-6:0 L_o domains would lead to much sharper transitions between height-mismatched domains and is thus not seen (Figure 4-4 and Figure 4-5). We imagine two mechanisms that could resolve height-mismatch: domain anti-registration or domain registration with a large degree of mixing at the domain boundaries. We observe the former, suggesting that the mixing penalty is larger than the penalty due to anti-registration (which we will discuss below). However, in the 1:2:1 and 4:2:1 bilayers (Figure 4-6), the domains are unable to "perfectly" anti-register, and thus there is a height mismatch between neighboring regions of phase symmetry (either L_o/L_o or L_d/L_d) and phase asymmetry (L_o/L_d). In these cases we do observe an increase in mixing at the domain boundaries. Though mixing is energetically unfavorable, it is apparent that in this case, the penalty is less than the penalty due to extreme curvature.

The corresponding curvature effects in the asymmetric bilayers, shown in Figure 4-9D-F, are quite remarkable. First, the surfaces of the top, single component leaflets are not flat (compare with the [di-4:2]/[di-4:2] in Figure 4-9A); rather they project outwards in the region opposing the L_o domain (that is, the L_o domain in the bottom leaflet induces a local positive curvature in the top leaflet), and it projects inwards in the region opposite the L_d domain (the L_d domain in the bottom leaflet induces a local negative curvature in the top leaflet). Second, the bottom leaflets in these asymmetric bilayers are relatively flat compared to the more curved surfaces in the corresponding symmetric bilayers (Figure 4-9B and Figure 4-9C). As the saturated lipid chain-length is increased, the L_o/L_d thickness difference manifests at the terminal methyl surfaces. This curvature is matched by the top leaflet, both in the bilayer center and in the headgroups. As the ordered domain gets thicker, the curvature on the top leaflet gets larger. Thus it appears that the bottom, phase separated leaflets resist curvature in their headgroups, and that the major impact of domain-height mismatch in the bottom leaflet manifest in the top, single-component leaflet as an induced leaflet curvature.

As described in the section I4.1-Methods, we have been exceptionally careful in minimizing any potential leaflet-leaflet area mismatch in our simulated bilayers through our approach to system construction. To further ensure that these curvature phenomena are not due to a buckling effect of area mismatch, we have run a control simulation in which we dramatically altered the area of one of the two leaflets (by removing a number of lipids). The result of that control is well-substantiated evidence that the curvature effects in these simulated bilayers are a real consequence of differences between the L_o and L_d phases, namely their respective thicknesses and resistance to bending in the individual leaflets, and not an artifact of area mismatch.

It is quite illuminating to compare the curvature profiles in Figure 4-9 to the order parameter data from Figure 4-8. In doing so, a clear correlation emerges between surface curvature in the top, single component leaflet and the induced interleaflet ordering effect. For each of the three asymmetric bilayers, in regions opposite L_o domains the top leaflet has positive curvature and the di-4:2 lipids in that region have an increased order parameter (as well as decreased lipid tilt). Positive curvature suggests increased

compression of the chains within the leaflet, offering a likely explanation for their increased order [238]. Conversely, in the regions of the top leaflet that are opposite an L_d domain the leaflet has a negative curvature (decreased chain compression) and the di-4:2 lipids in that region have a decreased order parameter. As was indicated in Figure 4-8, this effect is increased in the longer chained lipids: larger degrees of surface curvature correlate with larger effects on chain order. The correlation between curvature and order also offers a potential explanation of the data in Figure 4-8B for the anti-registered bilayers, though this is complicated by the presence of an L_o domain in both leaflets. The di-4:2 order just outside the L_o domain was reduced relative to the control, and as Figure 4-9C shows the leaflets in those regions have negative curvature. Quite in contrast, in the control case (Figure 4-9F) those regions are nearly flat.

4.2.4 Cholesterol position and interdigitation at the bilayer center

The inter-locking of domains at the center of the asymmetric bilayers (Figure 4-9) is somewhat reminiscent of ideas put forth by Sankaram and Thompson in early NMR experiments on the distribution of phospholipids and cholesterol in L_o- and L_d-only bilayers [39, 227]. In those studies, the focus was on the leaflet-leaflet interface and the role of inter-locking of the constituent molecules between the two leaflets. Our findings thus far have focused on the inter-locking of domains, and here we present a more microscopic view of organization of the constituent molecules. We have probed how the interleaflet interactions described above influence the distribution of molecules in the z-dimension (normal to the bilayer). We were specifically interested in whether the lipids and cholesterol molecules inter-lock (or interdigitate) at the bilayer center.

In Figure 4-10 we plot the one-dimensional representations of the bilayers with the average location of the cholesterol headgroups and terminal tail groups now superimposed on the lipid backbone and terminal methyl positions. It is important to remember that the positions of the lines and points in these figures under-estimate the extent of the molecular distributions in the z-dimension, because they are calculated as the center of the coarse-grained beads, most of which have a radius of ~0.47 nm [133]. Additionally, the data do not reflect the gradient of cholesterol concentration associated with the domains, thus in the L_d domains the average cholesterol positions are taken over

many fewer molecules. In each of the simulations, the time-averaged position of the cholesterol hydroxyl is slightly beneath the lipid backbone group, in agreement with the NMR experiments and atomistic simulations which suggest a hydrogen-bond between the two [36, 39]. In the [di-4:2]/[di-4:2] bilayer (Figure 4-10A), the center of the cholesterol tail terminal beads meet at the center, which shows a modest degree of interdigitation of cholesterols.

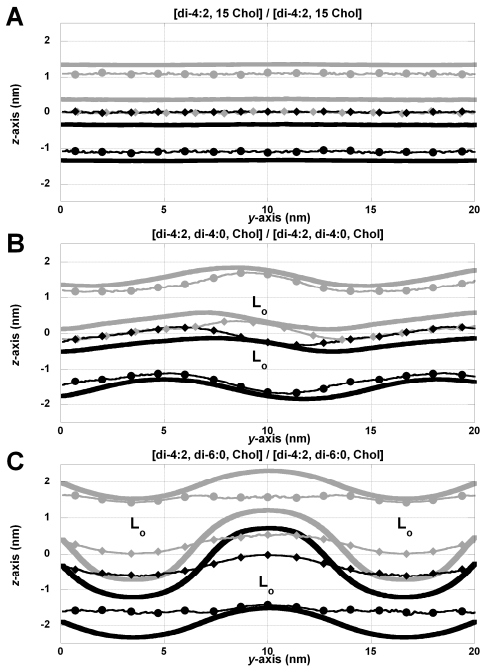

Figure 4-10 Cholesterol Position - Positions of lipid backbone (solid), terminal methyl (solid), cholesterol hydroxyl (circle), and cholesterol tail (diamonds) for the top (gray) and bottom (black) leaflets of selected simulations.

This position for the cholesterols is maintained in the L_d regions of the [di-4:2, di-4:0, Chol]/[di-4:2, di-4:0, Chol] bilayer (Figure 4-10B). However, in the L_o regions of the same bilayer cholesterol behaves differently. In particular, the cholesterol hydroxyl is closer to the lipid backbone and the cholesterol tails no longer extend to the bilayer center, but instead reach only as far as the lipid terminal methyls. Again, this region of the figure should not be interpreted as indicating empty space at the bilayer center (given that the beads occupy considerable volume beyond their centers). Nevertheless, the data does appear to indicate a slightly diminished molecular density at the L_o/L_o interface that is not present at the L_d/L_d interface. Whether this effect is increased with lipid chain-

length is hard to say because of the shift to the anti-registered configuration. However, in the longer-chain data (Figure 4-10C) the cholesterol tails are even further from the bilayer centers in the L_o regions, a consequence of the strong attraction between the hydroxyl and the lipid backbones. Quite interestingly, at the L_o/L_d interface at the bilayer center, the cholesterols in the opposing leaflet (in the L_d domain) appear to have released their stabilizing hydrogen-bonds with the lipid backbones, having sunk further into the bilayer core, with their tails extending past the bilayer center. This lost interaction between the cholesterol and the lipid backbone also occurs in the asymmetric, long-chained simulations. In each case where we have observed this loss of the hydrogen bond, it occurs in regions of leaflets that are opposite leaflets of negative curvature, though we currently have no explanation for this finding.

4.3 Discussion

We have organized our study based on two broad mechanisms through which lipid rafts could provide a platform for interleaflet communication. First, in the case of a locally symmetric lipid composition, L_o domains tend to form in the two leaflets in register, resulting in a homogeneous phase across the bilayer (phase symmetry). Conversely, in the case of domain-height mismatch, the domains are anti-registered (phase asymmetry). These anti-registered domains are then subject to the second type of interleaflet organization, which stems from locally asymmetric lipid composition. In this second case, L_o domains in one leaflet can alter the thermodynamic properties of the apposed leaflet. At one extreme, this influence can result in induction of L_o domains despite a lipid composition that would, on its own, favor the L_d phase. This mechanism has been shown in numerous experiments on model systems to depend upon on the specific lipid mixtures and experimental setups. In a less extreme case, where domain formation is not induced, there exists a phase asymmetry, which does not preclude the likelihood that the domains in the one leaflet alter properties of the other without inducing a complete phase change.

We have observed a clear difference in the molecular properties of a di-4:2 leaflet opposite a phase separated leaflet (namely chain tilt and order, rotational dynamics and curvature). However, whether this justifies re-categorizing the phase-state of the leaflet

remains unclear. Furthermore, while it is convenient to describe these bilayers as only consisting of two phases (L_d and/or L_o), an alternate, and perhaps more thermodynamically rigorous definition of a region containing phase asymmetry might be as a single, bilayer-spanning 'mixed' phase, as has been postulated based upon recent microscopy experiments [107]. Therefore, these simulations could also be considered the first to describe structural differences between the symmetric and 'mixed' phases.

Experiments on asymmetric bilayers have generally been incapable of interrogating physical properties in a single leaflet, making direct connection with simulations difficult. In the set of fluorescence experiments on asymmetric bilayers two outcomes, or three in the case of Collins et al, have been distinguished by the partitioning of dyes (as determined by visual assignment of fluorescence intensity) [95, 107-109]. On the other hand, in simulated bilayer models of L_o/L_d domain separation there is an inherent ambiguity in assigning phase in the same way as the experiments. Most simply put, we do not simulate the partitioning of a dye, though that would in theory be a tractable approach given careful parameterization of the dye chemistry. It is not clear that such a parameterization would be reliable under the coarse-grained simulation strategy, given the subtle chemistry involved, though recent attempts have been promising [156]. Instead, the assignment has typically been made simply by the densities of co-localized constituents (unsaturated lipid in the L_d domain, and saturated lipid and cholesterol in the L_o).

Thus, a vexing issue in analyzing these simulations was whether to assign a phase to the compositionally asymmetric bilayers: is the di-4:2 lipid opposite an L_o domain induced to form the L_o phase, or is it just relatively ordered L_d? In order to answer this question directly from simulations, we would need access to a direct, quantitative relationship between phase and quantifiable lipid properties (e.g. tilt and order) in asymmetric bilayers. Currently, experimental studies on asymmetric bilayers have addressed either phase *or* lipid properties, but have not drawn a clear, quantitative relationship between the two. Regarding phase, we have described in detail the experiments which used fluorescent dyes to distinguish between the phases [95, 107-109]. Regarding lipid properties, one recent example was the use of fluorescence anisotropy to

describe a decrease in the degree of rotational diffusion (and hence chain order) in the leaflet opposite an L_o domain [183]. However, this study did not attempt to characterize the phase-state of the altered leaflet.

A probe-free and quantitative experimental method for distinguishing between L_o and L_d domains has recently been established using wide-angle x-ray scattering (WAXS) [151, 239, 240]. Though this experimental technique is incapable of distinguishing structures in two leaflets, WAXS spectra from simulated bilayers might reasonably be decoupled between the two leaflets. Future simulation efforts might take advantage of that comparison point in establishing the exact phase signature of simulated domains by calculating the WAXS spectra directly from the simulations, though the adequacy of CGMD bilayer simulations to accurately capture x-ray scattering profiles in general has been questioned [143]. Alternate experimental approaches that provide the type of information we have extracted from simulations, such as chain tilt and order (perhaps deuterium NMR experiments on asymmetric bilayers, if only one leaflet could be selectively per-deuterated), would provide a more robust criterion for distinguishing between a relatively-ordered L_d phase and the L_o phase in simulations.

Our finding that long-chain saturated lipids (and the resultant domain-height mismatch) leads to domain anti-registration is consistent with a recent theory that suggested that domain registration is dictated by the balance of two tensions [208]. The first is an interleaflet tension that is predicted to exist between opposing leaflets of different phase, and is thus minimized by registration. The second competing tension is an intraleaflet one, partially caused by height mismatch between neighboring thick (L_o) and thin (L_d) domains—within a given leaflet—that can be ameliorated by anti-registration (see **Figure 4-5** and **Figure 4-9**C). Not only does a domain-height mismatch challenge the system with hydrophobic exposure of the chains of the thicker (L_o) domain, it is also likely to incur a curvature stress penalty at the domain boundaries. Our simulations of varied mole ratios (**Figure 4-6**) showed that an additional mechanism by which bilayers avoid this apparently costly penalty is through increased mixing of the saturated and unsaturated lipids at the domain boundaries. We see the transition from the registered to anti-registered configurations when the saturated lipid is increased in length from di-4:0

(which models 16-carbon chains) to di-5:0 (20-carbon chains), increasing the L_o/L_d height-mismatch by ~4 Å. It is quite compelling that this transition occurs near the chain-lengths of most biologically relevant lipids.

An additional consideration regarding the balance of these two tensions is how their relative contributions change with domain size [208]. The magnitude of the interleaflet tension (which is minimized by registration) is dependent upon the domain area, whereas the magnitude of the intraleaflet tension (which is minimized by anti-registration) is dependent upon the domain perimeter. Because a domain's area increases more quickly than its perimeter as it increases in size, all else being equal, we would expect larger domains to favor registration and smaller domains to favor anti-registration. This potentially explains why domain registration is more commonly observed in microscopy experiments than anti-registration, as these experiments are typically done using large domains (tens of microns) [92-95, 97, 107-109]. Anti-registration has been observed in simulations of very small (nm) solid domains [211, 212], and has been suggested experimentally [241, 242], including in one notable study of small (<microns) solid domains [207]. The presence of anti-registered domains at the length-scale of our simulations is difficult to detect experimentally, and given that biological ordered domains are thought to be as small as tens of nanometers [46, 200], may be a significant observation. It should be noted that we cannot rule out the possibility of finite-size effects in our simulations, though the fact that we see both registered and anti-registered domains indicates that these findings are likely not artifacts of the simulation conditions.

Finally, our findings regarding curvature have bearing on interpretation of experimental observations regarding domain formation and curvature. Experiments in model systems have demonstrated that this type of resistance to curvature is indeed greater in L_o domains than L_d domains, for example as seen in vesicle pipette aspiration [112, 243-245]. It is within this context that our curvature results are particularly compelling. Specifically, in the asymmetric bilayers, we show that the ternary leaflets are flat, but the single-component L_d leaflets are curved. That is, the L_o domains of the bottom leaflets resist curvature to a greater extent than the L_d domains in the top leaflet. This forces the top leaflets to conform to the shape of the bottom leaflet's mismatched acyl chains,

resulting in curvature in the top leaflet that likely alters the lipid order. These findings motivate our new hypothesis that induced curvature and associated changes in lipid order is at least one source of interleaflet coupling in asymmetric bilayers. Curvature has been shown to influence membrane protein behavior [121, 129, 246-249] and to be an important determinant of intra-cellular protein trafficking [121, 246, 250]. Thus, our findings suggest that curvature induced by compositional asymmetry may play an important role in membrane protein localization and function.

II Computational Modeling of a Membrane Protein

Preface

The structure and function of all proteins are determined by their environment. Section I characterized some of the structural features of membranes known to affect the behaviour of membrane proteins, including membrane thickness (Chapter 2), membrane phase (Chapters 3 and 4), lipid orientational order (section 4.2.1), and membrane curvature (section 4.2.3). In particular, the spontaneous generation of membrane curvature in phase asymmetric bilayers was a surprising and perhaps important result. In this Chapter, the role of curvature is investigated from the perspective of the membrane protein α-Synuclein. Our findings in this chapter suggest that α-Synuclein's response to curvature may be critical for understanding its currently unknown function.

This chapter is based on a published manuscript and supplemental information and figures are available through the journal [129].

5 Curvature Dynamics of α-Synuclein Familial Parkinson Disease Mutants

5.1 Introduction

The main component of fibrous inclusions known as Lewy bodies and Lewy neurites, α-synuclein (αS) plays a critical, though as yet not fully understood, role in the onset of Parkinson's disease (PD) [251]. Three point mutations of αS, namely A53T, A30P, and E46K, have been correlated with familial PD [252-254], though it is still unclear exactly how these mutations trigger the disease [255-258]. In the case of A30P, a set of recent NMR studies suggest that the proline substitution significantly increases the structural dynamics of the protein when bound to a SDS detergent micelle [259, 260]. It is widely accepted that this mutant has reduced binding affinity for membranes, although the extent is somewhat controversial [259, 261-267]. The change in membrane affinity is correlated with a decrease in the helical content of the protein, though again there is considerable debate as to the extent of this effect [259, 260, 263, 266, 268]. This result is not altogether unexpected: proline disrupts helices due to the loss of a backbone-hydrogen bond and steric hindrance between it and neighboring residues [269]. The exact effects of proline on a helix, however, can be twofoL_d: substitution can cause local unfolding (i.e. total loss of secondary structure) or kinking without loss of helicity. In the case of A30P, current experimental techniques have suggested a loss of helicity up- and down-stream of the substitution. However, it is still unclear to what extent, and where, the proline substitution forces unfolding, kinking or both [259, 260].

The other PD familial mutants behave quite differently. The threonine substitution does not disrupt αS affinity for either synthetic vesicles or cellular membranes [259, 261-263, 265-267]. Likewise, the mutation does not appear to impact the protein's secondary structure (i.e. helicity is fully conserved) [259, 260, 263, 266, 268]. The more recently discovered E46K mutation leads to tighter binding between the protein and synthetic vesicles [270], while also preserving the secondary structure [271]. How these three mutations exert such divergent affects, yet are each linked to PD remains an open question. Though the function of αS remains unknown, localization to synaptic vesicles [262, 272, 273] has led to investigation of its role in synaptic vesicle regulation [122-126]. Therefore, changes in membrane affinity or

protein structure may alter αS's functionality, and may be a significant factor in PD pathogenesis [274].

Structurally, the N-terminal domain (residues 1-99) of wt αS forms two anti-parallel amphipathic helices on the membrane surface [275, 276]. The acidic C-terminal domain (residues 100-140) does not participate in membrane binding and remains unstructured [277, 278]. Truncation of the protein beyond residue 99 has no affect on the structure nor binding properties of the N-terminal domain [259]. When bound to a SDS micelle, the two helices, connected by an unstructured loop, are unusually dynamic and highly curved (the C-terminal helix (helix-C) being nearly twice as curved as its N-terminal (helix-N) counterpart) [279]. This micelle-bound structure is not nearly as curved as the unperturbed, spherical SDS micelle, and the degree of curvature is likely of functional significance. It was speculated, though not proven, that binding of αS deforms a micelle in a uniaxial direction, forcing an ellipsoidal, rather than spherical, structure [279]. This invites a highly attractive hypothesis: protein-induced membrane-deformation may underlie αS function, in particular as regards the potential impact such deformations may have on membrane fusion and the formation of fusion intermediates.

Computational molecular dynamics (MD) simulation is an excellent tool for characterizing the structural and dynamic features of proteins. MD simulations are capable of revealing molecular-level detail inaccessible to current high-resolution experimental methods, and can therefore illuminate unresolved issues connecting a protein's structure to its biological function. Because the function of αS appears so tightly coupled to dynamic changes in its structure, MD is an ideal tool for studying this system. Indeed, four recent MD simulations of αS have provided tremendous insight into the behavior of the wt protein. In particular, simulations have: revealed a broad distribution of natively unfo$L_d$ed structures in solution; mapped specific, stabilizing contact points within those structures [280]; elucidated the behavior of wt αS on the surface of membranes, in one case calculating the energetics of membrane binding [281], in another suggesting a novel homo-oligomeric organization [282]; and described the behavior of the inter-helical turn region in multiple environments [283].

The goal of this current study has been to use MD simulation to uncover experimentally inaccessible information regarding structural and dynamic changes to αS induced by the A53T, A30P, and E46K mutations. Collectively, our simulation results confirm and expand upon the existing perceptions regarding the PD mutants. The first set of simulations starts with the recently solved, high-resolution NMR structure of wt αS bound to a SDS micelle, where great care has been taken to accurately reproduce the experimental system [279]. We find that protein binding elongates the micelle, relieving curvature stress, and suggesting a functional role for wt αS. Helical bending, in particular at the site of consecutive glycine residues, endows αS with the conformational flexibility necessary to bind to membranes with variable curvature. Simulations of the mutant forms are analyzed in terms of local and long-range changes in dynamics and structure.

Significant questions remain about directly transferring the insight derived from micelle studies to the character of αS in biological membranes. Two recent experimental studies suggest that the structure of the membrane-bound form of αS is similar to the micelle form (i.e. contains the same broken helix structural motif) [283, 284]. These experiments provide a good rationale for designing our second set of simulations, in which we have studied the dynamics of αS and the three mutants bound to a DOPS bilayer using the simulated, micelle-bound structure of wt αS as our starting configuration. We have chosen phosphatidylserine because of αS's high affinity for anionic phospholipids [276]. A comparison of our results for the highly curved micelle and the flatter bilayer patch suggests that αS likely adapts to biological membranes of intermediate curvature (e.g. synaptic vesicles) by modulating the degree of bending at specific flexible sites.

5.2 Methods

5.2.1 Micelle-Bound Simulations

The starting configuration for the αS protein was the structure as determined by high-resolution NMR (PDB index 1XQ8 [279]). For the micelle simulation a pre-equilibrated, fully hydrated micelle consisting of 100 SDS detergent molecules was positioned a few angstroms away. Initial wt simulations were run using a SDS micelle composed of 70 SDS molecules, the reported average size from experiment [275, 279].

However, despite considerable effort, we were unable to stabilize the protein on this micelle, and thus nominally increased its size. The protein was positioned with the hydrophobic surface facing the micelle so as to match their concavities, buiL$_d$ing-in an assumption regarding their relative orientations that is fully reasonable given the results of the NMR study [279]. The protein includes only the N-terminal domain, residues 1-99. Figure 5-1 gives the primary amino acid sequence for the simulated protein, and highlights the key structural segments as well as positions of the point mutants. This system was solvated in a water box consisting of ≈23,000 TIP3 water molecules, with several layers of water molecules separating the protein and micelle. The average size of the simulation cell (90 Å x 90 Å x 90 Å) was carefully determined based upon the minimum-image convention so as to avoid finite-size artifacts, and included 100 sodium cations, and additional chloride anions to neutralize the overall charge of the system. Thus, the solvated protein/micelle simulations consisted of ≈76,000 atoms. Control simulations of a solvated, detergent-free wt α-synuclein and a protein-free, solvated micelle consisted of ≈69,000 atoms and ≈74,000 atoms, respectively.

MDVFMKGLSKAKEGVVAAAEKTKQGVAEAAGKTK
EGVLYVGSKTKEGVVHGVATVAEKT*KEQVTNVGGA*
*VVTGVTAVAQKTVEGAGSIAAATGFV*KKDQ

Figure 5-1 - Amino acid sequence of membrane binding domain of αS. Only the first 99 amino acids are involved in lipid binding and were considered in these simulations. Underlined are the two helices in the lipid binding domain. The positions in the wild-type where the PD familial mutations occur are in boL$_d$. The highly hydrophobic NAC region consisting of residues 60-95 is italicized.

The micelle-bound systems were constructed and analyzed using CHARMM version 32 with the CMAP correction. Periodic boundary conditions were applied, using a constant number of atoms (N), pressure (P) and temperature (T), to form NPT ensembles. The temperature in each simulation was set to 303 K. Simulations were performed using NAMD version 2.6. A cutoff of 10 Å was used for van der Waals interactions, and particle mesh EwaL$_d$ summation was used for long-range electrostatic interactions. The time step was 2 fs, and all bonds involving hydrogen were fixed using the SHAKE algorithm. The molecules were visualized with VMD [167] and secondary

structure was calculated with the Stride algorithm [285], which assigns secondary structure from a given coordinate set based upon hydrogen bonds and torsion angles.

Because the structure of αS does not provide direct information regarding the configuration of the SDS micelle, we employed a strategy of protein restraints in order to allow the proteins to bind to, and equilibrate within, the micelle. Specifically, the systems were first energy minimized, and then simulated for 20 ns with the protein under a restraint, to prevent unfolding. During the course of these 20 ns, the micelle, which was not restrained, morphed into contact with the protein, forming two deep channels into which the two helices buried. The simulation was then run in this bound-state without restraint for 45 ns. Thus, each αS/micelle system was run for a total of 65 ns, though only the unrestrained simulation was used for analysis. The protein-free and micelle-free systems were each run for 10 ns, where in the case of the protein-free system the micelle's radius of gyration was deemed converged (data not shown), and in the micelle-free system the RMSD of the protein clearly contrasted with the stability of the micelle-bound protein.

In order to construct the A30P, A53T, and E46K mutants, the starting configuration of the system was the same as wt (i.e. the NMR structure), with only the sidechains of the appropriate residues substituted. The orientation of the substituted residue was determined by the coordinates of the wt sidechain, and additional atoms were added using the CHARMM force fieL_d parameters for bonds, angles, and dihedrals. These two simulations were setup and run using the identical conditions and strategy of restraints and dynamics described for the wt.

5.2.2 Bilayer-Bound Simulations

The bilayer-bound systems were constructed by placing the final structure of the wt micelle-bound protein in the headgroup region of a pre-equilibrated pure DOPS bilayer (containing 512 lipids and ≈17,500 waters). All mutations were made from this common point as described above. An approximate surface area was calculated for the protein (based upon a cylindrical representation of the helices), which suggested an approximate number of lipids that should be removed from the monolayer that contained the protein. Lipids in closest contact with the protein were thus removed, leaving a total

of 479 lipids along with neutralizing ions (≈81,000 total atoms). In order to minimize finite-size effects and avoid artifacts of the simulated boundary condition, we chose to use a large, fully hydrated bilayer and to simulate with a variable lateral area. We used the united atom GROMOS force fieL_d (GROMACS version 3.3.2), which allows for more efficient simulation of large lipid systems and is more frequently used for variable lateral area simulations than CHARMM. Simulations were performed under the NPT ensemble at 303 K, and employed the Parrinello-Rahman pressure and Nose-Hoover temperature coupling scheme. A cutoff of 16 Å was used for van der Waals interactions, and particle mesh EwaL_d summation was used for long-range electrostatic interactions. The time step was 2 fs, and all bonds were constrained using the LINCS algorithm. Membrane simulations were run for 50 ns after a similar minimization and constrained dynamics scheme employed for the micelle. While comparison between different force fieL_ds can be complicated, a recent exhaustive simulation study suggests that both force fieL_ds are reasonably similar in modeling protein behavior [286]. In order to confirm that our comparison of micelle and bilayer results were not overly dependent upon our force-fieL_d choice, we simulated wt αS bound to DOPS using CHARMM (using parameters from [287]) under constant area (NP_NAT ensemble) and observed remarkably consistent magnitudes of protein motion as those we report below for GROMOS.

Simulations were run on the Minnesota Supercomputer Institute's cluster of 307 IBM BladeCenter LS21 nodes and the University of Illinois' National Center for Supercomputing Application's cluster of 1450 Dell PowerEdge 1750 nodes. Approximately 200,000 total cpu hours were used.

5.3 Results

5.3.1 Bound-State Structure

Snapshots taken from the simulation of wt αS bound to a SDS micelle are shown in **Figure 5-2**. The backbones of the two helices, consisting of residues 3-37 (helix-N) and 45-92 (helix-C), are both deeply buried beneath the headgroups of the detergent. Despite a high degree of fluctuation, the helices remain stably immersed in these channels throughout the course of all of the simulations. The terminal regions of helix-C are frayed, but stable, and the helices themselves follow a somewhat tortuous path

through the channels: rarely are they straight. The major features of the NMR structure are conserved throughout the simulations [279]. In particular, as illustrated in **Figure 5-2**C, the non-polar sidechains orient towards the micelle center, basic sidechains (αS is lysine rich) orient along the micelle surface and form salt-bridges with the sulfate headgroups, and the acidic sidechains orient into the solvent. A similar motif has been observed in apolipoproteins [288]. Within the N-terminal region of αS, there are seven imperfect copies of an 11-mer repeat, most of which contain two (*i*, *i*+2) lysine residues. In all cases, these paired sidechains point in opposite directions along the micelle surface, exerting a strong influence on helical depth and topology. In agreement with previous observation, the highly hydrophobic sixth 11-mer repeat buries deepest into the micelle [279, 281, 289]. This section of the protein is within the largely hydrophobic NAC (residues 60-95), the region which is thought to drive fibril formation [290, 291]. We have calculated the C^{α} root-mean squared deviation (RMSD) from the NMR structure, a quantitative measure of stability and equilibration. Helix-C shows slightly elevated deviation as compared to helix-N, though the values of ~2-4 Å for both are typical for protein simulations and indicate that the structure is equilibrated and the simulations are converged. An indication of the micelle's role in stabilizing α-synuclein's structure, the RMSD calculated from the simulation of the protein in water (i.e. no micelle) reached 12 Å after only 5 ns.

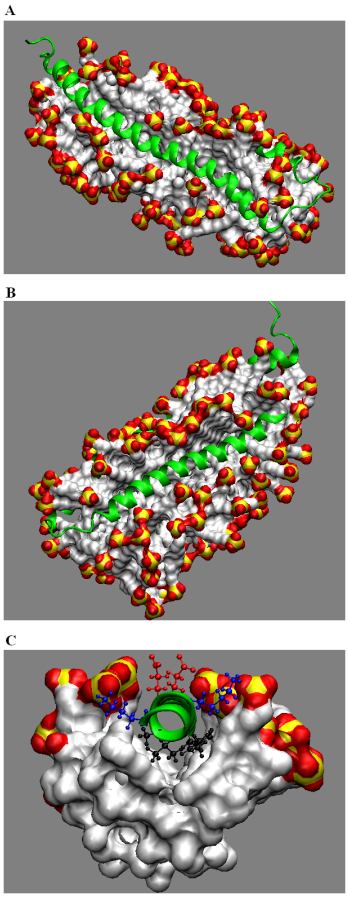

Figure 5-2 Micelle-Bound Snapshots - Snapshots of wild-type αS bound to the detergent micelle, after 45 ns of simulated dynamics. The protein embeds deeply into the core of the micelle, forming channels in both helix-C (A) and helix-N (B). C) A representative slice through the micelle, illustrating typical sidechain orientations. Non-polar sidechains (black) are directed towards the micelle center, basic sidechains (blue) orient along the micelle surface, and acidic sidechains (red) orient towards the water. αS backbone is represented as a green ribbon. The SDS micelle is shown with the following color scheme: white = carbon, yellow = sulfur, and red = oxygen. Hydrogens, water, and ions have been removed for clarity of presentation.

In both the wt and mutant simulations, αS binding significantly perturbs the equilibrium structure of the SDS micelle. As is readily apparent from **Figure 5-2**, the micelle flattens into an elongated, ellipsoidal (rod-like) shape. The deformation is quantified by a 20% increase in the radius of gyration (23.6 Å *vs.* 19.5 Å in the case of the protein-free micelle). Quantifying the area per headgroup for an irregularly shaped structure, such as the micelle, can be done by measuring the solvent accessible surface area (SASA). The change in micelle shape upon αS binding is accompanied by an

approximately 10% decrease in SASA, a substantial change that will be discussed in detail below. Differences in SASA between the αS variants were negligible.

In Figure 5-3 we show snapshots of wt αS bound to a negatively charged DOPS bilayer. Over the course of the 50 ns simulation, the helices submerged more than 5 Å more deeply into the bilayer core than their starting positions and flattened significantly. The RMSD suggests that the bilayer simulations are reasonably well-converged, though there remain subtle changes in the helix positions throughout the 50 ns.

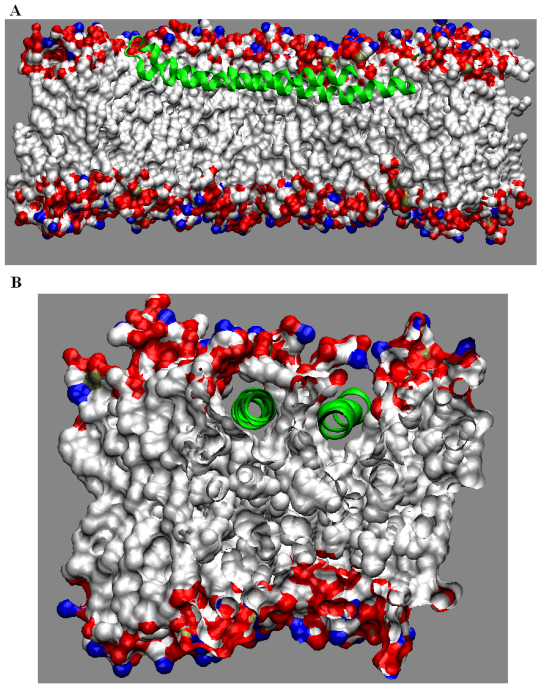

Figure 5-3 Bilayer-Bound Snapshots - Snapshots of wild-type αS bound to the DOPS bilayer, after 45 ns of simulated dynamics. The protein embeds into the hydrophobic core of the bilayer, beneath the lipid headgroup. αS backbone is represented as a green ribbon and the DOPS bilayer is shown with the following color scheme: white = carbon, red = oxygen, blue = nitrogen, and tan = phosphorous. Hydrogen, water, and ions have been removed for clarity of presentation.

Figure 5-4 presents the electron density profiles (EDP) for the molecular constituents of the wt system. EDPs are commonly used to describe the location of molecules and their chemical components within a bilayer. The figures indicate that the two helix backbones are submerged just beneath the lipid headgroup/water interfacial region, allowing the hydrophobic face of the protein to interact with the lipid

hydrophobic core and the hydrophilic face of the protein to interact with the lipid polar region and water. Helix-N ends up at a depth of ~3 Å beneath the lipid headgroup phosphates, in agreement with a recent experimental study [292]. Helix-C buries an average of ~2 Å deeper into the bilayer center than helix-N despite having started at the same depth. This result is consistent with our micelle simulation and previous studies [279, 281, 289]. As in the micelle-bound state, the turn region projects outwards from the bilayer. This molecular architecture leads to a substantially different binding environment for the protein in the bilayer (Figure 5-3B), as compared to the micelle (Figure 5-2C). In contrast to the micelle, portions of the protein are fully ensconced in the lipid (a subset of the lipid headgroups hang over the helices and directly interact with the polar sidechains). Thus, the protein appears in places to tunnel through the bilayer, although there are regions where the protein is also exposed to the water. This additional degree of incorporation may underscore a tighter interaction with the lipids than detergents, and likely explains an overall decrease in dynamics of the bilayer-bound proteins, as described below.

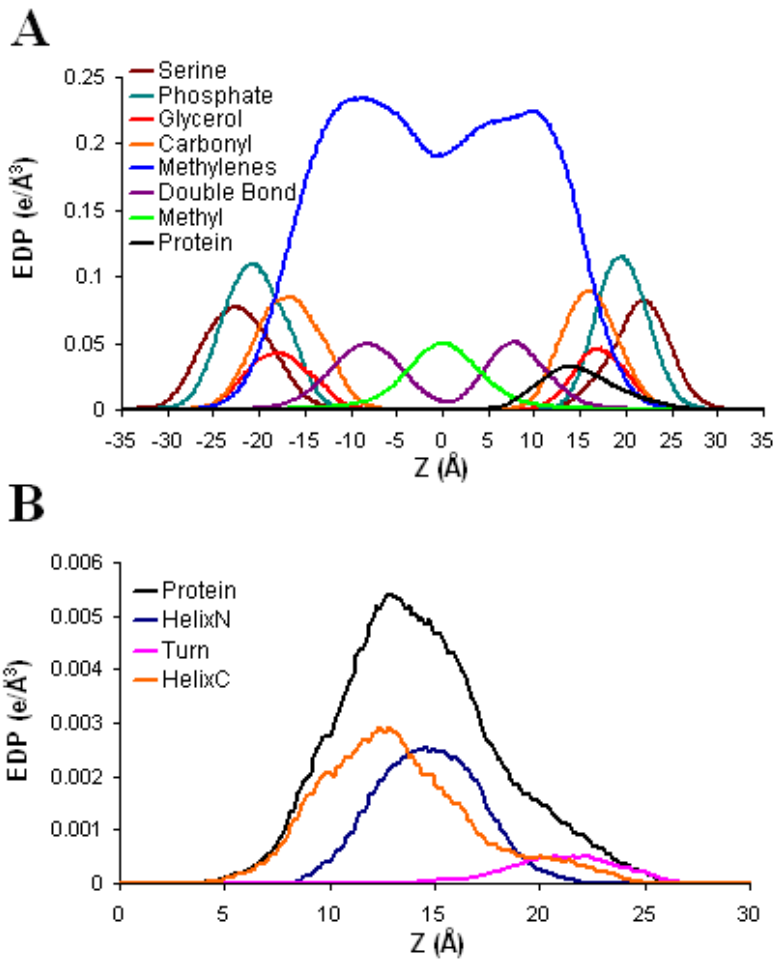

Figure 5-4 Electron Density Profiles – A) Component electron density profiles (EDP) for DOPS bilayer and wild-type αS. B) C^{α} electron density, describing relative backbone depth of the protein helices.

5.3.2 Protein Dynamics

The simulations provide insight into similarities and differences in how the micelle and bilayer affect dynamic deviations from the average NMR structure for the wt and mutant proteins. The root mean squared fluctuation (RMSF) provides a quantitative measure of a protein's Cα motion on a per residue basis and a first look at changes induced by the mutations. Figure 5-5A compares the RMSF for the micelle-bound wt with the A53T, A30P, and E46K mutants. Consistent with experimental measurements, the maximal dynamics of the wt protein occur in the non-helical regions: the N- and C-terminals of the protein, as well as the turn (residues 38-44) for each of the proteins for which experimental data is available [260, 279]. The first two residues of the N-terminus

interact intimately with the detergent, whereas the C-terminal residues downstream of Gly93 extend out of the micelle, into the water, causing a sharp increase in RMSF (data has not been included in the graph). The RMSF also indicates a high degree of flexibility near residues Gly67 and Gly68, as well as downstream of Gly82 and Gly84. Interestingly, the wt RMSF is greater in the helix-kinking region of Gly67/Gly68 than in any of the mutants, with the greatest reduction in the case of A30P. As would be expected, there is a clear maxima, and subtle increase over wt, in the dynamics around the site of the proline substitution. Less expected is an increase in dynamics in that same region in the E46K mutant, with a maximal value at residue 24. E46K dynamics are reduced immediately upstream of position 46, in the turn-region. A30P and E46K display less dynamics throughout helix-C, suggesting that this measure can not be directly correlated with experimental binding affinity. The threonine substitution behaves similarly to the wt, though there is a subtle decrease in dynamics in helix-N and in helix-C near Gly67/Gly68, as well as a slight increase in dynamics at Gly82/Gly84. Direct comparison of simulated αS dynamics to experiment is made through the NMR measured S^2 [260, 279]. We have calculated the S^2 data from the simulations, overlaid with the experimental data for wt, A53T, and A30P [260, 279] (data not shown [129]). Experimental results for E46K have not yet been published. While direct comparison between the experiments and simulation is difficult, and there are some elements of the simulation that do not exactly reproduce the experimentally observed behavior, all of the major trends upon which our results are based are reasonably consistent with experiment [293].

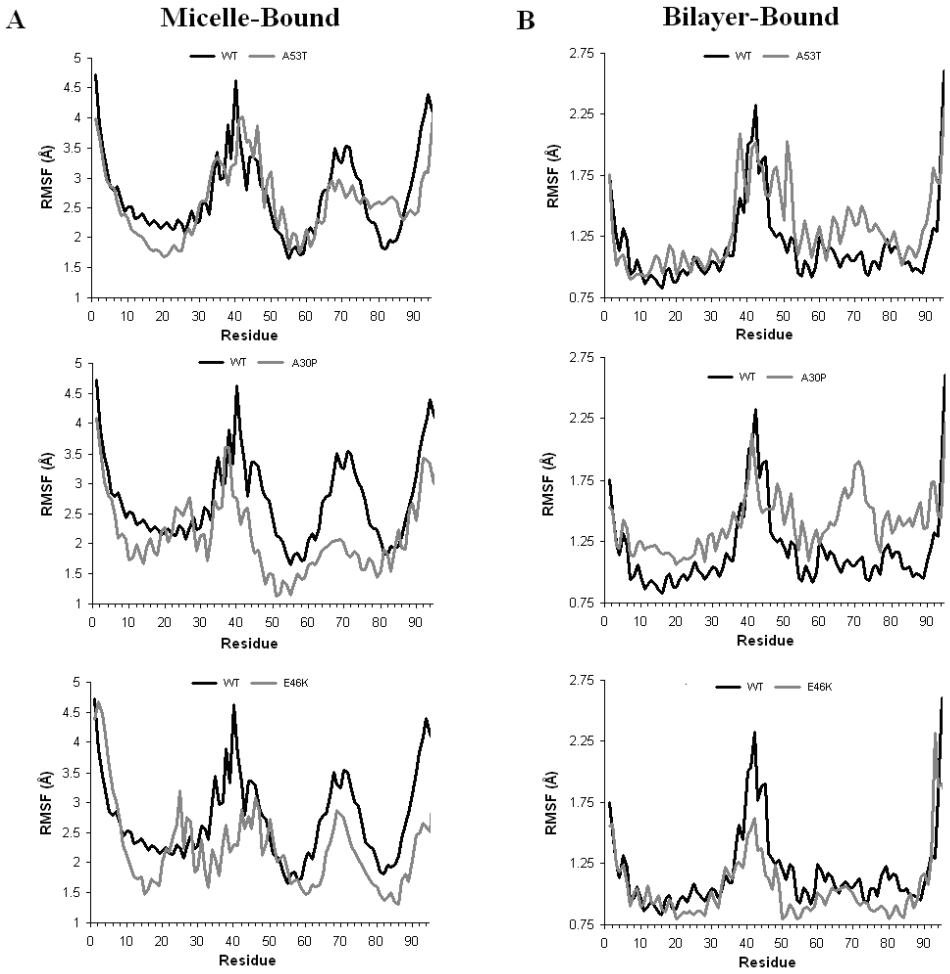

Figure 5-5 RMSF Dependence on Environment and Sequence - The root mean squared fluctuation (RMSF) of αS C^{α} calculated from the eight simulations, in each case averaged over the last 25ns for the micelle-bound (A) and bilayer-bound (B) states.

Figure 5-5B shows RMSF data for the bilayer-bound αS variants and indicates an overall decrease in protein dynamics of 2-3 foL_d as compared to the micelle-bound forms. We have checked to ensure that this reduction is not due to the different force-fieL_ds (as stated in section 5.2-Methods). A comparison between GROMACS and CHARMM bilayer-bound dynamics has been made and the similarity in magnitudes justifies comparison of our micelle- and bilayer-bound simulations. The general features of the bilayer-bound RMSF data are broadly similar to the micelle forms: the largest maximal values are in the non-helical segments and the turn. Remarkably, a maximum is seen at the Gly67/Gly68 hinge in all variants except the wt, where it has completely vanished

(the RMSF curve is concave for the mutants but flat for the wt). The micelle trend for A53T and A30P are reversed in the bilayer: both display an *increase* in their overall dynamics (relative to wt). In contrast, the E46K mutant displays a slight suppression of dynamics. As is always the case with simulation, these trends might change given significantly longer timescales.

A subset of the overall dynamics, helical bending is of particular interest. Bending can reflect at least two things: 1) equilibrium fluctuations that tightly couple the shape of the helices to that of the highly malleable micelle or more rigid bilayer or 2) perturbation induced by mutation that disrupts these normal interactions. Helical bending was calculated at each residue as the angle between the two helical-axes formed by the residues four up-stream and four down-stream, and the results for the micelle-bound states are given in Figure 5-6A. Both the wt and A53T protein show minimal bending in helix-N, while the A30P and E46K mutants bend significantly (as much as 40° in A30P and 25° in E46K). In the A30P protein this increase occurs up-stream of the substitution (maximally at position 25) where it is, on average, approximately twice as bent (≈ 40°) as the wt is at its position of maximum bending (just downstream of Gly67/Gly68). In helix-C, the proline substitution has a significant effect in reducing the bend around Gly67/Gly68, indicating long-range effects that act through the detergent. In contrast, the E46K system displays a large increase in bending in helix-C. In the A53T mutant, the bending is of roughly the same magnitude as the wt. The A53T mutant also shows increased bending at Gly82/Gly84 in helix-C. Collectively, the effects of each mutation on the RMSF and bending in the micelle-bound form indicate that the two helices are not fully independent, despite being physically sequestered by the detergent.

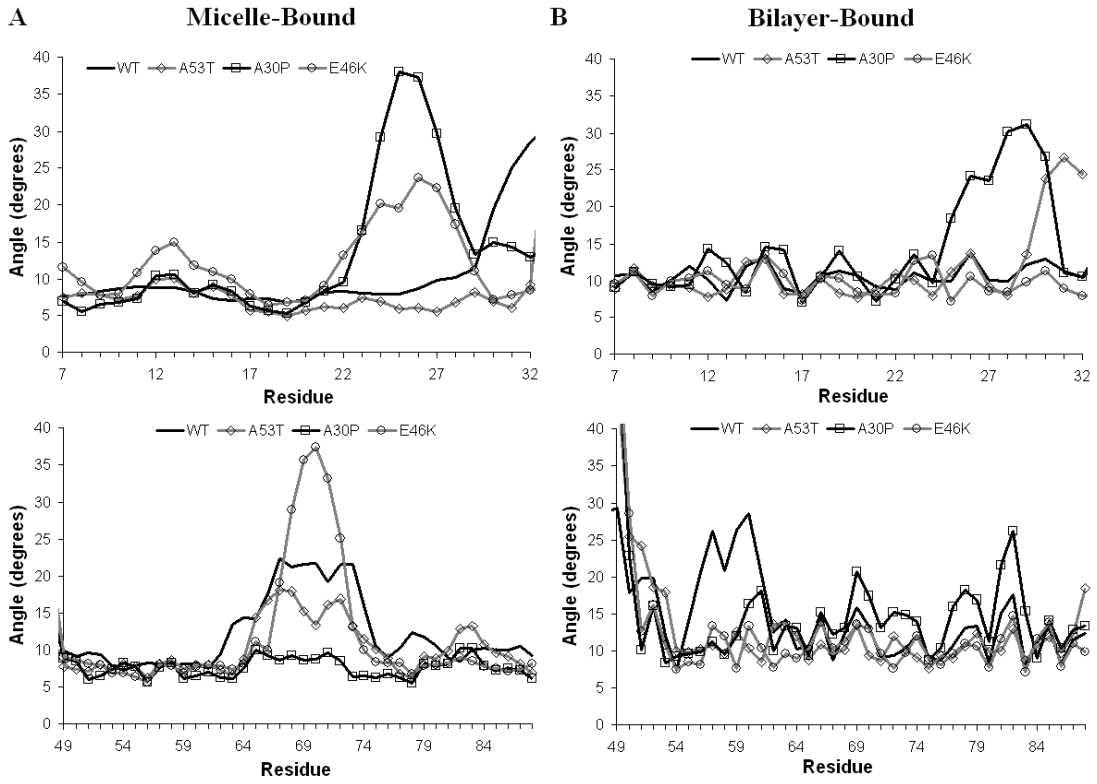

Figure 5-6 Bending Dependence on Environment and Sequence - The angle formed by the intersection of the residues four up- and down-stream at each helical position describes the helical bending in the micelle-bound (A) and bilayer-bound (B) states.

Helical bending in the bilayer-bound state is shown in Figure 5-6B. In helix-N, A30P displays an increase in bending, at approximately the same location as in the micelle-bound state, though slightly lower in magnitude. Similarly, the wt and A53T mutants show minimal bending in helix-C. However, in contrast to the micelle-bound state, E46K shows minimal bending in helix-N. The bending in helix-C is entirely different in the bilayer-bound state than in the micelle-bound form. Whereas in the micelle-bound structure each protein showed an increase around Gly67/Gly68, in the bilayer-bound form only A30P shows a small increase in bending at that point. A30P also shows a small increase in bending around Gly82/Gly84. Interestingly, the wt shows a maximal bending value at residue 60, a position in which bending is not observed in the micelle-bound state.

In Figure 5-7 we show a time series of the changes in bending angle at the position of Gly67/Gly68 from the wt micelle-bound and bilayer-bound simulations.

Snapshots illustrate the extreme values, as the micelle-bound helix fluctuates between nearly straight and highly bent. The bilayer-bound protein equilibrates at a relatively low angle (≈ 15°). It is highly interesting that in the latter part of the simulations the average bending is similar in the two environments, perhaps suggesting that the protein itself has this as its preferred-state. Consistent with the overall increase in RMSF, though, the micelle-bound form samples a wider range of angles. These lower angles are about half that of the averaged NMR structure, likely a consequence of the simulated micelle being larger than the experimental average.

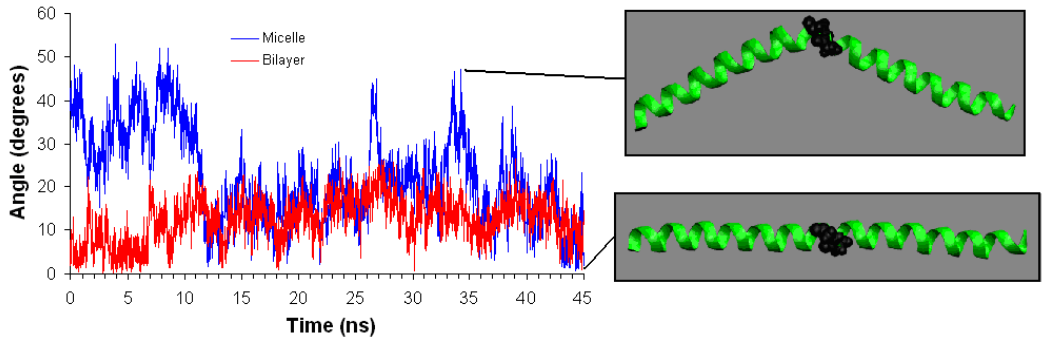

Figure 5-7 Bending at Gly67/Gly68 - The bending angle at Gly67/Gly68 is calculated at each time-point in helix-C, as described in the text, for the micelle-bound (blue) and bilayer-bound (red) states. The micelle-bound state shows a large range of values, capturing nearly straight as well as highly bent structures, whereas the bilayer-bound state remains relative straight. Representative snapshots from the micelle-bound state at the indicated timepoints show minimal and maximal bending conformations (the micelle, water and ions have been omitted). The helix is represented as a green ribbon and Gly67/Gly68 are shown in the space filling representation as black.

5.3.3 A30P: Destabilization and Unfolding

The proline substitution is known to alter the helical content of αS [259, 260, 263, 266], and the simulations reproduce this result. We have calculated the helical content on a per residue basis for the micelle-bound A30P protein compared to the wt. In all simulations, the turn region is completely without secondary structure. Consistent with the RMSF and bending data, helicity is disrupted upstream of the proline substitution. Snapshots in Figure 5-8A illustrate three loosely defined categories of helical structure observed in micelle-bound A30P: straight, kinked, and unfo$L_d$ed (i.e. loss of i,i+4 hydrogen bonding and change in geometry including backbone torsion angles). There is no significant

reduction in helicity in the micelle-bound forms of A53T or E46K mutants, also consistent with experiment [259, 260, 263, 266, 268, 271].

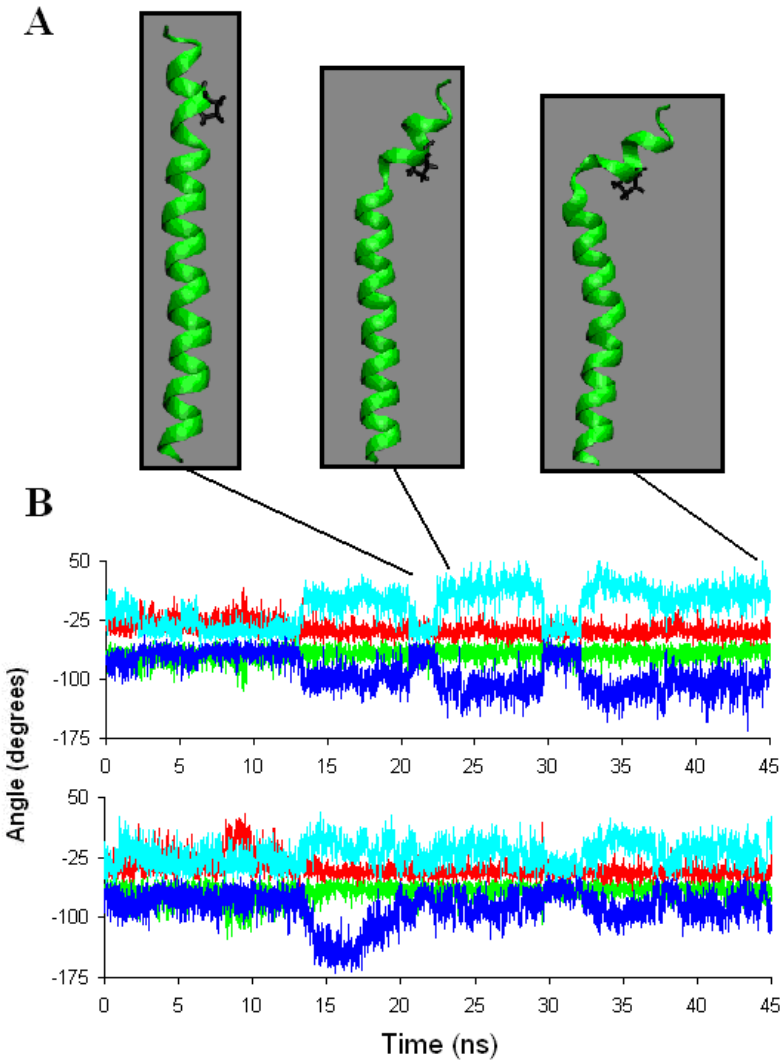

Figure 5-8 A30P Induced Unfolding – A) Snapshots illustrating different conformations of the A30P mutant from the micelle-bound simulation: straight helix, kinked helix, and unfo$L_d$ed (timepoints 21ns, 24 ns, and 45ns). Helix-N is represented as a green ribbon, the proline is shown in black (micelle, water and ions omitted). B) Torsion angles for the A30P substitution mutant and wild-type proteins for residues 26 and 28 from the micelle-bound simulations show reversible unfolding.

Another way to present these dynamic transitions is through the time-evolution of backbone torsion angles. During a 15 ns pre-equilibrated period of dynamics there were

significant deviations in the wt from typical α-helical torsion angles in certain residues. Throughout the remainder of the simulation, the wt protein displayed torsion angles for all residues that are close to that of a typical α-helix ($\varphi \approx -62°$, $\psi \approx -41°$ [269]) . The proline substitution induces substantial deviations from helicity, in particular at Val26 and Glu28. Figure 5-8B overlays the results for residues 26 and 28 in the micelle-bound wt and A30P. Ala27 and Pro30 show more subtle variation, as do residues Gly25, Thr33, and Lys34 (data not shown). The time-evolution of these structural fluctuations is illuminating, showing a dynamic volley between unfoLded and helical: unfoLded regions can refoLd on the nanosecond timescale, particularly evident at residue 26. The structural transitions back to a helical state for this residue, however, appear to mostly dissipate towards the end of the simulation, suggesting that the secondary structure may be fully broken by this point. It is not clear, given the brevity of our simulated timescale, whether these transitions will continue, or whether the equilibrium structure is indeed completely unfoLded at this, or other, sites. Given the experimental evidence for the latter, and the data in Figure 5-8, it is likely that unfolding of the bound A30P nucleates at residue 26, but does not extend beyond 4-5 residues up- or downstream of the mutation site. Whether this unfolding would lead to unbinding given a significantly longer simulation, remains an open question. A comparison of the time-dependent changes in torsion angles and helical bending directly correlates A30P unfolding with maximum bending angles in the N-terminal helix (data not shown). This is in contrast to the high bending angles at Gly67/Gly68, which are not accompanied by a loss of helicity.

The A30P bilayer-bound simulation shows only minor unfolding. Figure 5-5 and Figure 5-6 showed an increase in the backbone RMSF and helical bending relative to the wt, suggesting that the mutation destabilizes the protein in the same region as in the micelle-bound simulation. However, the helicity and backbone torsion angles are only subtly affected (data not shown). In this case, it must be noted that equilibration in bilayers is likely a slower process given the relative relaxation rates of the lipids and detergent and, as a result, the timescale for full unfolding in the bilayer is possibly longer than we are able to simulate. Torsion angle dynamics for A53T are indistinguishable from wt in both environments: there are no unfolding transitions. This lack of gross

structural change agrees well with experimental observation [259, 260, 263, 266, 268]. Structural analysis of sidechain orientation also reveals no discernable differences between the A53T mutant and the wt (data not shown). Helicity is preserved in E46K and all of the bilayer simulations, with only subtle deviations in torsion angles (data not shown).

5.3.4 A53T: Intra- and Inter-molecular Hydrogen Bonding

Recent NMR results measuring protein dynamics at longer timescales (nano- to milli-seconds) have suggested that the micelle-bound A53T mutant includes an unresolved, enthalpically stabilizing motif [260]. Indeed, Figure 5-9 reveals that the secondary structure of helix-C is likely stabilized in the A53T mutant by an intra-protein hydrogen bond that forms between the threonine hydroxyl and the backbone carbonyl of Val49. Figure 5-9A plots a time-series that illustrates the dynamics of this partnership in the micelle-bound system. The hydrogen bond was not present at the onset of the simulation. In fact, during the pre-equilibration period (<15 ns) the hydroxyl group was stabilized by interactions with the SDS and surrounding water. This clearly indicates that the hydrogen bond is not a product of the initial starting configuration, but rather the natural, equilibrated structural motif for A53T. Figure 5-9B shows that the same sidechain-backbone hydrogen bond forms in the bilayer-bound simulation of A53T, however it is noticeably less stable, flickering on and off throughout the simulation. Instead, a different stabilizing interaction predominates: the hydrogen bond forms with the lipid's glycerol backbone carbonyl. SDS has no hydrogen bond acceptors beneath the micelle surface that can compete for threonine's donor hydrogen in this way.

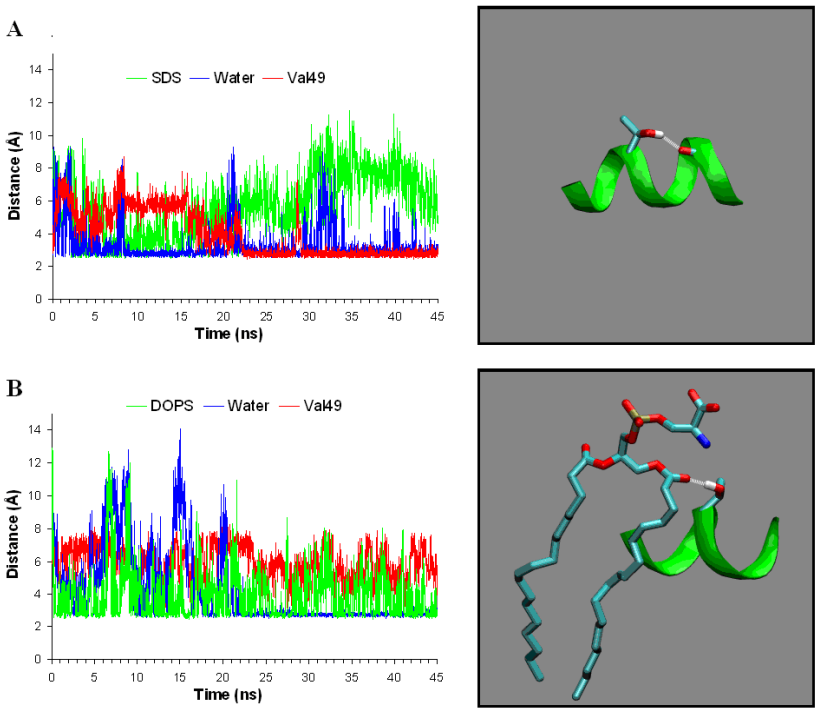

Figure 5-9 A53T Interactions – A) Minimum distance between Thr53 sidechain donor oxygen and water oxygens (blue), SDS oxygen hydrogen bond acceptors (green), and Val49 backbone carbonyl oxygen (red). B) Minimum distance between Thr53 sidechain donor oxygen and water oxygens (blue), DOPS oxygen hydrogen bond acceptors (green), and Val49 backbone carbonyl oxygen (red). Representative snapshot illustrating the hydrogen bond between the Thr53 sidechain and Val49 backbone taken from the micelle-bound simulation (top right) and DOPS carbonyl (bottom right). Micelle, bilayer, water, ions, and hydrogens have been omitted for clarity. Backbone is represented as a green ribbon, Thr53, Val49, and DOPS are represented with the following color scheme: white = Threonine donor hydrogen, light blue = carbon, red = oxygen, blue = nitrogen, tan = phosphorous.

5.3.5 E46K: Putative Increase in Binding Affinity

The E46K substitution leads to an additional intermolecular interaction which is very similar in both environments. As illustrated in Figure 5-10, the substituted lysine sidechain interacts with the SDS headgroup or the lipid hydrogen bond acceptors (primarily the carbonyl groups), as well as with water, throughout the course of the simulation. No intra-protein interaction is observed. While this interaction likely contributes to the E46K mutant's increased membrane affinity, it has also been suggested that a structural rearrangement may contribute [270]. In the micelle-bound simulation, there is an increased interaction between the micelle and the protein turn region (residues 38 to 44), which is reflected in the decrease in RMSF (Figure 5-5A). Long-range changes in

the RMSF (i.e. far from the mutation) suggest a global change in dynamics, in agreement with a recent experimental study [271]. Significantly, in the bilayer-bound state of E46K, helix-C buries ~1-2 Å deeper than wt, though helix-N appears to submerge to the same depth as wt.

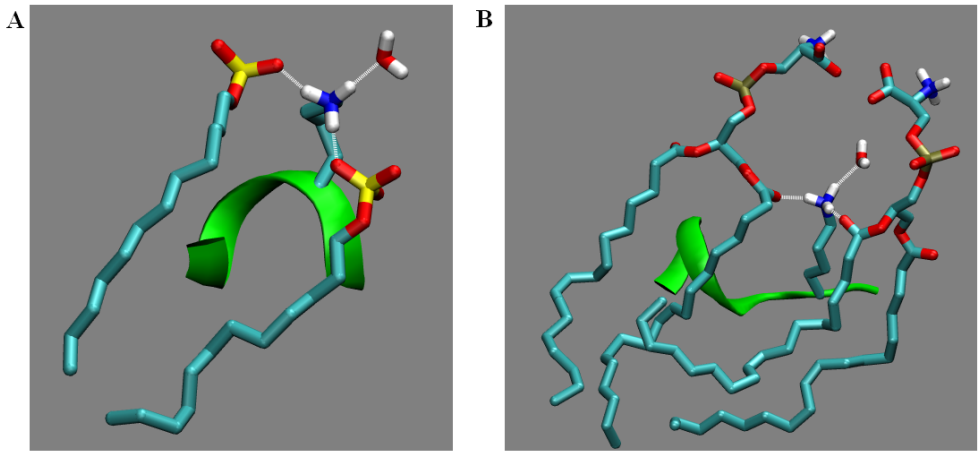

Figure 5-10 E46K Interactions - Representative snapshot illustrating the hydrogen bond between the Lys46 sidechain and SDS detergent (A) or DOPS carbonyl (B) and water (other detergent molecules, lipids, water, ions and aliphatic hydrogens omitted). Backbone is represented as a green ribbon, Lys46, SDS, DOPS, and water are represented with the following color scheme: white = hydrogen, light blue = carbon, yellow = sulfur, blue = nitrogen, and red = oxygen.

5.4 Discussion

As regards function and pathology, the behavior of αS on the surface of membranes has been the source of considerable uncertainty. Several studies have concluded that αS aggregation is triggered by interaction with membranes [261, 294, 295], while others suggest that membrane interaction inhibits the process [296]. Thus, as is the case with most membrane proteins, the dynamic behavior in the membrane environment is critical to function, but is only partially understood [297]. Recent NMR data, however, has revealed highly informative and intriguing dynamic information in the case of wt αS, A30P, A53T, and E46K. Indeed, it appears that the dynamics of αS, which were described as "unusually rich" [279], may be the critical piece in understanding the breadth of its interactions and behaviors.

Our efforts to understand the structure and dynamics of the A30P, A53T, and E46K mutants start with a detailed characterization of the wt. αS is a widely studied,

presynaptic protein with an unknown physiological function. Recently, it has been suggested that αS inhibits synaptic vesicle fusion after the docking of synaptic vesicles to the presynaptic terminal membrane [126]. Relative to other subcellular, membranous structures (such as lysosomes and endosomes), presynaptic vesicles are quite small, and are thus characterized by a higher degree of curvature. αS binds to lipid membranes, with highest affinity in the case of small, highly curved vesicles, and this interaction is thought to be tightly coupled to the protein's structure [127, 128, 276]. Indeed, the NMR structure supports this notion, demonstrating that the protein itself has a propensity to shadow the binding surface of a micelle by adopting a highly curved, helical structure [279].

In general, the spontaneous curvature of a membrane's component lipids is a significant factor in determining its fusogenic properties [113]. The curvature of a bilayer can be altered by the binding of a protein, which can either induce or relieve curvature stress [246]. Curvature stress is caused by a discrepancy between the intrinsic, spontaneous curvature of a subset of the component lipids and the actual shape of the bilayer. For example, a subset of the lipids may prefer to sit in a flat bilayer (e.g. those with a headgroup cross-sectional area similar to that of their chains) but be forced into a curved structure by the other lipids (e.g. those with a headgroup area less than their chains). Those flat-loving lipids would then be in a frustrated, or stressed, state. Area per headgroup, which is directly related to the intrinsic curvature, thus becomes a critical parameter in understanding the fusogenic tendencies of biological membranes.

Curvature stress is exploited by cells, allowing their membranes to overcome a thermodynamic barrier (high-energy intermediates) to fusion [113]. Membranes with high curvature stress are more likely to fuse with a flatter, target membrane in order to relieve that stress (the larger headgroup lipids will have found a more comfortable home). Likewise, any perturbation that ameliorates curvature stress lowers a membrane's propensity to fuse. One example of how a protein can alter curvature stress is the case of synaptotagmin-1, which encourages fusion of synaptic vesicles by inducing positive curvature in the relatively flat presynaptic terminal membrane [298]. Conversely, as would be relevant to the case of αS binding, synaptic vesicles are typically highly curved (they contain a large fraction of negatively charged lipids as well as lipids with both positive

and negative curvature [14]), and existing under curvature stress makes them fusogenic. A decrease in curvature should therefore stabilize the vesicles and inhibit fusion. Consistent with these ideas, a recently introduced theory is that αS binding relieves the curvature stress in small vesicles by reducing packing defects that are thought to occur in highly curved bilayers [127, 128].

MD simulation is a technique well-suited for studying the structural and dynamic behavior of membranes and membrane proteins [36, 153, 299-301]. Here, we confirm speculation that αS binding significantly deforms a micelle, and suggest that a similar mechanism may apply to lipid vesicles [260, 279]. It is known that cations can deform spherical (highly curved) SDS micelles into rod-like (flatter) structures [302]. By screening the charge-charge interactions between sulfate headgroups, which would otherwise be repulsive, the cations allow the detergent heads to pack closer together, inducing a change in shape. It has been suggested that the lysine residues in αS may have a similar effect [279]. Indeed, Figure 2 showed the elongated micelle-structure induced by αS binding, which was quantified by an increased radius of gyration and, perhaps most significantly, a decrease in the solvent accessible surface area, which correlates directly with area per headgroup. We note that while the above average size of the micelle results in a slight deviation from sphericity, the difference in structure before and after αS binding is incontrovertible. Our convergent results for wt bending at Gly67/Gly68 in the two environments (Figure 5-7) suggested that αS itself may have an intrinsic, preferred bend: perhaps it too is in a stressed state when bound intimately to a highly curved micelle or vesicle.

Given our results we infer a potential mechanism for wt function: αS flattens curved membranes by screening the repulsive interactions between negatively charged, acidic headgroups, thereby reducing the effective area per headgroup and relieving the inherent positive curvature of the lipids on the outer leaflet of the vesicle. This process ameliorates the driving force for fusion. Future simulations of curved bilayers should be aimed at addressing this possibility, though such efforts will likely require significantly more computer power than is currently available. Regarding the mutants, then, we hypothesize that reduced binding of A30P could decrease this inhibitory action of αS,

potentially leading to over-active neural signaling. Both the threonine and lysine substitutions are shown to increase direct interaction with the lipids through a hydrogen bond, which may then increase the protein's inhibitory potential.

The deformation of the micelle also serves to maximize both the favorable hydrophobic contact between the rather long helices and the core of the micelle, as well as the stabilizing electrostatic interactions between the sulfates and lysines [295]. The helices of αS are highly pliable, particularly around Gly67/Gly68, where they exhibit particularly high dynamics and helical bending. This is within the highly hydrophobic NAC (residues 60-95), which we and others observe to bury deeply into the core of the micelle/bilayer [260, 281, 289]. Therefore, the simulations suggest that αS bends in order to maximize contact area between the NAC region and the micelle.

Each mutation, and environment, has a distinct affect on the average magnitude of helical bending near Gly67/Gly68; relative to the wt, the micelle-bound A30P mutant suppresses bending, the E46K enhances bending, and A53T has little affect. If wt αS bends at Gly67/Gly68 in order to maximally insert the hydrophobic NAC region into the micelle center, than modulation of this bending may affect the amount of favorable interaction between protein and micelle. Therefore, changes in bending at the position of Gly67/Gly68 may contribute to the observed increased affinity of E46K, the decreased affinity of A30P, and the unchanged A53T affinity [259, 262, 263, 266, 270]. Our results suggest that this bending is less prevalent (at least on this timescale) in flat membranes.

In the region of the threonine substitution, the dynamics are nearly identical to those of the wt. This agrees with experiments which concluded that the dynamics on this timescale and the structure of αS is not affected by the A53T mutation [259, 260, 263, 266, 268]. However, experiments report a decrease in dynamics near the A53T mutation, on the nano- to milli-second timescale, outside the range of MD simulation [260]. How might A53T increase the stability of the helical state? It was pointed out in the NMR study that augmented $^{13}C^{\alpha}$ secondary shifts at the point of the threonine substitution are consistent with an increased helicity, and that this goes against the tendency for Ala→Thr mutations to destabilize secondary structure due to decreased entropy of the Thr sidechain relative to alanine. Indeed, Ulmer et al. speculated that a compensating, enthalpic interaction must

be responsible for this helix stabilization [260]. We have found that a hydrogen bond between the threonine and the backbone carbonyl positioned four residues up-stream may be responsible for this stabilization. In the micelle-bound state, this intra-protein hydrogen bond is highly stable, while in the bilayer-bound state, it competes with hydrogen bond acceptors in the lipid interface region, which may serve to stabilize the bound state of that mutant.

The E46K mutation removes a negative charge that presents a repulsive interaction in the wt. Therefore, this substitution is thought to cause an increase in electrostatic interaction (with SDS or PS) that may explain the observed increase in affinity of the E46K mutant for vesicles containing negatively charged lipids [270] and the observed equivalent affinity for neutral vesicles [271]. Indeed, the substituted lysine sidechain directly interacts with the micelle/bilayer. Though in the case of the bilayer, the hydrogen bond is formed most frequently with the carbonyl group and less frequently with the lipid headgroup, suggesting that the headgroup charge may not fully determine the extent of E46K affinity. Interestingly, both the micelle- and lipid-bound simulations suggest larger scale structural rearrangements that may contribute to an increase in affinity. In the micelle-bound state, we observe increases in dynamics in the N-terminal helix at the same positions where others have observed structural perturbations [271]. In the bilayer-bound state we observed helix-C to submerge deeper into the bilayer center. This suggests that changes in affinity due to this point mutation may be more complex than simply the addition of a single electrostatic interaction.

In the micelle-bound A30P simulation we observe a decrease in helicity as has been observed experimentally [259, 260, 263, 266, 268]. However, in the bilayer-bound state decreased stability is reflected in an increase in backbone dynamics, but only slight changes in structure. It is possible that A30P's relative stability in the bilayer environment represents a different equilibrated structure than in the micelle-bound state. However, an equally likely conclusion is that a longer simulation would be necessary to reach the final unfo$L_d$ed state in the bilayer-bound state.

A main feature of wt αS in the micelle-bound state, namely the large increase in fluctuations near Gly67/Gly68 relative to neighboring residues is, remarkably,

completely missing in the bilayer-bound form. We interpret this to mean that αS becomes somewhat locked into a stable conformation (i.e. the free-energy profile is steeply divergent from this conformation). This suggests that on a surface of intermediate curvature (e.g. a synaptic vesicle) the protein may respond by modulating the character of fluctuation at this hinge location. Does membrane curvature act as a switch that liberates or dampens relative fluctuations at this glycine hinge? Is this effect all-or-none, or do intermediate degrees of fluctuation exist depending upon the degree of curvature?

While each simulation began with an identical starting configuration, the equilibrium structures and dynamics of the mutants show deviations from wt that are highly informative. Each mutant does have its own particular local influence (i.e. at position 30, 46 or 53), but there is also one common, long-range effect. In the bilayer only, the RMSF curve for each mutant recovers the local maximum at the Gly67/Gly68 hinge-point that was lost in the wt (Figure 5-5). We are left with an unresolved question: does this commonality suggest a functional significance? While we must entertain the possibility that this result could be due to limited sampling of conformational space, we find it remarkable that these fluctuations are only absent in one of the eight simulations presented in Figure 5. Importantly, we also note the absence of these fluctuations in the wt, bilayer-bound CHARMM simulation, which increases our confidence that this is a real phenomenon.

A highly curved micelle surface and a flat bilayer patch represent two possible extremes of curvature. On the relatively flat bilayer surface, helical bending and dynamics of αS are considerably reduced as compared to the micelle-bound state. We therefore conclude that the extent of αS bending on highly curved surfaces (e.g. a micelle) is largely imposed by the curvature of the substrate, and that a defining, specifically evolved aspect of the primary sequence of αS is this inherent ability to adapt its structure. We have, in part, addressed the ways in which the familial PD mutants influence this adaptivity, though the exact relationship between αS curvature, dynamics, functionality and PD pathogenesis remains elusive.

III Computational Modeling of a Membrane Protein stabilizing Polymer

Preface

This chapter expands upon the relationship between membrane proteins and their environments to include a newly developed membrane-mimetic. Section I focused on subtle features of membranes which could potentially affect membrane protein structure. Section II then focused specifically on one membrane protein, α-Synuclein, and its response to changes its environment. The two distinct environments used were a lipid bilayer (a simple model of the physiological environment) and a detergent micelle (a commonly used membrane-mimetic for membrane protein characterization). Here in Section III we expand this investigation of the effect of environment on membrane protein structure to include another membrane-mimetic: an amphipathic polymer composed of a polyacrylate backbone with hydrophobic grafts. While this polymer has been demonstrated to effectively stabilize membrane proteins, it is thought that it may have an effect on membrane protein structure, distinct from that of membranes. Given that its intended use is characterization of membrane proteins, it is critical to understand how it might alter the structure of resident proteins. Chapter 6 presents the intial work of parametrizing the polymer model and characterizing the self-assembled particle. Section 0 presents preliminary work investigating the polymer – membrane protein complex.

6 All-Atom and Coarse-Grained Molecular Dynamics Simulations of a Membrane Protein Stabilizing Polymer

6.1 Introduction

Studying membrane proteins (MPs) *in vitro* is a notoriously difficult task [297, 303-305]. The most common method of making MPs water-soluble is through the use of detergents [306]. However, detergents by necessity are dissociative, meaning they disrupt competing interactions in order to solubilize the protein [307, 308]. This includes not only preventing non-specific aggregation, but also competing with the specific protein/protein and protein/lipid interactions that keep MPs native. As a result, most MPs become unstable in detergent solutions. Stabilization can be achieved by transferring MPs, after solubilization, to less dissociative environments [307, 308], among which are specially designed amphipathic polymers called amphipols (APols) [308-312]. APols, as a rule, greatly stabilize MPs as compared to detergents [308, 309, 312]. They have proven useful for a wide range of applications, including MP folding [313-315], *in vitro* synthesis [312], immobilization onto solid supports [316], radiation scattering [317-319], light spectroscopy [317, 320], electron microscopy [312, 321], as well as such practical uses as drug screening [316], diagnostics [316], or vaccination [322]. NMR studies show that MP/APol complexes can be used for obtaining high-resolution structures of MPs or their ligands [323-327].

Among several chemically different types of APols whose usefulness for handling MPs *in vitro* has been documented ([328-333] and for an overview see [312]), the most thoroughly used APol to date is A8-35 [309, 334]. In this nomenclature, the '*A*' refers to the poly*a*crylate backbone, chosen because it is highly flexible and allows the polymer to adapt to the small radius of curvature and irregularities of MP transmembrane domains [310]. The *8* refers to the initial estimates of the average molecular mass (~8 kDa, but see below) of single polymer chains after derivation with two grafts, octylamine and isopropylamine, at ratios of 35% ungrafted carboxylates, 40% isopropylamine, and 25% octylamine (Figure 1-1) [309, 310]. Derivation with isopropylamine, which reduces the number of free carboxylates, decreases the charge density along the chain [310]. The proportion of octylamine was adjusted so that the polymer remain highly soluble in water while becoming sufficiently amphipathic to adsorb onto the hydrophobic transmembrane

surfaces of MPs [310, 324-327], forming water-soluble complexes. In aqueous solution, A8-35 has been shown to self-assemble into well-defined globular particles, with a mass of ~40 kDa and a radius of gyration (R_g) of ~2.4 ± 0.2 nm, similar to detergent micelles [318]. Each particle comprises an average of ~80 octylamine chains, which are thought to form a hydrophobic core [318]. While the composition, size and solution properties of A8-35 particles have been extensively characterized experimentally [318-320], little is known about their internal organization nor their dynamics, two features thought to be relevant to the mechanism(s) by which A8-35 stabilizes MPs and favors their folding [310, 312-315, 335, 336]. In the present work, we have investigated these issues using molecular dynamics (MD) simulations.

In order to model A8-35 particles, we have utilized all-atom (AA) and coarse-grained (CG) MD simulations. AAMD simulation has proven to be a useful tool for studying the structure and dynamics of soluble proteins [19, 337, 338], lipid bilayers [36, 171, 193, 339], MPs [129, 340, 341], and polymers [159, 342-345]. However, the computational expense of explicitly representing every atom of the solute and solvent limits AAMD simulations to a timescale of tens of nanoseconds. In order to overcome this limitation, CGMD force fields have been developed, in which groups of atoms are represented by a single CGMD "bead." In particular, the Martini CGMD force field [133] has been used to study the microsecond time-scale behavior of many molecules, including lipids [133, 144], MPs [346], and polymers [159, 344, 347-349].

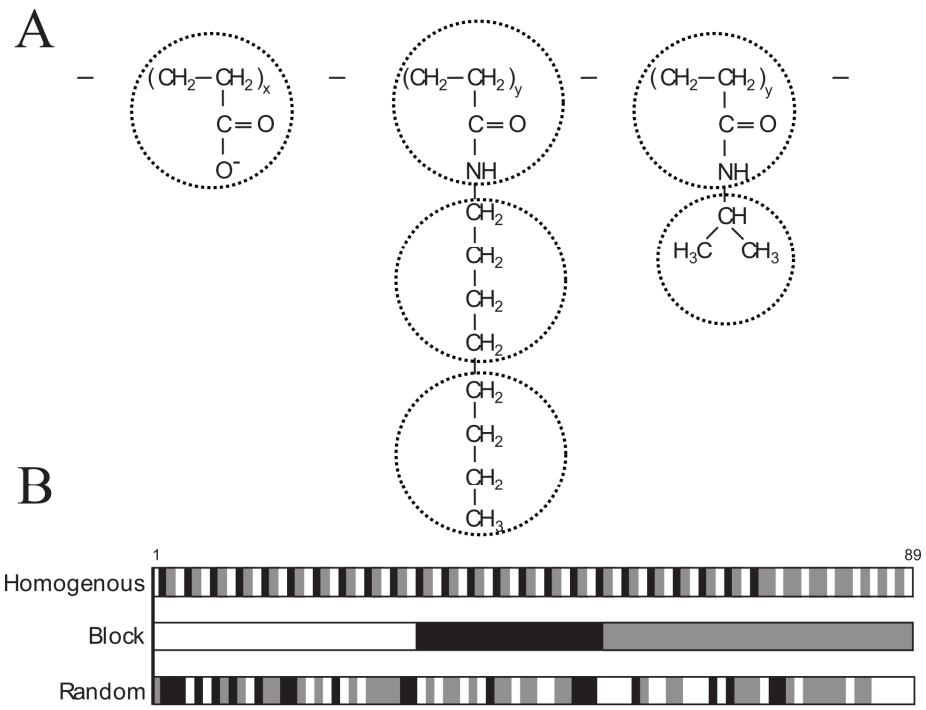

Figure 6-1 Chemical Structure and Grafting Sequence - A) Chemical Structure of ungrafted, octylamine grafted, and isopropylamine grafted units, with coarse-grained mapping. B) Grafting sequences simulated (white = ungrafted, black = octylamine grafted, gray = isopropylamine grafted).

Our multi-scale strategy is summarized in Figure Figure 6-2: we first present AAMD simulations of multiple A8-35 particles starting from arbitrary initial configurations. We then use the results of these simulations to parametrize a CGMD model. Using the CGMD model we are able to obtain 4 microseconds of simulation time and thus directly observe *de novo* the assembly of four polymer chains into a single particle. Finally, we present a third set of simulations, where we convert a set of coordinates obtained from the CGMD simulations into the AAMD resolution. This process of reverse coarse-graining (rCG) allows us to characterize the structures obtained from a multi-microsecond CGMD simulation using higher resolution AAMD simulations. For each of these three sets of simulations, we characterize the structure of the particles, emphasizing the extent to which the particles form a hydrophobic core, a critically important feature for the colloidal stabilization of hydrophobic MPs. These results represent a first step towards an all-atom MD study of MP/APol complexes. They also offer insights into possible mechanisms of stabilization of MPs by APols.

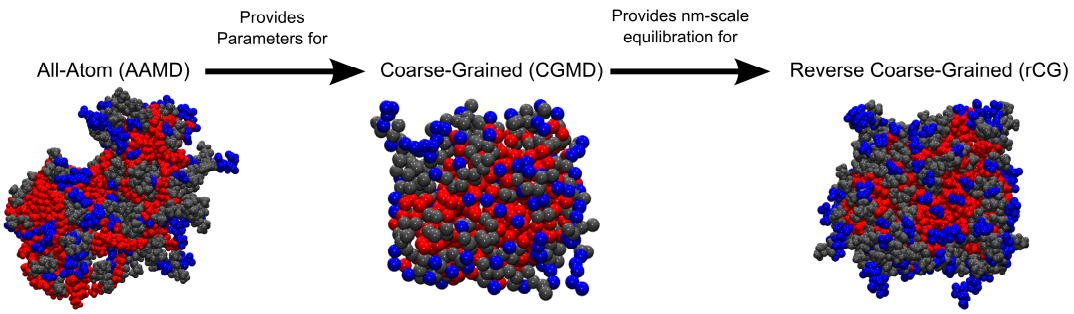

Figure 6-2 Multi-scale strategy overview - First, initial AAMD simulations are run and analyzed. Second, the AAMD simulations are used to parametrize a CGMD model. Third, coordinates from CGMD simulations are then used to start rCG (all-atom) simulations, allowing higher resolution characterization of equiilbrated particles.

6.2 Methods

6.2.1 Sequence Design

The sequence of a binary copolymer has been described using first-order Markov statistics and the following transition probability matrix [350]:

$$\mathbf{p} = \begin{bmatrix} p(A \mid A) & p(A \mid B) \\ p(B \mid A) & p(B \mid B) \end{bmatrix} \qquad \textbf{Eq 6-1}$$

where p($X \mid Y$) is the probability of a unit of type X following a unit of type Y. Conservation of probability provides two restraints, $p(A \mid A) + p(B \mid A) = 1$ and $p(B \mid B) + p(A \mid B) = 1$. If we define f as the fraction of unit A, then $f = p(A)$, and the third restraint is: $f = fp(A \mid A) + (1 - f)p(A \mid B)$. Using the nontrivial eigenvalue of **p**, we can define $\kappa = p(A \mid A) + p(B \mid B) - 1$, and the system can be fully determined using two variables, f (which ranges from 0 to 1) and κ (which ranges from -1 to 1), with κ indicating the degree of sequential correlation. At κ =-1, both $p(A \mid A)$ and $p(B \mid B)$ are 0, resulting in an alternating AB copolymer. At κ =1, $p(A \mid A)$ and $p(B \mid B)$ are both 1, and the result is a block copolymer. At κ =0, an entirely random copolymer forms.

While this formalism is for a binary polymer, it helps illustrate the sequences that we have used which we present graphically as Figure Figure 6-1B. The first sequence, which we will refer to as 'Homogeneous', is conceptually related to κ =-1, and primarily contains an alternating sequence of ungrafted-octylamine-isopropylamine, though the

sequence is not perfectly homogeneous due to the unequal proportions of the three components. We hypothesized that this sequence would show the least aggregation of octylamine grafts. The 'Block' sequence, related to the κ =1 case, is a triblock copolymer, designed to have a maximal ability to sequester octylamine grafts. Finally, a random sequence, idealized by κ =0, was generated to investigate an intermediate degree of octylamine sequestering and to model a sequence that may be more representative of those formed by statistical polymerization, as actually used in the synthesis of A8-35.

6.2.2 AAMD Simulation Setup

Most of the bonded and non-bonded parameters for the AAMD model were adapted from functional groups that have been previously parametrized in the CHARMM22 force field [351]. Based on the CHARMM atom typing scheme, Lennard-Jones parameters and partial charges are available in the CHARMM22 force field for all atoms in the amphipol molecule. Similarly, most of the bonded terms including bond lengths, angles, and proper and improper dihedral angles can be directly transferred from other molecules in the CHARMM22 force field without further optimization. However, the C-Cα-C angle, where Cα is the backbone carbon connected to the side chain graft, required an angle parameter that did not exist in the CHARMM22 force field. To parametrize the angle term for a 3 atom sequence of CHARMM atom types CT2-CT1-CT2, we chose N-metyl-3-ethylbutamide as the model compound and used the angle bending parameters for alkanes (CT2-CT1-CT1) in the CHARMM22 force field as initial input. AAMD parameters were determined to reproduce the geometries of the model compound from optimizations using hybrid density functional theory at the B3LYP/6-31G(d) level [352]. In the CHARMM force field the bending potential for this angle is the sum of a harmonic potential and a Urey-Bradley term to restrain the distance between the first and third atoms in the angle:

$$V_{Angle}(\theta,R)=\left[\frac{1}{2}K_{Angle}(\theta-\theta_{Angle})^2\right]+\left[\frac{1}{2}K_{UB}(R-R_{UB})^2\right] \qquad \textbf{Eq 6-2}$$

For the CT2-CT1-CT2 angle, we have found that the optimized parameters are K_{angle}=53.350 kcal/mol/rad^2, θ_{Angle}=114.000°, K_{UB}=8.000 kcal/mol/Å^2, R_{UB}=2.561 Å. The predicted C-Cα-C angle with the optimized parameters is 111.61º, which is in excellent with 111.62º obtained from the B3LYP/6-31G(d) calculation.

Each AAMD system was built with four polymer chains consisting of 89 units each, with charges neutralized by the addition of sodium ions, and solvated in a cubic box of water represented by the TIP3P model [353], large enough to avoid self-interaction through the periodic boundaries. A length of 89 units was chosen based on a 10 kDa chain [309, 319], without attributing any of the mass to sodium ions. As we discuss below, a series of simulations were performed in order to show that our assumed chain length has no significant effect on the particle properties. Systems were built using the CHARMM molecular mechanics package [165] and AAMD simulations were run using the NAMD molecular dynamics package [166], using the isothermal-isobaric (NPT) ensemble with a total of ~70,000 atoms, a constant pressure of 1 atm, and a constant temperature of 303 K. The temperature and pressure was controlled using the Langevin piston Nose-Hoover method [354]. A cut-off of 10 Å was used with a switching function for van der Waals interactions and particle mesh Ewald summation was used to treat long range electrostatic interactions [355]. All bonds involving hydrogen were fixed using the SHAKE algorithm [356]. A time-step of 2 fs was used and a total simulation time of 45 ns was run for each simulation.

6.2.3 CGMD Parametrization

As illustrated schematically in Figure Figure 6-2, we have used our AAMD simulations to parametrize a CGMD model. While it is a common strategy to parametrize a CGMD model from AAMD simulations, numerous procedures have been used, even within the Martini CGMD force field [133, 156, 159, 344, 346, 348, 349, 357-359]. We followed closely the method used recently in the parametrization of carbohydrates [357].

To obtain non-bonded parameters, we created a CGMD molecule for which the water/octanol partitioning coefficient matches that calculated from the AAMD model. This is done by determining the free energy of solvation for the polymer in the two distinct solvents (water and water saturated octanol), obtaining ΔG_W and ΔG_O, the difference of which is $\Delta\Delta G_{OW}$. This relates to the partitioning coefficient (P_{OW}) by:

$$\Delta\Delta G_{OW} = -2.3RT \log P_{OW} \qquad \textbf{Eq 6-3}$$

where R is the universal gas constant and T is temperature. Calculation of ΔG_W and ΔG_O is done using thermodynamic integration [360], where the potential energy describing the solute-solvent interaction (U) is scaled by a coupling parameter λ. When λ=0 there is no interaction (or the solute is a "dummy" molecule) and when λ=1 the solute-solvent interaction is fully occurring. By simulating the entire range of λ values between 0 and 1, a change in free energy can be calculated.

$$\Delta G = G_{\lambda=1} - G_{\lambda=0} = \int_{\lambda=0}^{\lambda=1} d\lambda \left\langle \frac{\partial U(\lambda)}{\partial \lambda} \right\rangle_{\lambda} \qquad \textbf{Eq 6-4}$$

This change in free energy can then be related to the solvation energy (ΔG_W or ΔG_O) by defining a thermodynamic cycle.

Our strategy is to use thermodynamic integration to calculate P_{OW} from the AAMD representation and then design the CGMD molecule such that its P_{OW} matches the AAMD result. In the Martini force field there is only one particle type representing charged particles (Q), and thus the particle type of the ungrafted unit is assigned without calculation (specifically to the Qa subtype due to the presence of a hydrogen bond acceptor). However, for uncharged particles, there is a gradient of 11 particle types, ranging from hydrophobic to polar, making the assignment through a quantitative comparison between the AAMD and CGMD representations preferable. Partition coefficients were calculated for a single unit, with either the octylamine or isopropylamine grafting. In the AAMD simulations, 25 λ values were simulated for 100 ps each (using a 1 fs time-step and totaling 2.5 ns per simulation and 15 ns altogether). The solvents consisted of either ~3,880 waters or 183 octanols and 67 waters (an octanol:water ratio similar to that used previously for this type of calculation [357, 361]). In

the CGMD simulations, 21 λ values were executed for 50 ns each (a total of ~1 μs per simulation and ~80 μs total). The solvents consisted of 2,049 water beads or 519 octanols and 43 water beads [357]. Note that in the Martini force field, each water bead represents 4 water molecules [133]. CGMD simulations were run using GROMACS molecular dynamics package as described below [230].

Bonded Parameters were obtained by comparison with the AAMD simulations of the A8-35 particle. The CGMD bond distances, angles, and dihedrals are taken from the AAMD simulation, by calculating the distances, angles, and dihedrals formed by the center of mass of the atoms mapped to the CGMD beads. In the CGMD force field, bond lengths are defined by a harmonic potential:

$$V_{Bond}(R) = \frac{1}{2} K_{Bond} (R - R_{Bond})^2 \qquad \textbf{Eq 6-5}$$

with an equilibrium distance R_{Bond} and force constant $K_{Bond.}$ In the Martini force field, angles are typically defined using a cosine-harmonic potential:

$$V_{Angle}(\theta) = \frac{1}{2} K_{Angle} [\cos(\theta) - \cos(\theta_0)]^2 \qquad \textbf{Eq 6-6}$$

All angles described below are parametrized using the form of Eq 6-6, with the exception of the backbone-backbone-backbone angle, for which we have found greater stability using a harmonic potential, similar to a recent polymer parameterization [344]. The form of this potential is the same as Eq 6-2, but without the Urey-Bradley correction. Proper dihedral angles have a multiplicity of 1 and are defined:

$$V_{Dihedral}(\Phi) = K_{Dihedral} [1 + \cos(\Phi - \Phi_0)] \qquad \textbf{Eq 6-7}$$

In order to determine the agreement between probability density functions representing the distribution of bond lengths, angles, and dihedrals in both representations, we quantify the intersection between the two distributions:

$$s = \int \min[f_{CG}(x), f_{AA}(x)] dx \qquad \textbf{Eq 6-8}$$

where *s* is between 0 (no overlap between these distributions) and 1 (complete overlap). Maximizing *s* maximizes the frequency with which the two representations have the same geometry.

6.2.4 CGMD Simulation Setup

Each CGMD simulation started with the four polymer chains in an entirely linear, extended conformation, separated from each other by at least 3 nm. Polymers were solvated in a box containing ~27,500 water beads and neutralizing sodium ions. Simulations were run using the GROMACS molecular dynamics package [230], and a constant number of atoms, constant pressure (1 atmosphere), and constant temperature (303 K), to form NPT ensembles. Pressure was controlled using the Berendsen isotropic pressure coupling scheme . A timestep of 30 fs was used and a total simulation time of 4000 ns was run for each simulation. Each sequence was simulated three times using the same initial starting configuration and alternate starting velocities.

6.2.5 Reverse Coarse-Graining

Our strategy for obtaining an AA representation from a polymer CGMD coordinate set is similar to our previously presented method for reverse coarse-graining (rCG) lipids bilayers [143]. The coordinates of each polymer CG bead is mapped to a single atom and the remaining atoms are assigned coordinates by CHARMM around these mapped atoms. As in our previous work, water and ions are not included in the reverse coarse-graining process, and the polymer is instead placed in a pre-equilibrated TIP3 waterbox [143]. An initial period of ~15 ns of dynamics is run with restraints placed on the mapped atoms in the polymer, during which the waterbox relaxes around the polymer. Simulations were then run for an additional 45 ns of unrestrained dynamics.

6.2.6 Analysis

The program CRYSON was utilized to calculate the small-angle neutron scattering (SANS) profiles from the atomic coordinates of each AA and rCG amphipol system [362]. The simulated scattering profile was normalized according to the experimental intensities [363]. The Guinier approximation [364] was used to calculate the radius of gyration (R_g) from the simulated SANS:

$$\ln(I(Q)) = \ln(I(0)) - \frac{Q^2 R_g{}^2}{3} \quad \textbf{Eq 6-9}$$

The R_g is obtained by plotting the scattering profile as a function of Q^2, in which case the slope of the linear fit within the low Q region is equal to $R_g{}^2/3$.

The shape of the particles is described by determining the three principal axes of inertia, $I_1 > I_2 > I_3$, and then finding the semiaxes of the ellipsoid (a,b,c) which has the same principal axes of inertia:

$$I_1 = \frac{1}{5} M (a^2 + b^2) \quad \textbf{Eq 6-10}$$

$$I_2 = \frac{1}{5} M (a^2 + c^2)$$

$$I_3 = \frac{1}{5} M (b^2 + c^2)$$

where M is the total mass of the particle. In the results, we present the a/c ratio, where a value of 1 indicates a sphere and larger values indicate increasing degrees of elongation. Analyses were performed using CHARMM [351], GROMACS [230], and a set of in-house perl scripts. Visualization was performed using VMD [167].

6.3 Results

6.3.1 CGMD Parametrization

The first step towards parametrizing a CGMD representation of a molecule is mapping the AAMD structure to a discrete number of CGMD beads. In the Martini force fieL_d each bead is typically composed of ~four non-hydrogen atoms [133]. The ungrafted unit contains 5 non-hydrogen atoms, and is mapped to a single bead (Figure 6-1A). The isopropylamine grafted unit is split into a backbone (BB) and a sidechain (SC), while the octylamine grafted unit is split into a backbone (BB) and two sidechain beads (SC1 and SC2), as shown in Figure 6-1A. This mapping strategy results in an uneven distribution of atoms in the isopropylamine grafted unit (5 atoms assigned to the backbone and 3 to the sidechain). However, it possesses two advantages: 1) It allows us to assign the same atoms to the backbone for both grafts and 2) It creates a molecule with a polar backbone

and hydrophobic grafting, instead of two beads which are intermediately polar, better representing the fundamental features of the molecule.

In the Martini force field, non-bonded parameters are determined by the bead type. For example, two hydrophobic beads will have a favorable Lennard-Jones interaction, while a hydrophobic bead and hydrophilic bead will have an unfavorable interaction. Assigning non-bonded parameters to the ungrafted unit is trivial; beads containing a charge are of the 'Q' category, and the presence of a hydrogen bond acceptor indicates the Qa subtype [133].

However, for charge-neutral beads there is a range of 11 possible bead types ranging from most hydrophobic (C1) to most polar (P5). Therefore, in order to assign the bead types and (thus the non-bonded interactions), we make use of the oil/water partitioning; an important feature for a polymer designed to segregate hydrophobic proteins. Calculating the oil/water partitioning is done through a series of thermodynamic integration calculations which allow us to determine the solvation free energy in octanol and water (see section 6.2.3 - CGMD Parametrization for more information). The difference in these solvation energies ($\Delta\Delta G_{OW}$) for the AA representation is -0.5 for the isopropylamine grafted unit and -5.7 kcal/mol for the octylamine grafted unit. These differences in free energy correspond to $\log P_{OW}$ values of 0.37 and 4.12 (Eq 6-3).

The next step is to create CGMD molecules which have $\log P_{OW}$ values equal to the $\log P_{OW}$ values of the AAMD representation. Table 6-1 presents $\log P_{OW}$ values for several combinations of bead types for the backbone (BB) and isopropylamine sidechain (SC). In bold is the combination we have chosen to use for the CGMD model, containing a backbone of type P3 and sidechain of type C4. The agreement between the CG $\log P_{OW}$ (0.43) and AA $\log P_{OW}$ (0.37) is excellent relative to a recent CGMD parametrization [357]. Additionally, intuitive comparison to other molecules parametrized in the Martini force field suggests that P3 and C4 are appropriate bead types for these molecules [133].

	C1	C2	C3	C4	C5
C5	3.92				
Nda	3.00				
P1	2.18	2.07		1.51	0.92
P2	1.90		1.55	1.24	
P3	1.09	0.98	0.71	***0.43***	-0.14
P4	0.89		0.54	0.25	

Side-chain

Backbone

Table 6-1 Isopropylamine Parametrization - Log P_{OW} values for isopropylamine grafted unit from CGMD simulations. Log P_{OW} value from AAMD is 0.37.

Table 6-2 presents the logP_{OW} values for several combinations of bead types for the BB and first sidechain (SC1) of the octylamine graft, with the second sidechain (SC2) set to type C1. A linear alkane consisting of four carbons should be the most hydrophobic type (C1), and therefore we expect both SC1 and SC2 to be type C1. The BB should be the same type as was chosen for the isopropylamine graft (P3). Indeed, as Table 6-2 shows, this combination produces a close match to the AAMD data, and is therefore is the most rational and internally consistent choice.

	C1	C2	C3	C4	C5
Nda	5.67				
P1					3.68
P2	4.60		4.21		
P3	***3.85***	3.71		3.17	
P4	3.64				

Side-chain 1

Backbone

Table 6-2 Octylamine Parametrization- Log P_{OW} values for Octylamine grafted unit from CGMD simulations. Log P_{OW} value from AAMD is 4.12. For each of these calculations, the second side-chain is type C1.

Bonded parameters are obtained through a similar strategy: the bond length, angle, and dihedral distributions are obtained from the AAMD simulations, and then the CGMD representation is altered until it matches the AAMD results. The bond length distributions for the AAMD representation and the simulations using the optimized CGMD parameter set are shown in Figure 6-3. We quantify the agreement between the two parameter sets by calculating the area overlap of the two curves, i.e. the fraction of the AAMD distribution which is matched by the CGMD distribution (Eq 6-8). For the bond lengths, the best agreement is obtained by the BB-BB bond (*s*=0.87). The worst agreement is from the isopropylamine BB-SC distribution, where the AAMD distribution is too narrow to be matched by a harmonic potential. Bonds of this nature, such as the similar Backbone – Side chain bond in the amino acid valine [346], are more stably modeled as distance constraints, though this leads to a relatively poor agreement (*s*=0.66). The need to balance stability and accuracy is a recurring issue in CGMD parametrizations. For the other two bonds, the AAMD distributions are matched relatively well by the CGMD model (octylamine BB-SC1 *s*=0.81 and octylamine SC1-SC2 *s*=0.86).

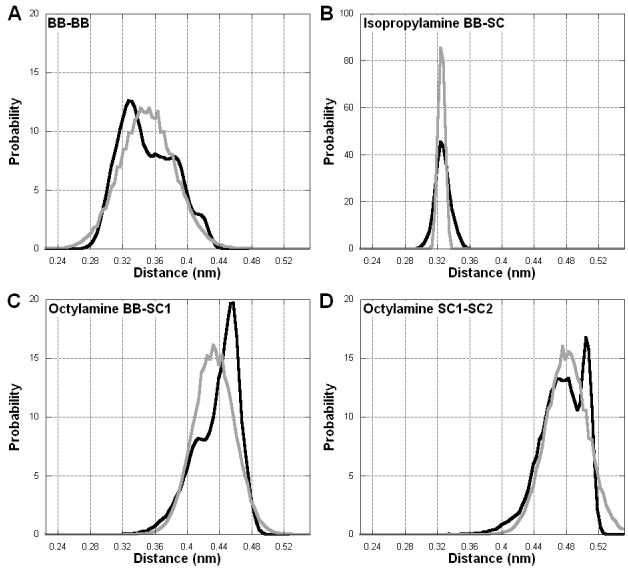

Figure 6-3 Bond Length Parametrization - Comparison of all-atom and coarse-grained bond length distributions (AAMD = black, CGMD = gray).

Parametrizing the angles used in the CGMD representation presents similar challenges, as shown in Figure Figure 6-4. Two of the CGMD angles match the AAMD data very well, BB-BB-SC s=0.93 and the octylamine BB-SC1-SC2 *s*=0.86. Note that the same BB-BB-SC potential is applied to both possible side chain graftings, as was the case for the protein parametrization [346]. In the case of the BB-BB-BB angle, increased stability was found using a harmonic potential, rather than a cosine-harmonic, and using a narrower distribution, as in a recent parametrization study [344]. Although this increases the stability, the agreement between the CGMD and AAMD models becomes relatively weak (*s*=0.69). Finally, the proper dihedral connecting four backbone beads matches the AAMD data very well (*s*=0.94). The bonded parameters are summarized in Table 6-3.

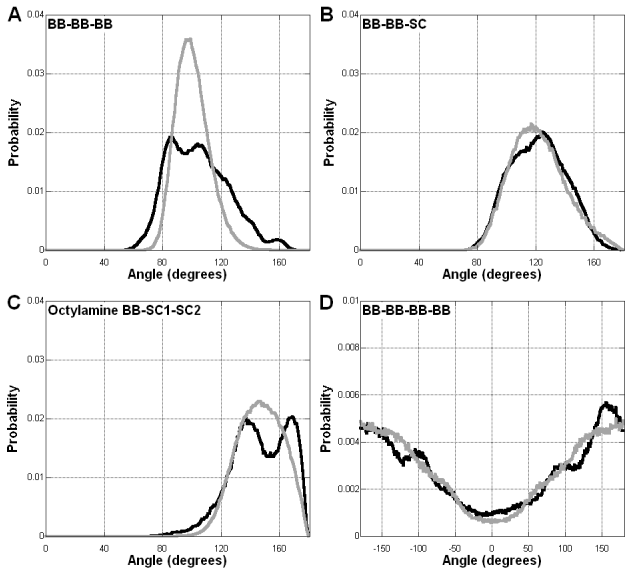

Figure 6-4 Angle Parametrization - Comparison of all-atom and coarse-grained angle and dihedral angle distributions (AAMD = black, CGMD = gray).

Grafting	Bonds	R_{Bond} (nm)	K_{Bond} (kJ mol^{-1} nm^{-2})	Angles	θ_0 (deg)	K_{Angle} (kJ mol^{-1})	Di-hedrals	Φ_0 (deg)	$K_{Dihedral}$ (kJ mol^{-1})
	BB-BB	0.350	2000	BB-BB-BB	80	20[1]	BB-BB-BB-BB	0	3
Iso-propylamine	BB-SC	0.325	n/a[2]	BB-BB-SC	120	5			

Octylamine	BB-SC1	0.435	4000	BB-BB-SC1	120	5
	SC1-SC2	0.485	4000	BB-SC1-SC2	180	30

Table 6-3 - Bonded Parameters for CGMD model. [1]Angle uses harmonic potential, rather than cosine-harmonic potential. [2]Bond is parameterized with a constraint, rather than a distance harmoic potential.

CGMD parametrization is complicated by the goal of creating a single set of parameters that are applicable in a variety of thermodynamic conditions [134]. However, it is not certain whether the same set of bonded and non-bonded parameters should be used for polymers with different grafting sequences, length, association number, or bound to a membrane or MP. We have investigated this question, and found only a weak dependence in the cases available to us. For example, the three AAMD simulations using different sequences have a very large degree of similarity, with each bond, angle, and dihedral having an overlap value $s>0.83$. We present additional information interrogating this issue as supplemental, though in general it remains a valid concern for all CGMD simulations.

6.3.2 A8-35 Characterization

In this section we characterize the particle structures formed in the three separate sets of simulations (schematically depicted in Figure Figure 6-2). The first set is the original AAMD simulations, which were obtained starting from an arbitrary initial configuration; however their limited duration prevents large scale reorganization. This motivated the parametrization of the CGMD model, as described above.

The second set of simulations uses the CGMD model to simulate *de novo* particle assembly. In Figure 6-5 we present snapshots from a CGMD simulation illustrating the assembly of four polymer chains into a single particle. The starting configuration is composed of four linear, extended chains, each separated by at least 3 nm. On a timescale of nanoseconds, the polymers collapse into individual bundles, partially shielding the hydrophobic octylamine chains from the solvent. This drive to shield the hydrophobic components leads to fusion of the separate chains into a single particle. While this fusion

requires overcoming the repulsion due to the negatively charged, ungrafted carboxylates on the particle periphery, we have observed fusion to occur in every case, although the rate varies from ~100 ns (as in Figure Figure 6-5) to ~1 µs. It is also important to note that the timescale of CGMD simulations is somewhat uncertain, and there is often a "speed-up" effect relative to AAMD simulations [133].

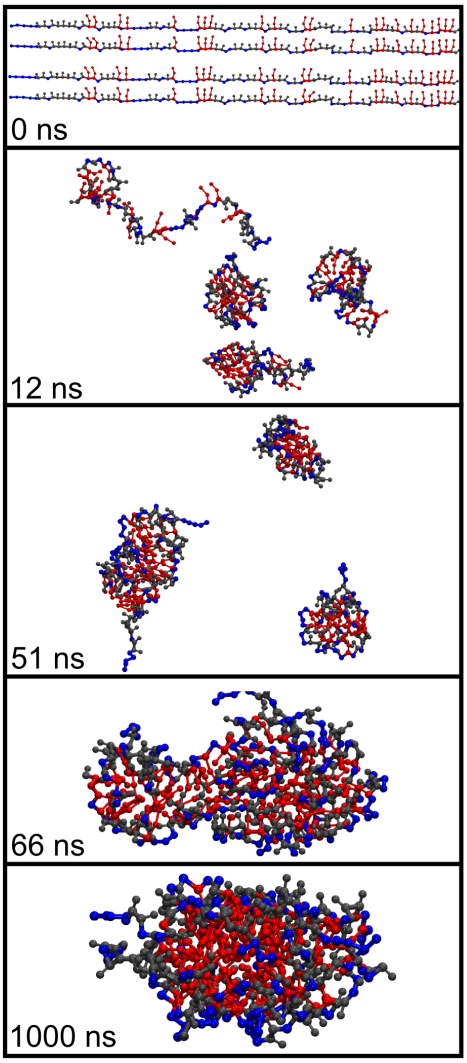

Figure 6-5 De Novo Assembly - Snapshots from CGMD simulation illustrating de novo particle assembly.

The third set of simulations employs the final configuration of the CGMD trajectory as the starting point for a set of simulations at the all-atom resolution. These reverse coarse-grained (rCG) simulations allow us to investigate the structure of these

particles using an organization derived from the CGMD model, rather than an arbitrary starting configuration, as in the original AAMD simulations. Over the course of the rCG simulations, the structure relaxes on the atomistic scale, as shown by the RMSD, but the larger scale molecular organization does not change.

This molecular organization is described by the radial component density distribution, presented in Figure 6-6. This figure most clearly shows the differences between the different simulation strategies. In the AAMD simulations of the Homogeneous and Random sequences, the components appear to be almost randomly distributed throughout the particle, with a minimal degree of segregation of the hydrophobic and hydrophilic components. Only in the Block sequence can we observe a strong tendency for the hydrophobic contents to be enriched in the center of the particle and charged components to be on the outside of the particle. However, in the CGMD simulations there is in each case a very clear pattern of separation: the side chains of the octylamine form a hydrophobic core surrounded by the ungrafted, charged carboxylates. For the CGMD simulations, each sequence was simulated three times, and the results are entirely consistent. We present in Figure 6-6 the average of the three simulations. In the rCG simulations, the distributions of components taken from the CGMD coordinates are stable, and there is no change in the organization on the nanosecond time-scale, though there is a difference in sampling between the resolutions.

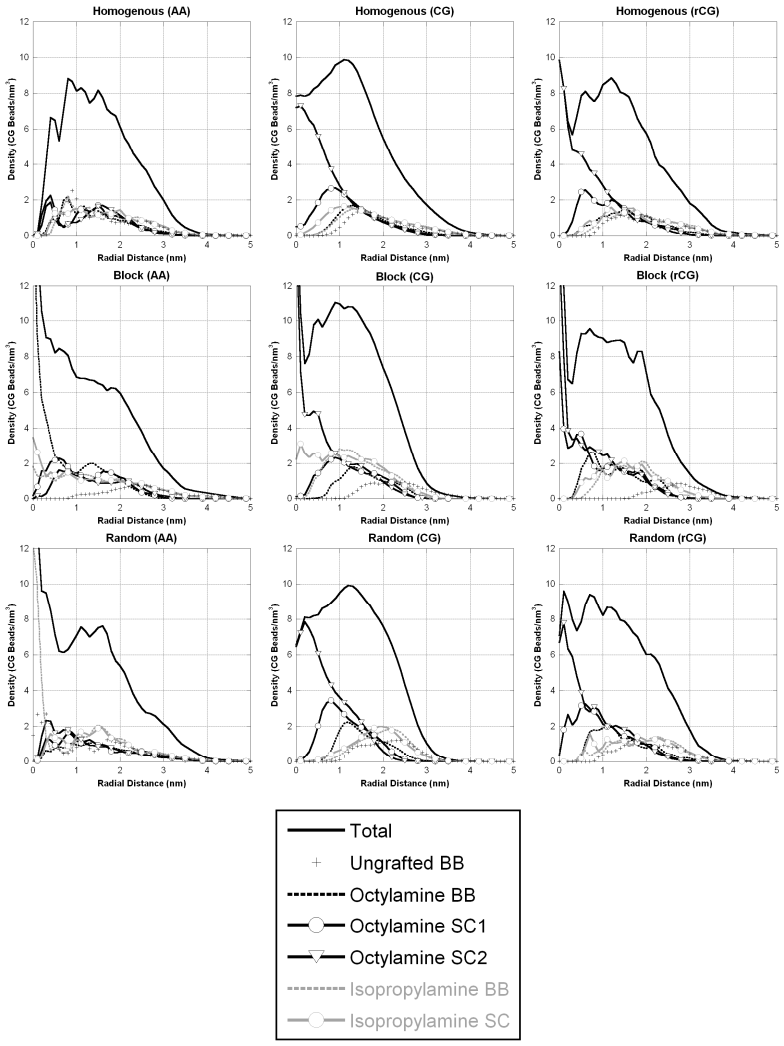

Figure 6-6 Radial Density Distributions - Component radial density distributions describe the organization of the particle contrasting the different simulation strategies.

The character of the particle interior is of great interest due to its role in stabilizing MPs. The available experimental data are ambiguous: small angle neutron scattering (SANS) of A8-35 particles containing deuterated octyl- and isopropylamine side chains have suggested the existence of a hydrophobic core, but the data collected on unlabeled A8-35 were inconclusive, possibly because of insufficient contrast [310, 318]. The particles we observe in the AAMD and rCG simulations have very different particle cores, as demonstrated in Figure 6-7, which shows the number of water molecules within 0.5 nm of the center of mass. The AAMD simulations have a core that is to a surprising

degree, permeable to water. In particular, in the AAMD simulation of the Homogeneous sequence there is a near bulk density of water at the particle center. This feature appears to be reversible, with the Block and Random sequences showing a water permeated core in various periods of simulation time, whereas at other times, there is substantially less water penetration. These fluctuations occur on the timescale of nanoseconds to tens of nanoseconds, suggesting that the duration of our simulations is appropriate for studying this feature. In contrast to these AAMD simulations, in the rCG simulations there is practically no water in the particle center, as these particles form hydrophobic, water excluding domains. If the results of the rCG simulations are any guidance, it seems plausible that APols can effectively shield the transmembrane surface of MPs from contact with water.

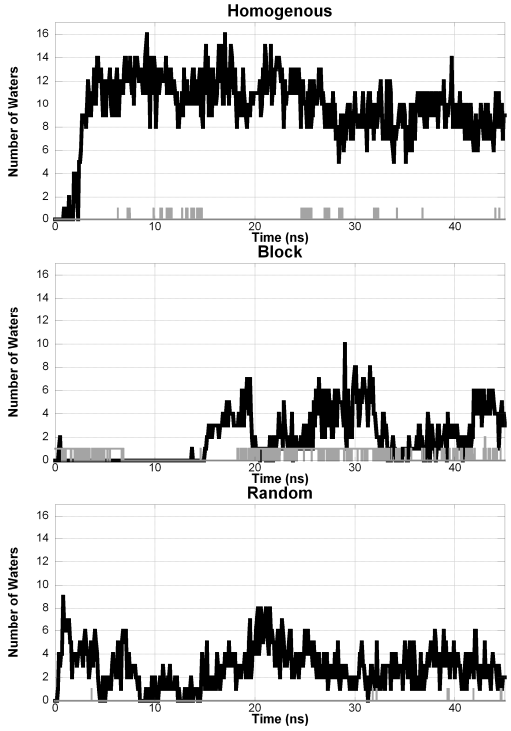

Figure 6-7 Water Permeability - Water within 0.5 nm of amphipol center of mass (AAMD = black, rCG = gray).

A common way of describing the structure of polymer particles is through their radius of gyration (R_g). Figure Figure 6-8 presents the particle Rg over the simulation time for all three sets of simulations. SANS studies of experimental A8-35 samples,

which are comprised of an ensemble of sequences, concluded that A8-35 particles have an average R_g of 2.4 ± 0.2 nm [318]. The AAMD simulations are on the larger side of this range, with the Block (2.59 nm) and Random (2.60 nm) particles being slightly larger than the Homogeneous particle (2.44 nm). For the CGMD model, the three separate simulations for each sequence give very similar results and we chose to treat the separate simulations as independent samples, allowing us to include a standard error on our estimate of R_g. Compared to the AAMD simulations, in the CGMD simulations the particles in general are smaller, with, in this case, the Homogeneous particles (2.44 ± 0.04 nm) being larger than the Block (2.15 ± 0.04 nm) or Random (2.16 ± 0.01 nm) particles. This pattern is consistent for the rCG simulations, which relax over the course of the trajectory to slightly larger values than the CGMD simulations, with the Homogeneous particles (2.49 nm) being larger than the Block (2.34 nm) or Random (2.32 nm) particles. The R_g obtained from the AAMD and rCG Random particles, which we hypothesize best represent the actual sequence distribution in A8-35 samples, is within experimental error from that determined by SANS [318].

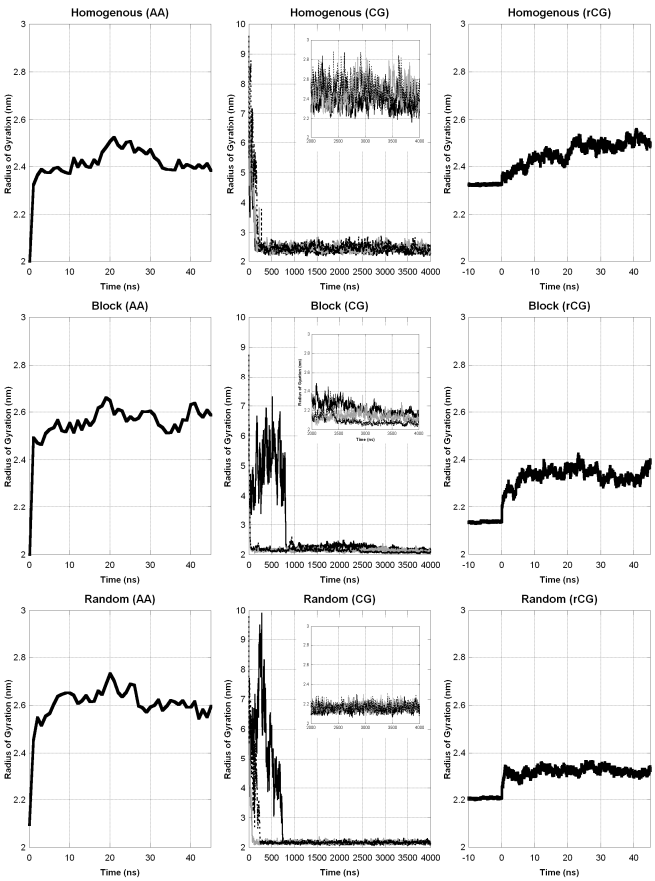

Figure 6-8 Radii of Gyration - Radii of gyration over time, describing structural relaxation and contrasting the different simulation strategies.

To describe the shape of A8-35 particles, we present the axial ratios of semi-ellipses calculated from the particle moments of inertia in Figure 6-9 (see Eq 6-10). For this parameter, a value of 1 would indicate a sphere, while larger values indicate a more elongated structure. SANS data suggest that the average A8-35 particle is nearly spherical, with axial ratios expected to be <2 (ref [318]). This is in agreement with all of the simulations, except the CGMD simulation of the Homogeneous sequence. Note that the shape of the particle is related to the R_g, a more extended particle having a larger R_g than a spherical particle. Indeed, the CGMD simulation of the Homogeneous sequence yields the most extended particles, whose R_g is significantly larger than the other CGMD simulations.

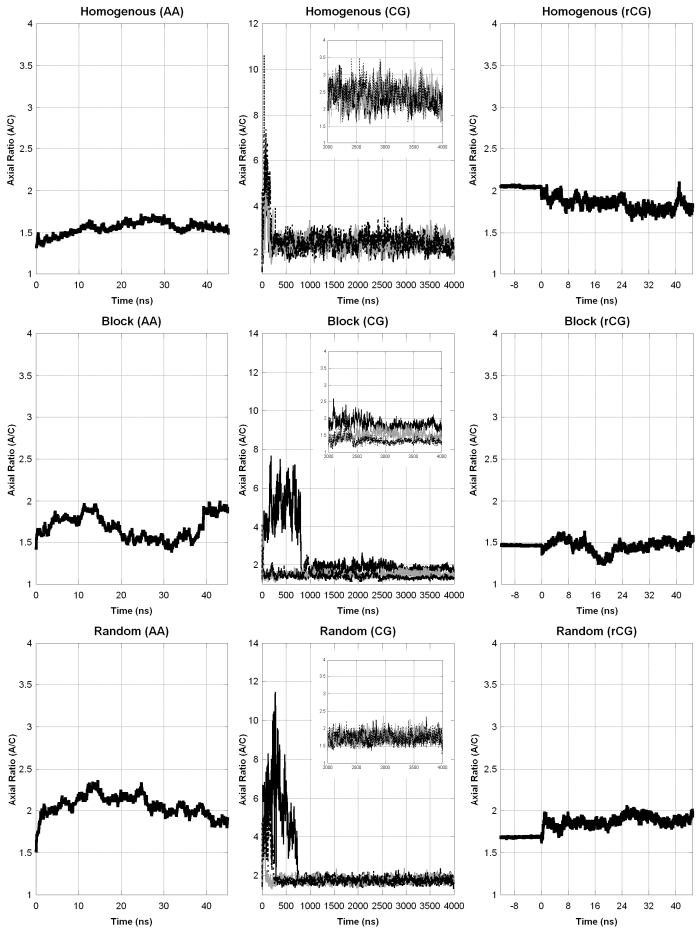

Figure 6-9 Particle Shape - Particle shape is described by fitting the structure to an ellipsoid and calculating the semiaxis ratios (*a/c*), with 1 being a spherical particle and larger values indicating elongation.

In Figure 6-10 we compare SANS profiles calculated from simulation with experimental data [318]. Note that the experimental data are the same in each panel and come from scattering on an ensemble of polymer lengths and grafting sequences. The region of interest for particles of this size is $0.0015 < Q^2 < 0.0055$ Å^{-2}, while the excess scattering at lower angle is due to a tiny fraction of larger aggregates [318], which are not present in the simulations. The relevant feature of these profiles is the slope, which according to the Guinier relation, is linear and related to the R_g of the particles (Eq 6-9). For each of the three sequences, the SANS calculated from the AAMD and rCG simulations matches the experimental data fairly well in this region, with the slopes having a percent error of <15% in all cases.

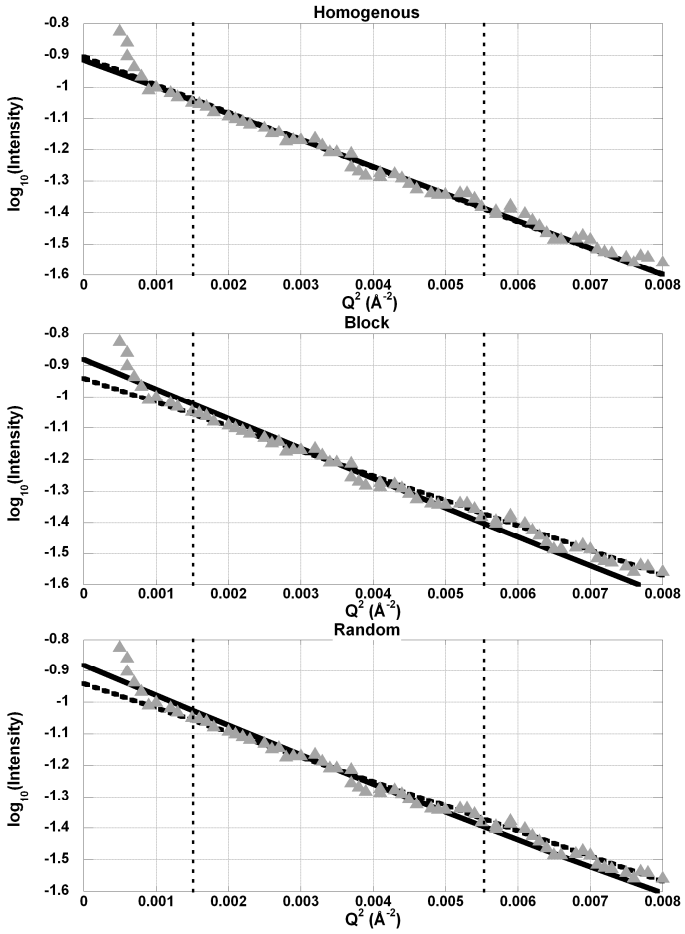

Figure 6-10 SANS Comparison - SANS from experimental ensemble (gray triangles) [Gohon et al. 2006], AAMD simulations (solid), and rCG simulation (dotted). The vertical dotted lines indicate the Guinier region, in which the linear slope of these profiles can be used to find the radius of gyration.

While comparison with the SANS data shows that MD models are compatible with existing experimental evidence, it does not allow us to differentiate between the different simulation strategies. The three sequences and two methods provide us with particles featuring a range of component segregation, water content, R_g, and shape (or *a/c* axial ratio), as characterized in Figures 6-6- 6-9. For example, the AAMD Homogeneous particle has minimal component segregation and a high internal water content, while the rCG Homogenous particle has a larger degree of segregation and almost no internal water content. However, as shown in Figure 6-10, their calculated SANS profiles are indistinguishable, with the slopes differing by only ~3%. Indeed, the structural information obtained in this region of q-space is on the nanometer scale, and is thus

sensitive to the overall particle size, but not to the higher resolution features MD simulations can access. Therefore, we use this experimental data to demonstrate that all of our particles are of the appropriate size, without suggesting differences in agreement due to other observed structural features.

Previous work has led to the hypothesis that the dynamics of the sarcoplasmic reticulum Ca^{2+}-ATPase (SERCA1a) may be damped when the protein is trapped in APols, relative to lipid bilayers or detergent micelles, suggesting that protein experiences a more viscous environment [310, 312, 335, 336]. Figure 6-11 presents the average mean squared displacement (MSD) for the AAMD and rCG A8-35 particles, as well as an all-atom POPC lipid bilayer and an all-atom SDS detergent micelle (with additional details regarding the latter simulations available elsewhere [129, 143]). Figure 6-11A shows the MSD for peripheral atoms, specifically the APol backbone α-carbons, the POPC ester oxygens, and the SDS sulfurs. Figure 6-11B shows the MSD for the terminal methyl carbons from the APol octylamine grafts, the POPC palmitoyl chains, and the SDS hydrocarbon chains. The central conclusion is that the MSDs are lower in APols as compared to the lipid bilayer and detergent micelle. In both the hydrophobic molecular core and molecular periphery, the SDS molecule is the most dynamic, the POPC is intermediate, and the amphipol is the most restrained. These results suggest that APols provide the transmembrane domain with an environment that is indeed more viscous than those of lipid bilayers or detergent micelles, a difference consistent with current hypotheses about their effect on MP dynamics [310, 312, 335, 336].

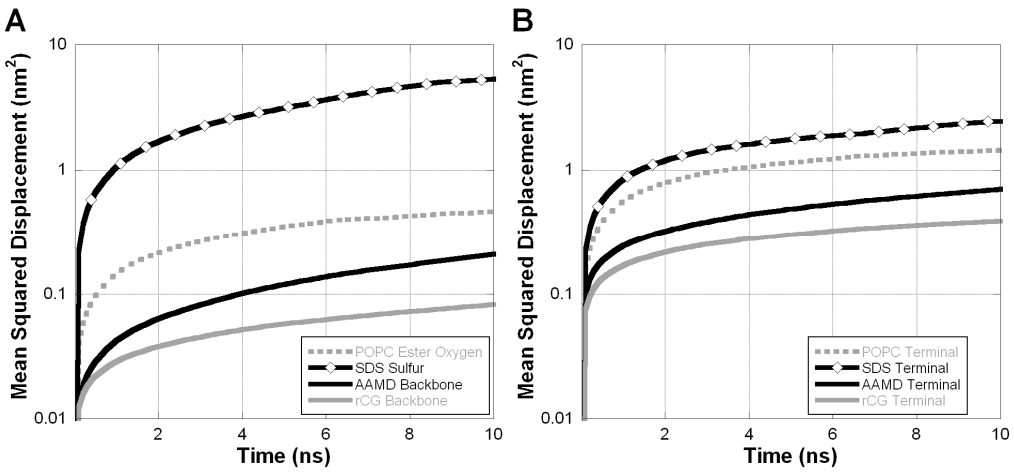

Figure 6-11 Intra-Particle Dynamics - Mean squared displacement from amphipol simulations (AAMD and rCG) compared with POPC lipid bilayer and SDS detergent micelle, for peripheral atoms (A) and hydrocarbon chain terminals (B).

6.4 Discussion

The existence of numerous potential applications of APols for the stabilization and study of solubilized MPs has prompted a series of structural investigations of both APol particles and MP/APol complexes, using such experimental approaches as radiation scattering, analytical ultracentrifugation, size exclusion chromatography, and NMR (reviewed in ref [312]). While these experimental studies have been insightful, they provide no information about the organization and dynamics of MP/APols complexes at the atomistic resolution. Here, we have taken the first steps towards this goal, by developing parameters for AAMD and CGMD simulation of APol A8-35 and characterizing the structure and dynamics of the self-assembled A8-35 particles.

Simulations of polymers could be considered a more challenging task than simulations of other macromolecules. For proteins, oligonucleotides, and most small molecules, the structure can be experimentally 'solved,' providing a well-defined set of atomic coordinates as a representative, equilibrium structure. However, for polymers, there is only minimal evidence to inform a starting configuration that is representative of the ensemble average. Given the limitations in computational power, AAMD simulations are generally restricted to durations of a few tens of nanoseconds. It is therefore not possible to obtain an equilibrated oligomeric structure starting from an unbiased initial

configuration consisting of isolated polymer chains. While our AAMD simulations have clearly relaxed to a structure that is stable on the nanosecond timescale, the limited sampling available to AAMD inspired our decision to use a lower-resolution technique, CGMD, in order to obtain structures unbiased by our design. These CGMD simulations showed a clearly different organization, which we characterized at the AAMD resolution using a set of rCG simulations. The differences in structure between the original AAMD simulations and the rCG simulations strongly suggests that the AAMD simulations had not reached equilibrium.

A particularly intriguing feature that we have characterized here is the degree of segregation of the various groups that comprise the polymer and the character of the particle core. Aggregation of A8-35 into well-defined particles is thought to result from the octylamine chains segregating from water to form a hydrophobic core – as in the formation of detergent micelles - which intuitively agrees with the efficiency of APols at stabilizing MPs in aqueous solution. However, experimental evidence in favor of the formation of such a core has remained limited [310, 318]. In our initial AAMD simulations, we find that relatively brief simulations starting from an arbitrary configuration settle into a state which is stable on the nanosecond timescale, in which the various groups are only partially segregated and which contains a substantial amount of internal water. These observations suggested that sampling was insufficient. Indeed, our much longer CGMD simulations consistently converge to a state with a well-defined hydrophobic core, which, according to rCG simulations, entirely excludes water.

Experimental batches of A8-35 are comprised of a highly polydisperse mixture of chains of various lengths and random graft sequences [309]. In these simulations we have considered the impact of grafting sequence on the structure of the particles. The Homogeneous and Block sequences were chosen to explore the ability of these polymers to form hydrophobic clusters. All sequences, including the Block sequence, consistently show some degree of hydrophobic – hydrophilic segregation, even in the initial, brief AAMD simulations. However, given the relatively low computational cost of running CGMD simulations, we can broaden our study of the relationship between sequence and structure. Figure 6-12 presents the results from a “high-throughput” set of simulations,

where 97 randomly generated sequences were run. Using this larger number of randomly generated sequences, we attempted to establish a relationship between grafting sequence and particle structure. To quantify the distribution of octylamines within a sequence, we define an Octyl Density Index, which is the maximal number of octylamine grafted units within any 10 sequential positions (though the results are consistent for a range of lengths). Using this parameter, the Homogeneous sequence has a value of 4, the Block sequence a value of 10, and the original Random sequence a value of 6. In Figure 6-12B, the particle *a/c* axial ratio is plotted as a function of the Octyl Density Index. These new simulations, in combination with the sequences already characterized, suggest that polymers with a more even distribution of octylamines tend to form particles with a more extended shape. Given this effect, we cannot exclude the possibility that the structure and functionality of the MP/APol complexes depend on the polymer sequence. Indeed, recent light scattering and electron microscopy studies point to a difference in size between random and block particles for a polymer analogous to A8-35 [365].

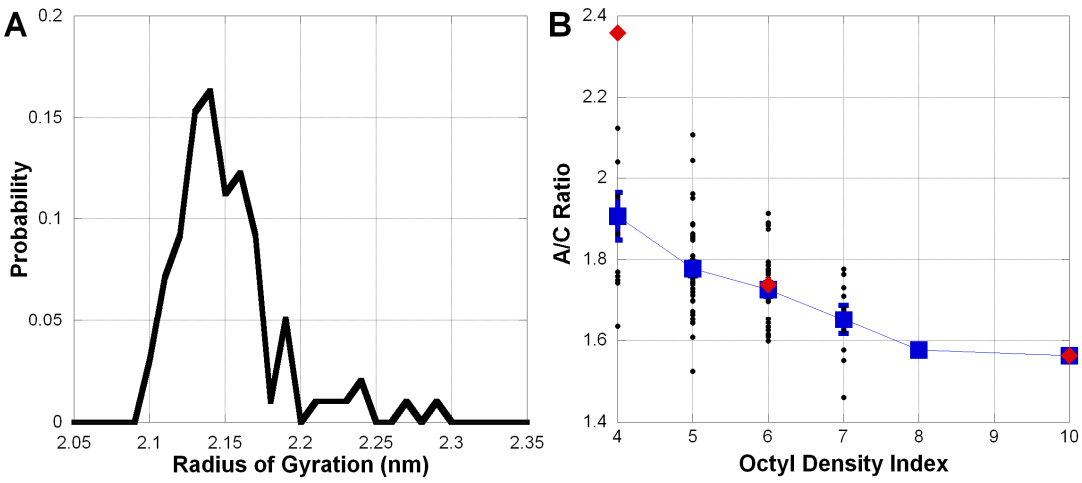

Figure 6-12 "High-Throughput" Simulations - A) Histogram of radii of gyration from 97 CGMD simulations using randomly generated sequences. B) These simulations suggest a relationship between particle shape (quantified by the a/c semiaxial ratio) and sequence.

Similarly, we have used a series of CGMD simulations to examine the effect of polymer chain length on particle structure. SANS and AUC data indicate that the average A8-35 particle has a mass of ~40 kDa (ref. [318]). According to original standard-based

estimates [309, 319] of the average mass of A8-35 molecules, namely 9-10 kDa, this would correspond to an average of ~4 molecules per particle. More recent, standard-independent mass determinations suggest however that the average mass of individual A8-35 molecules more likely lies in the 4-5 kDa range (F.Giusti & J. Rieger, unpublished observations), in which case the average particle would comprise 8-10 chains. It is therefore useful to note that particles composed of chains either twice as long or half as long as those used in the main analysis, as well as unimolecular particles, present similar R_g and *a/c* axial ratios. This is consistent with early experimental data indicating that chains that are, on average, either ~4× longer [309] or 2× shorter [366] than those of A8-35 appear as efficient as it is at keeping MPs water soluble. On the contrary, CGMD particles composed of many (16 or more) much shorter chains are considerably more ellipsoid, suggesting that large excursions from the average chain length of A8-35 may entail differences in the structure and function of MP/APol complexes. Looking ahead to future work, we consider CGMD to offer two complementary paths to understanding the structure of APol particles and MP/APol complexes: 1) CGMD can generate structures for AA-resolution rCG simulations and, 2) CGMD can explore a structural relationship using a large number of simulations at a lower resolution.

A particularly valuable property of APols is their mildness towards MPs, whose stability is, a rule, considerably improved over that in detergent (see *e.g.* [309, 312, 314, 317, 336]). This property has been tentatively traced to three mechanisms (for a more extended discussion, see [312]). First, the use of APols makes it possible to reduce the amount of free surfactant, which acts as a hydrophobic sink into which stabilizing lipids, cofactors and subunits can diffuse away. Second, APols are intrinsically less dissociating than detergents, because they compete less efficiently with the protein-protein and protein-lipid interactions that stabilize the 3D structure of MPs. The third, hypothetical effect has been dubbed the 'Gulliver effect'. Based primarily on observations carried out on the sarcoplasmic calcium ATPase (SERCA1a), it postulates that APols do not interfere much with small-scale movements at the transmembrane surface of MPs [317, 367], but slow down larger-scale movements, such as those involved in the enzymatic cycle of SERCA1a [335, 336] or in MP denaturation [310, 312, 335]. This hypothesis is supported by the present analysis

of the dynamics of A8-35 particles, which shows that movements that cannot be accommodated by the rearrangement of octyl chains will be hampered by the much less dynamic APol backbone, whose viscosity is higher than that of the polar head region of a detergent micelle, or even a lipid bilayer.

It is interesting to speculate on how the organization of a MP-adsorbed APol layer may differ from that of the free APol particle. On the one hand, the hydrophobic transmembrane surface of the protein may drive the clustering of octylamine chains around it, creating a layer that could be even more hydrophobic than that of the core of free APol particles. On the other hand, it is possible that the layer immediately in contact with the protein transmembrane surface be not exclusively hydrophobic, as suggested by NMR data on the interaction between A8-35 and the transmembrane β-barrel of *Escherichia coli*'s OmpA: while it was found that one face of the barrel strongly interacts with the octylamine and/or isopropylamine grafts, the other face showed less dense interactions with the hydrophobic polymer side chains [324]. This type of question can be readily addressed by MD, using the parameters and simulation strategy we have presented here.

6.5 Simulation of an Amphipol–Membrane Protein Complex

The motivation for parametrizing the amphipol polymer, as discussed in Chapter 6 is to perform structural characterization of the amphipol – membrane protein complex. A specific hypothesis that we will seek to address is that protein dynamics are dampened by A8-35 solubilization. This hypothesis was proposed based on experimental investigation of the sarcoplasmic reticulum Ca^{2+}-ATPase (SERCA1a), which showed that release of calcium from the transmembrane domain, a step in SERCA1a's enzymatic cycle, was slower when the protein was solubilized in A8-35 relative to a detergent micelle [335]. Since the release of calcium is accompanied by a conformational change, it was suggested that the amphipol environment dampened the protein dynamics, slowing the rate at which this step occurs.

We have begun to investigate the relative dynamics of membrane proteins stabilized by amhpipols, detergent micelles, and lipid bilayers. While observations of SERCA1a inspired this hypothesis, it is a larger protein (~110 kDa). Instead, we chose to begin with a simpler model protein, the transmembrane domain of bacteriorhodopsin (BR ~25 kDa). The structure of the Amphipol – BR complex has been recently characterized, providing useful information (such as the ratio of amphipol : BR found in the complex) and perhaps data that can be used for experimental verification (e.g. SANS) [317]. Below are preliminary snapshots illustrating the Amphipol – BR complex which forms after 5 microseconds of simulation (Figure 6-13). In particular, note that polymer has a specific organization, with the hydrophobic octylamine grafts surrounding the hydrophobic transmembrane domain (Figure 6-13B).

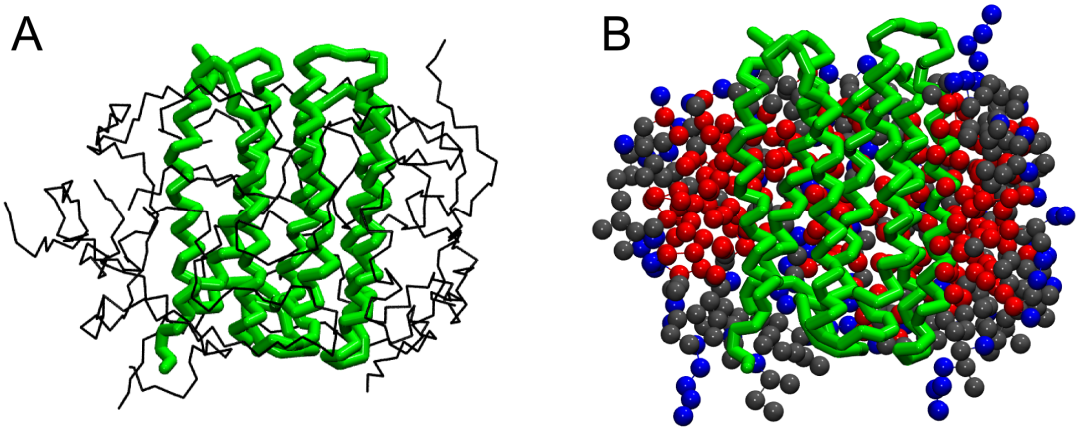

Figure 6-13 Snapshots of Amphipol – BR complex – Representations emphasizing polymer backbone (A) and particle organization (B). Green = Protein, Red = octylamine grafted units, Gray = Isopropylamine grafted units, Blue = Ungrafted units.

A second set of simulations will investigate the interaction between the amphipol and lipid bilayers. There is some evidence that amphipols can be used to deliver membrane proteins to a membrane [308]. There is also evidence that at high concentrations amphipols can deform lipid bilayers [368, 369]. Therefore, in order to build towards simulations of greater complexity, containg polymer, protein, and lipid, we are investigating the interaction between amphipols and lipid bilayers. Figure 6-14 presents snapshots showing the insertion and clustering of the hydrophobic octylamine grafts on the surface of a bilayer.

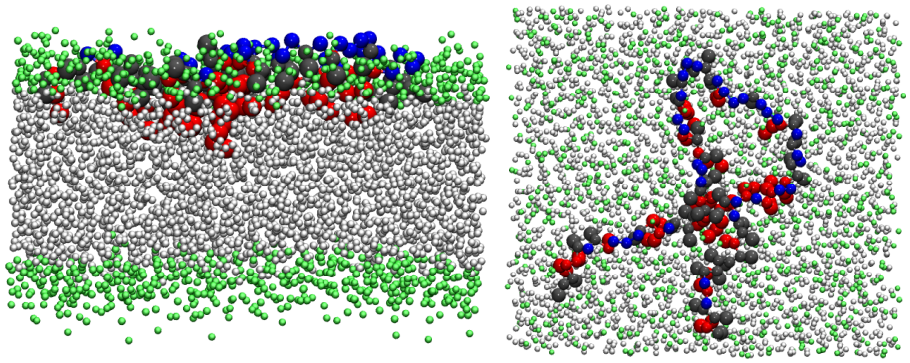

Figure 6-14 Snapshots of Amphipol – Bilayer Interaction – Side and Top views of amphipol lipid bilayer interaction. Green = lipid headgroup, White = lipid chains, Red = octylamine grafted units, Gray = Isopropylamine grafted units, Blue = Ungrafted units.

IV Conclusion

The over-arching subject of this thesis is the structure of membranes and the effects of membrane structure on membrane proteins. Section I presents our efforts to characterize the structure of lipid bilayers, focusing on experimental verification through X-ray Scattering (Chapter 2), the effect of cholesterol structure on domain formation/inhibition (Chapter 3), and the structural effects due to interleaflet coupling (Chapter 4). Major results include an orientation dependent mechanism for steroid domain promotion and inhibition (Chapter 3), a dependency of domain organization on hydrophobic mismatch (section 4.2.2), and an interleaflet induction in order and curvature in bilayers containing phase asymmetry (section 4.2.3).

In Section II, the effect of membrane and membrane-mimetic structure on the protein α-Synuclein is investigated, suggesting ways in which α-Synuclein might adapt to its environment. In particular, membrane curvature is found to be important, with the highly curved detergent micelle inducing changes in protein structure. For example, a specific region within the protein was identified as a bending point, allowing the protein to adapt to the curvature of its environment.

Section III presents an investigation into the structure of a membrane-mimetic amphipathic polymer. Given the sensitivity of membrane proteins to the membrane environment, such as to differences in thickness, it is important to consider the role of membrane-mimetic structure on membrane protein behavior. While membrane-mimetics are commonly used as an experimental proxy to stabilize membranes proteins in solution, there is growing evidence that they can have a distinct effect on membrane protein structure, thus perhaps undermining their use. In Sections II and III, the effects of membrane-mimetics are considered in order to determine how their environments might exert a distinct effect.

Collectively, these simulations expand upon our understanding of membranes and membrane proteins, describing structural features which may have important functional repercussions. The relatively simple models presented in this thesis offer insight into the fundamental features which may be essential for the understanding the structure and function of complex biological mixtures.

V References

(1) van Meer, G.; Voelker, D. R.; Feigenson, G. W. *Nat Rev Mol Cell Biol* **2008,** *9*, 112-24
(2) Bretscher, M. S.; Munro, S. *Science* **1993,** *261*, 1280-1
(3) Levine, T. P.; Wiggins, C. A.; Munro, S. *Mol Biol Cell* **2000,** *11*, 2267-81
(4) Cotter, D.; Maer, A.; Guda, C.; Saunders, B.; Subramaniam, S. *Nucleic Acids Res* **2006,** *34*, D507-10
(5) Sud, M.; Fahy, E.; Cotter, D.; Brown, A.; Dennis, E. A.; Glass, C. K.; Merrill, A. H., Jr.; Murphy, R. C.; Raetz, C. R.; Russell, D. W.; Subramaniam, S. *Nucleic Acids Res* **2007,** *35*, D527-32
(6) Lewis, B. A.; Engelman, D. M. *J Mol Biol* **1983,** *166*, 211-7
(7) Rawicz, W.; Olbrich, K. C.; McIntosh, T.; Needham, D.; Evans, E. *Biophys J* **2000,** *79*, 328-39
(8) Sugii, T.; Takagi, S.; Matsumoto, Y. *J Chem Phys* **2005,** *123*, 184714
(9) Levy, Y.; Onuchic, J. N. *Annu Rev Biophys Biomol Struct* **2006,** *35*, 389-415
(10) McIntosh, T. J.; Simon, S. A. *Annu Rev Biophys Biomol Struct* **2006,** *35*, 177-98
(11) Andersen, O. S.; Koeppe, R. E., 2nd *Annu Rev Biophys Biomol Struct* **2007,** *36*, 107-30
(12) Lee, A. G. *Biochim Biophys Acta* **2004,** *1666*, 62-87
(13) Engelman, D. M. *Nature* **2005,** *438*, 578-80
(14) Takamori, S.; Holt, M.; Stenius, K.; Lemke, E. A.; Gronborg, M.; Riedel, D.; Urlaub, H.; Schenck, S.; Brugger, B.; Ringler, P.; Muller, S. A.; Rammner, B.; Grater, F.; Hub, J. S.; De Groot, B. L.; Mieskes, G.; Moriyama, Y.; Klingauf, J.; Grubmuller, H.; Heuser, J.; Wieland, F.; Jahn, R. *Cell* **2006,** *127*, 831-46
(15) Berkowitz, M. L. *Biochim Biophys Acta* **2009,** *1788*, 86-96
(16) Marrink, S. J.; de Vries, A. H.; Tieleman, D. P. *Biochim Biophys Acta* **2009,** *1788*, 149-68
(17) Lindahl, E.; Sansom, M. S. *Curr Opin Struct Biol* **2008,** *18*, 425-31
(18) Hansson, T.; Oostenbrink, C.; van Gunsteren, W. *Curr Opin Struct Biol* **2002,** *12*, 190-6
(19) Karplus, M.; McCammon, J. A. *Nat Struct Biol* **2002,** *9*, 646-52
(20) Killian, J. A. *Biochim Biophys Acta* **1998,** *1376*, 401-15
(21) Mouritsen, O. G.; Bloom, M. *Biophys J* **1984,** *46*, 141-53
(22) Sharpe, H. J.; Stevens, T. J.; Munro, S. *Cell* **2010,** *142*, 158-69
(23) Periole, X.; Huber, T.; Marrink, S. J.; Sakmar, T. P. *J Am Chem Soc* **2007,** *129*, 10126-32
(24) Karlovska, J.; Uhrikova, D.; Kucerka, N.; Teixeira, J.; Devinsky, F.; Lacko, I.; Balgavy, P. *Biophys Chem* **2006,** *119*, 69-77
(25) Faller, R.; Marrink, S. J. *Langmuir* **2004,** *20*, 7686-93
(26) Mabrey, S.; Sturtevant, J. M. *Proc Natl Acad Sci U S A* **1976,** *73*, 3862-6
(27) London, E. *Curr Opin Struct Biol* **2002,** *12*, 480-6
(28) de Almeida, R. F.; Fedorov, A.; Prieto, M. *Biophys J* **2003,** *85*, 2406-16
(29) Feigenson, G. W. *Biochim Biophys Acta* **2009,** *1788*, 47-52

(30) Goni, F. M.; Alonso, A.; Bagatolli, L. A.; Brown, R. E.; Marsh, D.; Prieto, M.; Thewalt, J. L. *Biochim Biophys Acta* **2008,** *1781*, 665-84
(31) Veatch, S. L.; Keller, S. L. *Biophys J* **2003,** *85*, 3074-83
(32) Zhao, J.; Wu, J.; Heberle, F. A.; Mills, T. T.; Klawitter, P.; Huang, G.; Costanza, G.; Feigenson, G. W. *Biochim Biophys Acta* **2007,** *1768*, 2764-76
(33) Silvius, J. R. *Biochim Biophys Acta* **2003,** *1610*, 174-83
(34) Simons, K.; Vaz, W. L. *Annu Rev Biophys Biomol Struct* **2004,** *33*, 269-95
(35) Huang, J.; Feigenson, G. W. *Biophys J* **1999,** *76*, 2142-57
(36) Kucerka, N.; Perlmutter, J. D.; Pan, J.; Tristram-Nagle, S.; Katsaras, J.; Sachs, J. N. *Biophys J* **2008,** *95*, 2792-805
(37) McConnell, H. M.; Radhakrishnan, A. *Biochim Biophys Acta* **2003,** *1610*, 159-73
(38) McConnell, H. M.; Vrljic, M. *Annu Rev Biophys Biomol Struct* **2003,** *32*, 469-92
(39) Sankaram, M. B.; Thompson, T. E. *Proc Natl Acad Sci U S A* **1991,** *88*, 8686-90
(40) Pandit, S. A.; Jakobsson, E.; Scott, H. L. *Biophys J* **2004,** *87*, 3312-22
(41) Marrink, S. J.; de Vries, A. H.; Harroun, T. A.; Katsaras, J.; Wassall, S. R. *J Am Chem Soc* **2008,** *130*, 10-1
(42) Harroun, T. A.; Katsaras, J.; Wassall, S. R. *Biochemistry* **2008,** *47*, 7090-6
(43) Harroun, T. A.; Katsaras, J.; Wassall, S. R. *Biochemistry* **2006,** *45*, 1227-33
(44) Simons, K.; Ikonen, E. *Nature* **1997,** *387*, 569-72
(45) Singer, S. J.; Nicolson, G. L. *Science* **1972,** *175*, 720-31
(46) Hancock, J. F. *Nat Rev Mol Cell Biol* **2006,** *7*, 456-62
(47) de Almeida, R. F.; Loura, L. M.; Fedorov, A.; Prieto, M. *J Mol Biol* **2005,** *346*, 1109-20
(48) Silvius, J. R. *Biophys J* **2003,** *85*, 1034-45
(49) Feigenson, G. W.; Buboltz, J. T. *Biophys J* **2001,** *80*, 2775-88
(50) Yuan, C.; Furlong, J.; Burgos, P.; Johnston, L. J. *Biophys J* **2002,** *82*, 2526-35
(51) Veatch, S. L.; Keller, S. L. *Biochim Biophys Acta* **2005,** *1746*, 172-85
(52) Veatch, S. L.; Polozov, I. V.; Gawrisch, K.; Keller, S. L. *Biophys J* **2004,** *86*, 2910-22
(53) Lingwood, D.; Simons, K. *Science* **2009,** *327*, 46-50
(54) Hanada, K.; Nishijima, M.; Akamatsu, Y.; Pagano, R. E. *J Biol Chem* **1995,** *270*, 6254-60
(55) Ge, M.; Field, K. A.; Aneja, R.; Holowka, D.; Baird, B.; Freed, J. H. *Biophys J* **1999,** *77*, 925-33
(56) Schroeder, R.; London, E.; Brown, D. *Proc Natl Acad Sci U S A* **1994,** *91*, 12130-4
(57) London, E.; Brown, D. A. *Biochim Biophys Acta* **2000,** *1508*, 182-95
(58) Lichtenberg, D.; Goni, F. M.; Heerklotz, H. *Trends Biochem Sci* **2005,** *30*, 430-6
(59) Shogomori, H.; Brown, D. A. *Biol Chem* **2003,** *384*, 1259-63
(60) Sot, J.; Collado, M. I.; Arrondo, J. L. R.; Alonso, A.; Goni, F. M. *Langmuir* **2002,** *18*, 2828-2835
(61) Sharma, P.; Varma, R.; Sarasij, R. C.; Ira; Gousset, K.; Krishnamoorthy, G.; Rao, M.; Mayor, S. *Cell* **2004,** *116*, 577-89
(62) Goswami, D.; Gowrishankar, K.; Bilgrami, S.; Ghosh, S.; Raghupathy, R.; Chadda, R.; Vishwakarma, R.; Rao, M.; Mayor, S. *Cell* **2008,** *135*, 1085-97

(63) Suzuki, K. G.; Fujiwara, T. K.; Sanematsu, F.; Iino, R.; Edidin, M.; Kusumi, A. *J Cell Biol* **2007,** *177*, 717-30
(64) Lenne, P. F.; Wawrezinieck, L.; Conchonaud, F.; Wurtz, O.; Boned, A.; Guo, X. J.; Rigneault, H.; He, H. T.; Marguet, D. *Embo J* **2006,** *25*, 3245-56
(65) Plowman, S. J.; Muncke, C.; Parton, R. G.; Hancock, J. F. *Proc Natl Acad Sci U S A* **2005,** *102*, 15500-5
(66) Eggeling, C.; Ringemann, C.; Medda, R.; Schwarzmann, G.; Sandhoff, K.; Polyakova, S.; Belov, V. N.; Hein, B.; von Middendorff, C.; Schonle, A.; Hell, S. W. *Nature* **2009,** *457*, 1159-62
(67) Swamy, M. J.; Ciani, L.; Ge, M.; Smith, A. K.; Holowka, D.; Baird, B.; Freed, J. H. *Biophys J* **2006,** *90*, 4452-65
(68) Dietrich, C.; Volovyk, Z. N.; Levi, M.; Thompson, N. L.; Jacobson, K. *Proc Natl Acad Sci U S A* **2001,** *98*, 10642-7
(69) Kahya, N.; Brown, D. A.; Schwille, P. *Biochemistry* **2005,** *44*, 7479-7489
(70) Giocondi, M. C.; Seantier, B.; Dosset, P.; Milhiet, P. E.; Le Grimellec, C. *Pflugers Arch* **2008,** *456*, 179-88
(71) Sengupta, P.; Hammond, A.; Holowka, D.; Baird, B. *Biochim Biophys Acta* **2008,** *1778*, 20-32
(72) Brown, D. A.; London, E. *J Biol Chem* **2000,** *275*, 17221-4
(73) Brown, D. A.; Rose, J. K. *Cell* **1992,** *68*, 533-44
(74) Rossin, A.; Derouet, M.; Abdel-Sater, F.; Hueber, A. O. *Biochem J* **2009,** *419*, 185-92, 2 p following 192
(75) Barnes, N. C.; Powell, M. S.; Trist, H. M.; Gavin, A. L.; Wines, B. D.; Hogarth, P. M. *Immunol Lett* **2006,** *104*, 118-23
(76) Bhattacharya, J.; Peters, P. J.; Clapham, P. R. *J Virol* **2004,** *78*, 5500-6
(77) Chen, B. J.; Takeda, M.; Lamb, R. A. *J Virol* **2005,** *79*, 13673-84
(78) Levental, I.; Lingwood, D.; Grzybek, M.; Coskun, U.; Simons, K. *Proc Natl Acad Sci U S A* **2010,** *107*, 22050-4
(79) Morel, J.; Claverol, S.; Mongrand, S.; Furt, F.; Fromentin, J.; Bessoule, J. J.; Blein, J. P.; Simon-Plas, F. *Mol Cell Proteomics* **2006,** *5*, 1396-411
(80) Gosse, J. A.; Wagenknecht-Wiesner, A.; Holowka, D.; Baird, B. *J Immunol* **2005,** *175*, 2123-31
(81) Garcia-Garcia, E.; Brown, E. J.; Rosales, C. *J Immunol* **2007,** *178*, 3048-58
(82) Takeda, M.; Leser, G. P.; Russell, C. J.; Lamb, R. A. *Proc Natl Acad Sci U S A* **2003,** *100*, 14610-7
(83) Scheiffele, P.; Roth, M. G.; Simons, K. *Embo J* **1997,** *16*, 5501-8
(84) Barman, S.; Adhikary, L.; Chakrabarti, A. K.; Bernas, C.; Kawaoka, Y.; Nayak, D. P. *J Virol* **2004,** *78*, 5258-69
(85) Kundu, A.; Avalos, R. T.; Sanderson, C. M.; Nayak, D. P. *J Virol* **1996,** *70*, 6508-15
(86) Cho, N. H.; Kingston, D.; Chang, H.; Kwon, E. K.; Kim, J. M.; Lee, J. H.; Chu, H.; Choi, M. S.; Kim, I. S.; Jung, J. U. *J Virol* **2006,** *80*, 108-18
(87) Min, C. K.; Bang, S. Y.; Cho, B. A.; Choi, Y. H.; Yang, J. S.; Lee, S. H.; Seong, S. Y.; Kim, K. W.; Kim, S.; Jung, J. U.; Choi, M. S.; Kim, I. S.; Cho, N. H. *PLoS Pathog* **2008,** *4*, e1000209

(88) Schafer, L. V.; de Jong, D. H.; Holt, A.; Rzepiela, A. J.; de Vries, A. H.; Poolman, B.; Killian, J. A.; Marrink, S. J. *Proc Natl Acad Sci U S A* **2011,** *108*, 1343-8
(89) van Duyl, B. Y.; Rijkers, D. T.; de Kruijff, B.; Killian, J. A. *FEBS Lett* **2002,** *523*, 79-84
(90) McIntosh, T. J.; Vidal, A.; Simon, S. A. *Biophys J* **2003,** *85*, 1656-66
(91) Vidal, A.; McIntosh, T. J. *Biophys J* **2005,** *89*, 1102-8
(92) Samsonov, A. V.; Mihalyov, I.; Cohen, F. S. *Biophys J* **2001,** *81*, 1486-500
(93) Korlach, J.; Schwille, P.; Webb, W. W.; Feigenson, G. W. *Proc Natl Acad Sci U S A* **1999,** *96*, 8461-6
(94) Dietrich, C.; Bagatolli, L. A.; Volovyk, Z. N.; Thompson, N. L.; Levi, M.; Jacobson, K.; Gratton, E. *Biophys J* **2001,** *80*, 1417-28
(95) Garg, S.; Ruhe, J.; Ludtke, K.; Jordan, R.; Naumann, C. A. *Biophys J* **2007,** *92*, 1263-70
(96) Stottrup, B. L.; Veatch, S. L.; Keller, S. L. *Biophys J* **2004,** *86*, 2942-50
(97) Crane, J. M.; Kiessling, V.; Tamm, L. K. *Langmuir* **2005,** *21*, 1377-88
(98) Rinia, H. A.; Snel, M. M.; van der Eerden, J. P.; de Kruijff, B. *FEBS Lett* **2001,** *501*, 92-6
(99) Op den Kamp, J. A. *Annu Rev Biochem* **1979,** *48*, 47-71
(100) Devaux, P. F.; Morris, R. *Traffic* **2004,** *5*, 241-6
(101) Bretscher, M. S. *Nat New Biol* **1972,** *236*, 11-2
(102) McIntosh, T. J. *Biophys J* **2003,** *85*, 1675-81
(103) Schroeder, F.; Nemecz, G.; Wood, W. G.; Joiner, C.; Morrot, G.; Ayraut-Jarrier, M.; Devaux, P. F. *Biochim Biophys Acta* **1991,** *1066*, 183-92
(104) Edidin, M. *Annu Rev Biophys Biomol Struct* **2003,** *32*, 257-83
(105) Kiessling, V.; Wan, C.; Tamm, L. K. *Biochim Biophys Acta* **2009,** *1788*, 64-71
(106) Wang, T. Y.; Silvius, J. R. *Biophys J* **2001,** *81*, 2762-73
(107) Collins, M. D.; Keller, S. L. *Proc Natl Acad Sci U S A* **2008,** *105*, 124-8
(108) Kiessling, V.; Crane, J. M.; Tamm, L. K. *Biophys J* **2006,** *91*, 3313-26
(109) Wan, C.; Kiessling, V.; Tamm, L. K. *Biochemistry* **2008,** *47*, 2190-8
(110) Cheng, H. T.; Megha; London, E. *J Biol Chem* **2009,** *284*, 6079-92
(111) Chiantia, S.; Schwille, P.; Klymchenko, A. S.; London, E. *Biophys J* **2011,** *100*, L1-3
(112) Parthasarathy, R.; Groves, J. T. *Soft Matter* **2007,** *3*, 24-33
(113) Chernomordik, L.; Kozlov, M. M.; Zimmerberg, J. *J Membr Biol* **1995,** *146*, 1-14
(114) Ramamurthi, K. S.; Lecuyer, S.; Stone, H. A.; Losick, R. *Science* **2009,** *323*, 1354-7
(115) Ramamurthi, K. S.; Losick, R. *Proc Natl Acad Sci U S A* **2009,** *106*, 13541-5
(116) Hu, J.; Shibata, Y.; Voss, C.; Shemesh, T.; Li, Z.; Coughlin, M.; Kozlov, M. M.; Rapoport, T. A.; Prinz, W. A. *Science* **2008,** *319*, 1247-50
(117) Shibata, Y.; Hu, J.; Kozlov, M. M.; Rapoport, T. A. *Annu Rev Cell Dev Biol* **2009,** *25*, 329-54
(118) Voeltz, G. K.; Prinz, W. A.; Shibata, Y.; Rist, J. M.; Rapoport, T. A. *Cell* **2006,** *124*, 573-86
(119) Ayton, G. S.; Lyman, E.; Krishna, V.; Swenson, R. D.; Mim, C.; Unger, V. M.; Voth, G. A. *Biophys J* **2009,** *97*, 1616-25

(120) Blood, P. D.; Voth, G. A. *Proc Natl Acad Sci U S A* **2006,** *103*, 15068-72
(121) Zimmerberg, J.; Kozlov, M. M. *Nat Rev Mol Cell Biol* **2006,** *7*, 9-19
(122) Abeliovich, A.; Schmitz, Y.; Farinas, I.; Choi-Lundberg, D.; Ho, W. H.; Castillo, P. E.; Shinsky, N.; Verdugo, J. M.; Armanini, M.; Ryan, A.; Hynes, M.; Phillips, H.; Sulzer, D.; Rosenthal, A. *Neuron* **2000,** *25*, 239-52
(123) Cabin, D. E.; Shimazu, K.; Murphy, D.; Cole, N. B.; Gottschalk, W.; McIlwain, K. L.; Orrison, B.; Chen, A.; Ellis, C. E.; Paylor, R.; Lu, B.; Nussbaum, R. L. *J Neurosci* **2002,** *22*, 8797-807
(124) Murphy, D. D.; Rueter, S. M.; Trojanowski, J. Q.; Lee, V. M. *J Neurosci* **2000,** *20*, 3214-20
(125) Yavich, L.; Tanila, H.; Vepsalainen, S.; Jakala, P. *J Neurosci* **2004,** *24*, 11165-70
(126) Larsen, K. E.; Schmitz, Y.; Troyer, M. D.; Mosharov, E.; Dietrich, P.; Quazi, A. Z.; Savalle, M.; Nemani, V.; Chaudhry, F. A.; Edwards, R. H.; Stefanis, L.; Sulzer, D. *J Neurosci* **2006,** *26*, 11915-22
(127) Nuscher, B.; Kamp, F.; Mehnert, T.; Odoy, S.; Haass, C.; Kahle, P. J.; Beyer, K. *J Biol Chem* **2004,** *279*, 21966-75
(128) Kamp, F.; Beyer, K. *J Biol Chem* **2006,** *281*, 9251-9
(129) Perlmutter, J. D.; Braun, A. R.; Sachs, J. N. *J Biol Chem* **2009,** *284*, 7177-89
(130) Cross, T. A.; Sharma, M.; Yi, M.; Zhou, H. X. *Trends Biochem Sci* **2011,** *36*, 117-25
(131) Trexler, A.; Rhoades, E. *Biochemistry* **2009**,
(132) Marrink, S. J.; De Vries, A. H.; Mark, A. E. *J Phys Chem B* **2004,** *108*, 750-760
(133) Marrink, S. J.; Risselada, H. J.; Yefimov, S.; Tieleman, D. P.; de Vries, A. H. *J Phys Chem B* **2007,** *111*, 7812-24
(134) Voth, G. A., *Coarse Graining of Condensed Phase and Biomolecular Systems*. CRC Press: Boca Raton, 2008.
(135) Noid, W. G.; Chu, J. W.; Ayton, G. S.; Krishna, V.; Izvekov, S.; Voth, G. A.; Das, A.; Andersen, H. C. *J Chem Phys* **2008,** *128*, 244114
(136) Baron, R.; Trzesniak, D.; de Vries, A. H.; Elsener, A.; Marrink, S. J.; van Gunsteren, W. F. *Chemphyschem* **2007,** *8*, 452-61
(137) Stevens, M. J. *J Chem Phys* **2004,** *121*, 11942-8
(138) Shelley, J. C.; Shelley, M. Y.; Reeder, R. C.; Bandyopadhyay, S.; Klein, M. L. *J Phys Chem B* **2001,** *105*, 4464-4470
(139) Shih, A. Y.; Arkhipov, A.; Freddolino, P. L.; Schulten, K. *J Phys Chem B* **2006,** *110*, 3674-84
(140) Marrink, S. J.; Risselada, J.; Mark, A. E. *Chem Phys Lipids* **2005,** *135*, 223-44
(141) Risselada, H. J.; Mark, A. E.; Marrink, S. J. *J Phys Chem B* **2008,** *112*, 7438-47
(142) Bennett, W. F.; MacCallum, J. L.; Hinner, M. J.; Marrink, S. J.; Tieleman, D. P. *J Am Chem Soc* **2009,** *131*, 12714-20
(143) Perlmutter, J. D.; Sachs, J. N. *Biochim Biophys Acta* **2009,** *1788*, 2284-90
(144) Perlmutter, J. D.; Sachs, J. N. *J Am Chem Soc* **2009,** *131*, 16362-3
(145) Perlmutter, J. D.; Sachs, J. N. *J Am Chem Soc* **2011,** *133*, 6563-6577
(146) Nagle, J. F.; Tristram-Nagle, S. *Biochim Biophys Acta* **2000,** *1469*, 159-95
(147) Mashl, R. J.; Scott, H. L.; Subramaniam, S.; Jakobsson, E. *Biophys J* **2001,** *81*, 3005-15

(148) Hung, W. C.; Lee, M. T.; Chen, F. Y.; Huang, H. W. *Biophys J* **2007,** *92*, 3960-7
(149) Kucerka, N.; Nagle, J. F.; Sachs, J. N.; Feller, S. E.; Pencer, J.; Jackson, A.; Katsaras, J. *Biophys J* **2008,** *95*, 2356-67
(150) Epand, R. M. *Biochim Biophys Acta* **2008,** *1778*, 1576-82
(151) Mills, T. T.; Toombes, G. E.; Tristram-Nagle, S.; Smilgies, D. M.; Feigenson, G. W.; Nagle, J. F. *Biophys J* **2008,** *95*, 669-81
(152) Klauda, J. B.; Kucerka, N.; Brooks, B. R.; Pastor, R. W.; Nagle, J. F. *Biophys J* **2006,** *90*, 2796-807
(153) Sachs, J. N.; Petrache, H. I.; Woolf, T. B. *Chem Phys Lipids* **2003,** *126*, 211-23
(154) Catoire, L. J.; Zoonens, M.; van Heijenoort, C.; Giusti, F.; Guittet, E.; Popot, J. L. *Eur Biophys J* **2009**,
(155) Klein, M. L.; Shinoda, W. *Science* **2008,** *321*, 798-800
(156) Hinner, M. J.; Marrink, S. J.; de Vries, A. H. *J Phys Chem B* **2009,** *113*, 15807-19
(157) Marrink, S. J.; Mark, A. E. *J Am Chem Soc* **2003,** *125*, 15233-42
(158) Baoukina, S.; Monticelli, L.; Risselada, H. J.; Marrink, S. J.; Tieleman, D. P. *Proc Natl Acad Sci U S A* **2008,** *105*, 10803-8
(159) Lee, H.; Larson, R. G. *J Phys Chem B* **2006,** *110*, 18204-11
(160) Thogersen, L.; Schiott, B.; Vosegaard, T.; Nielsen, N. C.; Tajkhorshid, E. *Biophys J* **2008,** *95*, 4337-47
(161) Lopez, C. F.; Moore, P. B.; Shelley, J. C.; Shelley, M. Y.; Klein, M. L. *Computer Physics Communications* **2002,** *147*, 1-6
(162) Shih, A. Y.; Freddolino, P. L.; Sligar, S. G.; Schulten, K. *Nano Lett* **2007,** *7*, 1692-6
(163) Van Der Spoel, D.; Lindahl, E.; Hess, B.; Groenhof, G.; Mark, A. E.; Berendsen, H. J. *J Comput Chem* **2005,** *26*, 1701-18
(164) Silvius, J. R., Thermotropic Phase Transitions of Pure Lipids in Model Membranes and Their Modifications by Membrane Proteins. In *Lipid-protein interactions*, Jost, P. C.; Griffith, O. H., Eds. John Wiley & Sons: New York, 1982; Vol. 2, pp 239-281.
(165) Brooks, B. R.; Bruccoleri, R. E.; Olafson, B. D.; States, D. J.; Swaminathan, S.; Karplus, M. *J Comput Chem* **1983,** *4*, 187-217
(166) Phillips, J. C.; Braun, R.; Wang, W.; Gumbart, J.; Tajkhorshid, E.; Villa, E.; Chipot, C.; Skeel, R. D.; Kale, L.; Schulten, K. *J Comput Chem* **2005,** *26*, 1781-802
(167) Humphrey, W.; Dalke, A.; Schulten, K. *J Mol Graph* **1996,** *14*, 33-38
(168) Kucerka, N.; Tristram-Nagle, S.; Nagle, J. F. *J Membr Biol* **2005,** *208*, 193-202
(169) Pan, J.; Tristram-Nagle, S.; Kucerka, N.; Nagle, J. F. *Biophys J* **2008,** *94*, 117-24
(170) Marrink, S. J.; de Vries, A. H.; Mark, A. E. *J Phys Chem B* **2004,** *108*, 750-760
(171) Feller, S. E. *Curr Opin Colloid Interface Sci* **2000,** *5*, 217-223
(172) Hub, J. S.; Salditt, T.; Rheinstadter, M. C.; de Groot, B. L. *Biophys J* **2007,** *93*, 3156-68
(173) Benz, R. W.; Castro-Roman, F.; Tobias, D. J.; White, S. H. *Biophys J* **2005,** *88*, 805-17
(174) Scott, H. L. *Curr Opin Struct Biol* **2002,** *12*, 495-502
(175) Feller, S. E.; Pastor, R. W. *J Chem Phys* **1999,** *111*, 1281-1287
(176) Maxfield, F. R.; Tabas, I. *Nature* **2005,** *438*, 612-21
(177) Munro, S. *Cell* **2003,** *115*, 377-88

(178) Simons, K.; Toomre, D. *Nat Rev Mol Cell Biol* **2000,** *1*, 31-9
(179) Xu, X.; London, E. *Biochemistry* **2000,** *39*, 843-9
(180) Xu, X.; Bittman, R.; Duportail, G.; Heissler, D.; Vilcheze, C.; London, E. *J Biol Chem* **2001,** *276*, 33540-6
(181) Wang, J.; Megha; London, E. *Biochemistry* **2004,** *43*, 1010-8
(182) Stottrup, B. L.; Keller, S. L. *Biophys J* **2006,** *90*, 3176-83
(183) Megha; Bakht, O.; London, E. *J Biol Chem* **2006,** *281*, 21903-13
(184) Li, X. M.; Momsen, M. M.; Brockman, H. L.; Brown, R. E. *Biophys J* **2003,** *85*, 3788-801
(185) Bloch, K. E. *CRC Crit Rev Biochem* **1983,** *14*, 47-92
(186) Wenz, J. J.; Barrantes, F. J. *Biochemistry* **2003,** *42*, 14267-76
(187) Slotte, J. P. *Biochim Biophys Acta* **1995,** *1237*, 127-34
(188) Beattie, M. E.; Veatch, S. L.; Stottrup, B. L.; Keller, S. L. *Biophys J* **2005,** *89*, 1760-8
(189) Bacia, K.; Schwille, P.; Kurzchalia, T. *Proc Natl Acad Sci U S A* **2005,** *102*, 3272-7
(190) Rebolj, K.; Ulrih, N. P.; Macek, P.; Sepcic, K. *Biochim Biophys Acta* **2006,** *1758*, 1662-70
(191) Caldinelli, L.; Iametti, S.; Barbiroli, A.; Bonomi, F.; Fessas, D.; Molla, G.; Pilone, M. S.; Pollegioni, L. *J Biol Chem* **2005,** *280*, 22572-81
(192) Ben-Yashar, V.; Barenholz, Y. *Biochim Biophys Acta* **1989,** *985*, 271-8
(193) Rog, T.; Pasenkiewicz-Gierula, M.; Vattulainen, I.; Karttunen, M. *Biochim Biophys Acta* **2009,** *1788*, 97-121
(194) Olsen, B. N.; Schlesinger, P. H.; Baker, N. A. *J Am Chem Soc* **2009,** *131*, 4854-65
(195) Risselada, H. J.; Marrink, S. J. *Proc Natl Acad Sci U S A* **2008,** *105*, 17367-72
(196) Rog, T.; Stimson, L. M.; Pasenkiewicz-Gierula, M.; Vattulainen, I.; Karttunen, M. *J Phys Chem B* **2008,** *112*, 1946-52
(197) Murari, R.; Murari, M. P.; Baumann, W. J. *Biochemistry* **1986,** *25*, 1062-7
(198) Aittoniemi, J.; Rog, T.; Niemela, P.; Pasenkiewicz-Gierula, M.; Karttunen, M.; Vattulainen, I. *J Phys Chem B* **2006,** *110*, 25562-4
(199) Brown, D. A. *Physiology (Bethesda)* **2006,** *21*, 430-9
(200) Anderson, R. G.; Jacobson, K. *Science* **2002,** *296*, 1821-5
(201) Lucero, H. A.; Robbins, P. W. *Arch Biochem Biophys* **2004,** *426*, 208-24
(202) Ahmed, S. N.; Brown, D. A.; London, E. *Biochemistry* **1997,** *36*, 10944-53
(203) Hunt, G. R.; Tipping, L. R. *Biochim Biophys Acta* **1978,** *507*, 242-61
(204) Schmidt, C. F.; Barenholz, Y.; Huang, C.; Thompson, T. E. *Nature* **1978,** *271*, 775-7
(205) Sillerud, L. O.; Barnett, R. E. *Biochemistry* **1982,** *21*, 1756-60
(206) Daleke, D. L. *J Lipid Res* **2003,** *44*, 233-42
(207) Almeida, P. F.; Vaz, W. L.; Thompson, T. E. *Biochemistry* **1992,** *31*, 7198-210
(208) May, S. *Soft Matter* **2009,** *5*, 3148-3156
(209) Wagner, A. J.; Loew, S.; May, S. *Biophys J* **2007,** *93*, 4268-77
(210) Allender, D. W.; Schick, M. *Biophys J* **2006,** *91*, 2928-35
(211) Khanna, K.; Chang, T. T.; Kindt, J. T. *J Chem Phys* **2006,** *124*, 036102
(212) Stevens, M. J. *J Am Chem Soc* **2005,** *127*, 15330-1
(213) Collins, M. D. *Biophys J* **2008,** *94*, L32-4

(214) Gurtovenko, A. A. *J Chem Phys* **2005,** *122*, 244902
(215) Lee, S. J.; Song, Y.; Baker, N. A. *Biophys J* **2008,** *94*, 3565-76
(216) Sachs, J. N.; Crozier, P. S.; Woolf, T. B. *J Chem Phys* **2004,** *121*, 10847-51
(217) Denning, E. J.; Crozier, P. S.; Sachs, J. N.; Woolf, T. B. *Mol Membr Biol* **2009,** *26*, 397-421
(218) Cascales, J. J. L.; Otero, T. F.; Smith, B. D.; Gonzalez, C.; Marquez, M. *J Phys Chem B* **2006,** *110*, 2358-2363
(219) Bhide, S. Y.; Zhang, Z.; Berkowitz, M. L. *Biophys J* **2007,** *92*, 1284-95
(220) Vacha, R.; Berkowitz, M. L.; Jungwirth, P. *Biophys J* **2009,** *96*, 4493-501
(221) Porasso, R. D.; Cascales, J. J. L. *Colloids Surf., B* **2009,** *73*, 42-50
(222) Gurtovenko, A. A.; Vattulainen, I. *J Am Chem Soc* **2007,** *129*, 5358-9
(223) Gurtovenko, A. A.; Vattulainen, I. *J Phys Chem B* **2008,** *112*, 4629-34
(224) Esteban-Martin, S.; Risselada, H. J.; Salgado, J.; Marrink, S. J. *J Am Chem Soc* **2009,** *131*, 15194-202
(225) Bennum, S. V.; Longo, M. L.; Faller, R. *Langmuir* **2007,** *23*, 12465-12468
(226) Xing, C.; Faller, R. *J Phys Chem B* **2008,** *112*, 7086-94
(227) Sankaram, M. B.; Thompson, T. E. *Biochemistry* **1990,** *29*, 10676-84
(228) Sheetz, M. P.; Singer, S. J. *Proc Natl Acad Sci U S A* **1974,** *71*, 4457-61
(229) Pautot, S.; Frisken, B. J.; Weitz, D. A. *Proc Natl Acad Sci U S A* **2003,** *100*, 10718-21
(230) Hess, B.; Kutzer, C.; Van Der Spoel, D.; Lindahl, E. *J Chem Theory Comput* **2008,** *4*, 435-447
(231) Siwko, M. E.; Marrink, S. J.; de Vries, A. H.; Kozubek, A.; Schoot Uiterkamp, A. J.; Mark, A. E. *Biochim Biophys Acta* **2007,** *1768*, 198-206
(232) Klauda, J. B.; Roberts, M. F.; Redfield, A. G.; Brooks, B. R.; Pastor, R. W. *Biophys J* **2008,** *94*, 3074-83
(233) McIntosh, T. J. *Biochim Biophys Acta* **1978,** *513*, 43-58
(234) Levine, Y. K.; Wilkins, M. H. *Nat New Biol* **1971,** *230*, 69-72
(235) Pan, J.; Tristram-Nagle, S.; Nagle, J. F. *Phys Rev E Stat Nonlin Soft Matter Phys* **2009,** *80*, 021931
(236) Pandit, S. A.; Vasudevan, S.; Chiu, S. W.; Mashl, R. J.; Jakobsson, E.; Scott, H. L. *Biophys J* **2004,** *87*, 1092-100
(237) Lindahl, E.; Edholm, O. *Biophys J* **2000,** *79*, 426-33
(238) Thurmond, R. L.; Lindblom, G.; Brown, M. F. *Biochemistry* **1993,** *32*, 5394-410
(239) Mills, T. T.; Tristram-Nagle, S.; Heberle, F. A.; Morales, N. F.; Zhao, J.; Wu, J.; Toombes, G. E.; Nagle, J. F.; Feigenson, G. W. *Biophys J* **2008,** *95*, 682-90
(240) Mills, T. T.; Huang, J.; Feigenson, G. W.; Nagle, J. F. *General Physiology and Biophysics* **2009,** *28*, 126-39
(241) Zhang, J.; Jing, B.; Tokutake, N.; Regen, S. L. *J Am Chem Soc* **2004,** *126*, 10856-7
(242) Zhang, J.; Jing, B.; Tokutake, N.; Regen, S. L. *Biochemistry* **2005,** *44*, 3598-603
(243) Roux, A.; Cuvelier, D.; Nassoy, P.; Prost, J.; Bassereau, P.; Goud, B. *Embo J* **2005,** *24*, 1537-45
(244) Baumgart, T.; Das, S.; Webb, W. W.; Jenkins, J. T. *Biophys J* **2005,** *89*, 1067-80
(245) Heinrich, M.; Tian, A.; Esposito, C.; Baumgart, T. *Proc Natl Acad Sci U S A* **2010,** *107*, 7208-13

(246) McMahon, H. T.; Gallop, J. L. *Nature* **2005,** *438*, 590-6
(247) Tian, A.; Baumgart, T. *Biophys J* **2009,** *96*, 2676-88
(248) Huang, K. C.; Ramamurthi, K. S. *Mol Microbiol* **2010,** *76*, 822-832
(249) Brown, M. F. *Chem Phys Lipids* **1994,** *73*, 159-80
(250) Mukherjee, S.; Maxfield, F. R. *Traffic* **2000,** *1*, 203-11
(251) Spillantini, M. G.; Crowther, R. A.; Jakes, R.; Hasegawa, M.; Goedert, M. *Proc Natl Acad Sci U S A* **1998,** *95*, 6469-73
(252) Kruger, R.; Kuhn, W.; Muller, T.; Woitalla, D.; Graeber, M.; Kosel, S.; Przuntek, H.; Epplen, J. T.; Schols, L.; Riess, O. *Nat Genet* **1998,** *18*, 106-8
(253) Polymeropoulos, M. H.; Lavedan, C.; Leroy, E.; Ide, S. E.; Dehejia, A.; Dutra, A.; Pike, B.; Root, H.; Rubenstein, J.; Boyer, R.; Stenroos, E. S.; Chandrasekharappa, S.; Athanassiadou, A.; Papapetropoulos, T.; Johnson, W. G.; Lazzarini, A. M.; Duvoisin, R. C.; Di Iorio, G.; Golbe, L. I.; Nussbaum, R. L. *Science* **1997,** *276*, 2045-7
(254) Zarranz, J. J.; Alegre, J.; Gomez-Esteban, J. C.; Lezcano, E.; Ros, R.; Ampuero, I.; Vidal, L.; Hoenicka, J.; Rodriguez, O.; Atares, B.; Llorens, V.; Gomez Tortosa, E.; del Ser, T.; Munoz, D. G.; de Yebenes, J. G. *Ann Neurol* **2004,** *55*, 164-73
(255) Conway, K. A.; Lee, S. J.; Rochet, J. C.; Ding, T. T.; Williamson, R. E.; Lansbury, P. T., Jr. *Proc Natl Acad Sci U S A* **2000,** *97*, 571-6
(256) Wood, S. J.; Wypych, J.; Steavenson, S.; Louis, J. C.; Citron, M.; Biere, A. L. *J Biol Chem* **1999,** *274*, 19509-12
(257) Narhi, L.; Wood, S. J.; Steavenson, S.; Jiang, Y.; Wu, G. M.; Anafi, D.; Kaufman, S. A.; Martin, F.; Sitney, K.; Denis, P.; Louis, J. C.; Wypych, J.; Biere, A. L.; Citron, M. *J Biol Chem* **1999,** *274*, 9843-6
(258) Kubo, S.; Nemani, V. M.; Chalkley, R. J.; Anthony, M. D.; Hattori, N.; Mizuno, Y.; Edwards, R. H.; Fortin, D. L. *J Biol Chem* **2005,** *280*, 31664-72
(259) Bussell, R., Jr.; Eliezer, D. *Biochemistry* **2004,** *43*, 4810-8
(260) Ulmer, T. S.; Bax, A. *J Biol Chem* **2005,** *280*, 43179-87
(261) Cole, N. B.; Murphy, D. D.; Grider, T.; Rueter, S.; Brasaemle, D.; Nussbaum, R. L. *J Biol Chem* **2002,** *277*, 6344-52
(262) Jensen, P. H.; Nielsen, M. S.; Jakes, R.; Dotti, C. G.; Goedert, M. *J Biol Chem* **1998,** *273*, 26292-4
(263) Jo, E.; Fuller, N.; Rand, R. P.; St George-Hyslop, P.; Fraser, P. E. *J Mol Biol* **2002,** *315*, 799-807
(264) Kahle, P. J.; Neumann, M.; Ozmen, L.; Muller, V.; Jacobsen, H.; Schindzielorz, A.; Okochi, M.; Leimer, U.; van Der Putten, H.; Probst, A.; Kremmer, E.; Kretzschmar, H. A.; Haass, C. *J Neurosci* **2000,** *20*, 6365-73
(265) McLean, P. J.; Kawamata, H.; Ribich, S.; Hyman, B. T. *J Biol Chem* **2000,** *275*, 8812-6
(266) Perrin, R. J.; Woods, W. S.; Clayton, D. F.; George, J. M. *J Biol Chem* **2000,** *275*, 34393-8
(267) Outeiro, T. F.; Lindquist, S. *Science* **2003,** *302*, 1772-5
(268) Conway, K. A.; Harper, J. D.; Lansbury, P. T. *Nat Med* **1998,** *4*, 1318-20
(269) Barlow, D. J.; Thornton, J. M. *J Mol Biol* **1988,** *201*, 601-19
(270) Choi, W.; Zibaee, S.; Jakes, R.; Serpell, L. C.; Davletov, B.; Crowther, R. A.; Goedert, M. *FEBS Lett* **2004,** *576*, 363-8

(271) Fredenburg, R. A.; Rospigliosi, C.; Meray, R. K.; Kessler, J. C.; Lashuel, H. A.; Eliezer, D.; Lansbury, P. T., Jr. *Biochemistry* **2007,** *46*, 7107-18
(272) Irizarry, M. C.; Kim, T. W.; McNamara, M.; Tanzi, R. E.; George, J. M.; Clayton, D. F.; Hyman, B. T. *J Neuropathol Exp Neurol* **1996,** *55*, 889-95
(273) Maroteaux, L.; Campanelli, J. T.; Scheller, R. H. *J Neurosci* **1988,** *8*, 2804-15
(274) Lotharius, J.; Brundin, P. *Nat Rev Neurosci* **2002,** *3*, 932-42
(275) Chandra, S.; Chen, X.; Rizo, J.; Jahn, R.; Sudhof, T. C. *J Biol Chem* **2003,** *278*, 15313-8
(276) Davidson, W. S.; Jonas, A.; Clayton, D. F.; George, J. M. *J Biol Chem* **1998,** *273*, 9443-9
(277) Eliezer, D.; Kutluay, E.; Bussell, R., Jr.; Browne, G. *J Mol Biol* **2001,** *307*, 1061-73
(278) Bussell, R., Jr.; Eliezer, D. *J Mol Biol* **2003,** *329*, 763-78
(279) Ulmer, T. S.; Bax, A.; Cole, N. B.; Nussbaum, R. L. *J Biol Chem* **2005,** *280*, 9595-603
(280) Dedmon, M. M.; Lindorff-Larsen, K.; Christodoulou, J.; Vendruscolo, M.; Dobson, C. M. *J Am Chem Soc* **2005,** *127*, 476-7
(281) Mihajlovic, M.; Lazaridis, T. *Proteins* **2008,** *70*, 761-78
(282) Tsigelny, I. F.; Bar-On, P.; Sharikov, Y.; Crews, L.; Hashimoto, M.; Miller, M. A.; Keller, S. H.; Platoshyn, O.; Yuan, J. X.; Masliah, E. *Febs J* **2007,** *274*, 1862-77
(283) Bortolus, M.; Tombolato, F.; Tessari, I.; Bisaglia, M.; Mammi, S.; Bubacco, L.; Ferrarini, A.; Maniero, A. L. *J Am Chem Soc* **2008,** *130*, 6690-1
(284) Drescher, M.; Veldhuis, G.; van Rooijen, B. D.; Milikisyants, S.; Subramaniam, V.; Huber, M. *J Am Chem Soc* **2008,** *130*, 7796-7
(285) Frishman, D.; Argos, P. *Proteins* **1995,** *23*, 566-79
(286) Rueda, M.; Ferrer-Costa, C.; Meyer, T.; Perez, A.; Camps, J.; Hospital, A.; Gelpi, J. L.; Orozco, M. *Proc Natl Acad Sci U S A* **2007,** *104*, 796-801
(287) Ohkubo, Y. Z.; Tajkhorshid, E. *Structure* **2008,** *16*, 72-81
(288) Segrest, J. P.; Jackson, R. L.; Morrisett, J. D.; Gotto, A. M., Jr. *FEBS Lett* **1974,** *38*, 247-58
(289) Bussell, R., Jr.; Ramlall, T. F.; Eliezer, D. *Protein Sci* **2005,** *14*, 862-72
(290) Giasson, B. I.; Murray, I. V.; Trojanowski, J. Q.; Lee, V. M. *J Biol Chem* **2001,** *276*, 2380-6
(291) Iwai, A.; Yoshimoto, M.; Masliah, E.; Saitoh, T. *Biochemistry* **1995,** *34*, 10139-45
(292) Jao, C. C.; Der-Sarkissian, A.; Chen, J.; Langen, R. *Proc Natl Acad Sci U S A* **2004,** *101*, 8331-6
(293) Buck, M.; Bouguet-Bonnet, S.; Pastor, R. W.; MacKerell, A. D., Jr. *Biophys J* **2006,** *90*, L36-8
(294) Lee, H. J.; Choi, C.; Lee, S. J. *J Biol Chem* **2002,** *277*, 671-8
(295) Zhu, M.; Li, J.; Fink, A. L. *J Biol Chem* **2003,** *278*, 40186-97
(296) Narayanan, V.; Scarlata, S. *Biochemistry* **2001,** *40*, 9927-34
(297) Sachs, J. N.; Engelman, D. M. *Annu Rev Biochem* **2006,** *75*, 707-12
(298) Martens, S.; Kozlov, M. M.; McMahon, H. T. *Science* **2007,** *316*, 1205-8
(299) Pitman, M. C.; Suits, F.; Mackerell, A. D., Jr.; Feller, S. E. *Biochemistry* **2004,** *43*, 15318-28
(300) Leontiadou, H.; Mark, A. E.; Marrink, S. J. *Biophys J* **2004,** *86*, 2156-64

(301) Tarek, M. *Biophys J* **2005,** *88*, 4045-53
(302) Garg, G.; Hassan, P. A.; Aswal, V. K.; Kulshreshtha, S. K. *J Phys Chem B* **2005,** *109*, 1340-6
(303) White, S. H. *Protein Sci* **2004,** *13*, 1948-9
(304) Granseth, E.; Seppala, S.; Rapp, M.; Daley, D. O.; Von Heijne, G. *Mol Membr Biol* **2007,** *24*, 329-32
(305) Bowie, J. U. *Nature* **2005,** *438*, 581-9
(306) Garavito, R. M.; Ferguson-Miller, S. *J Biol Chem* **2001,** *276*, 32403-6
(307) Gohon, Y.; Popot, J.-L. *Curr Opin Colloid Interface Sci* **2003,** *8*, 15-22
(308) Popot, J.-L. *Annu Rev Biochem* **2010,** *79*, 737-75
(309) Tribet, C.; Audebert, R.; Popot, J.-L. *Proc Natl Acad Sci U S A* **1996,** *93*, 15047-50
(310) Popot, J.-L.; Berry, E. A.; Charvolin, D.; Creuzenet, C.; Ebel, C.; Engelman, D. M.; Flötenmeyer, M.; Giusti, F.; Gohon, Y.; Hervé, P.; Hong, Q.; Lakey, J. H.; Leonard, K.; Shuman, H. A.; Timmins, P.; Warschawski, D. E.; Zito, F.; Zoonens, M.; Pucci, B.; Tribet, C. *Cell Mol Life Sci* **2003,** *60*, 1559-74
(311) Sanders, C. R.; Kuhn Hoffmann, A.; Gray, D. N.; Keyes, M. H.; Ellis, C. D. *Chembiochem* **2004,** *5*, 423-6
(312) Popot, J.-L.; Althoff, T.; Bagnard, D.; Banères, J.-L.; Bazzacco, P.; Billon-Denis, E.; Catoire, L. J.; Champeil, P.; Charvolin, D.; Cocco, M. J.; Crémel, G.; Dahmane, T.; de la Maza, L. M.; Ebel, C.; Gabel, F.; Giusti, F.; Gohon, Y.; Goormaghtigh, E.; Guittet, E.; Kleinschmidt, J. H.; Kühlbrandt, W.; Le Bon, C.; Martinez, K. L.; Picard, M.; Pucci, B.; Sachs, J. N.; Tribet, C.; van Heijenoort, C.; Wien, F.; Zito, F.; Zoonens, M. *Annu Rev Biophys* **2011,** *40*, 379-408
(313) Banères, J.-L.; Popot, J.-L.; Mouillac, B. *Trends Biotechnol* **2011**,
(314) Dahmane, T.; Damian, M.; Mary, S.; Popot, J.-L.; Banères, J.-L. *Biochemistry* **2009,** *48*, 6516-21
(315) Pocanschi, C. L.; Dahmane, T.; Gohon, Y.; Rappaport, F.; Apell, H.-J.; Kleinschmidt, J. H.; Popot, J.-L. *Biochemistry* **2006,** *45*, 13954-61
(316) Charvolin, D.; Perez, J.-B.; Rouvière, F.; Giusti, F.; Bazzacco, P.; Abdine, A.; Rappaport, F.; Martinez, K. L.; Popot, J.-L. *Proc Natl Acad Sci U S A* **2009,** *106*, 405-10
(317) Gohon, Y.; Dahmane, T.; Ruigrok, R. W.; Schuck, P.; Charvolin, D.; Rappaport, F.; Timmins, P.; Engelman, D. M.; Tribet, C.; Popot, J.-L.; Ebel, C. *Biophys J* **2008,** *94*, 3523-37
(318) Gohon, Y.; Giusti, F.; Prata, C.; Charvolin, D.; Timmins, P.; Ebel, C.; Tribet, C.; Popot, J.-L. *Langmuir* **2006,** *22*, 1281-90
(319) Gohon, Y.; Pavlov, G.; Timmins, P.; Tribet, C.; Popot, J.-L.; Ebel, C. *Anal Biochem* **2004,** *334*, 318-34
(320) Zoonens, M.; Giusti, F.; Zito, F.; Popot, J.-L. *Biochemistry* **2007,** *46*, 10392-404
(321) Flötenmeyer, M.; Weiss, H.; Tribet, C.; Popot, J.-L.; Leonard, K. *J Microsc* **2007,** *227*, 229-35
(322) Tifrea, D. F.; Sun, G.; Pal, S.; Zardeneta, G.; Cocco, M. J.; Popot, J.-L.; de la Maza, L. M. *Vaccine* **2011**,
(323) Catoire, L. J.; Damian, M.; Giusti, F.; Martin, A.; van Heijenoort, C.; Popot, J.-L.; Guittet, E.; Banères, J.-L. *J Am Chem Soc* **2010,** *132*, 9049-57

(324) Zoonens, M.; Catoire, L. J.; Giusti, F.; Popot, J.-L. *Proc Natl Acad Sci U S A* **2005,** *102*, 8893-8
(325) Raschle, T.; Hiller, S.; Etzkorn, M.; Wagner, G. *Curr Opin Struct Biol* **2010,** *20*, 471-9
(326) Catoire, L. J.; Zoonens, M.; van Heijenoort, C.; Giusti, F.; Guittet, E.; Popot, J.-L. *Eur Biophys J* **2009**,
(327) Catoire, L. J.; Zoonens, M.; van Heijenoort, C.; Giusti, F.; Popot, J.-L.; Guittet, E. *J Magn Reson* **2009,** *197*, 91-5
(328) Nagy, J. K.; Kuhn Hoffmann, A.; Keyes, M. H.; Gray, D. N.; Oxenoid, K.; Sanders, C. R. *FEBS Lett* **2001,** *501*, 115-20
(329) Diab, C.; Tribet, C.; Gohon, Y.; Popot, J.-L.; Winnik, F. M. *Biochim Biophys Acta* **2007,** *1768*, 2737-47
(330) Diab, C.; Winnik, F. M.; Tribet, C. *Langmuir* **2007,** *23*, 3025-35
(331) Sharma, K. S.; Durand, G.; Giusti, F.; Olivier, B.; Fabiano, A. S.; Bazzacco, P.; Dahmane, T.; Ebel, C.; Popot, J.-L.; Pucci, B. *Langmuir* **2008,** *24*, 13581-90
(332) Bazzacco, P.; Sharma, K. S.; Durand, G.; Giusti, F.; Ebel, C.; Popot, J.-L.; Pucci, B. *Biomacromolecules* **2009,** *10*, 3317-26
(333) Dahmane, T.; Giusti, F.; Catoire, L. J.; Popot, J.-L. *Biopolymers, in the press.* **2011**,
(334) Tribet, C.; Audebert, R.; Popot, J.-L. *Langmuir* **1997,** *13*, 5570-5576
(335) Picard, M.; Dahmane, T.; Garrigos, M.; Gauron, C.; Giusti, F.; le Maire, M.; Popot, J.-L.; Champeil, P. *Biochemistry* **2006,** *45*, 1861-9
(336) Champeil, P.; Menguy, T.; Tribet, C.; Popot, J.-L.; le Maire, M. *J Biol Chem* **2000,** *275*, 18623-37
(337) Karplus, M.; Kuriyan, J. *Proc Natl Acad Sci U S A* **2005,** *102*, 6679-85
(338) Klepeis, J. L.; Lindorff-Larsen, K.; Dror, R. O.; Shaw, D. E. *Curr Opin Struct Biol* **2009,** *19*, 120-7
(339) Tieleman, D. P.; Marrink, S. J.; Berendsen, H. J. *Biochim Biophys Acta* **1997,** *1331*, 235-70
(340) Ash, W. L.; Zlomislic, M. R.; Oloo, E. O.; Tieleman, D. P. *Biochim Biophys Acta* **2004,** *1666*, 158-89
(341) Gumbart, J.; Wang, Y.; Aksimentiev, A.; Tajkhorshid, E.; Schulten, K. *Curr Opin Struct Biol* **2005,** *15*, 423-31
(342) Reddy, G.; Yethiraj, A. *J Chem Phys* **2010,** *132*, 074903
(343) Lee, H.; Venable, R. M.; Mackerell, A. D., Jr.; Pastor, R. W. *Biophys J* **2008,** *95*, 1590-9
(344) Lee, H.; de Vries, A. H.; Marrink, S. J.; Pastor, R. W. *J Phys Chem B* **2009,** *113*, 13186-94
(345) Srinivas, G.; Discher, D. E.; Klein, M. L. *Nat Mater* **2004,** *3*, 638-44
(346) Monticelli, L.; Kandasamy, S.; Periole, X.; Larson, R.; Tieleman, D.; Marrink, S. *J Chem Theory and Comput* **2008,** *4*, 819-834
(347) Ainalem, M. L.; Campbell, R. A.; Khalid, S.; Gillams, R. J.; Rennie, A. R.; Nylander, T. *J Phys Chem B* **2010,** *114*, 7229-44
(348) Peng, L. X.; Ivetac, A.; Chaudhari, A. S.; Van, S.; Zhao, G.; Yu, L.; Howell, S. B.; McCammon, J. A.; Gough, D. A. *Biopolymers* **2010,** *93*, 936-51

(349) Rossi, G.; Monticelli, L.; Puisto, S. R.; Vattulainen, I.; Ala-Nissila, T. *Soft Matter* **2011,** *7*, 698-708
(350) Fredrickson, G. H.; Milner, S. T. *Phys Rev Lett* **1991,** *67*, 835-838
(351) MacKerell Jr., A. D.; Bashford, D.; Bellott, M.; Dunbrack, R. L.; Evanseck, J. D.; Field, M. J.; Fischer, S.; Gao, J.; Guo, H.; Ha, S.; Joseph-McCarthy, D.; Kuchnir, L.; Kuczera, K.; Lau, F. T. K.; Mattos, C.; Michnick, S.; Ngo, T.; Nguyen, D. T.; Prodhom, B.; Reiher III, W. E.; Roux, B.; Schlenkrich, M.; Smith, J. C.; Stote, R.; Straub, J.; Watanabe, M.; Wiorkiewicz-Kuczera, J.; Yin, D.; Karplus, M. *J Phys Chem B* **1998,** *102*, 3586-3616
(352) Becke, A. D. *J Chem Phys* **1993,** *98*, 5648-5653
(353) Jorgensen, W. L.; Chandrasekhar, J.; Madura, J. D.; Impey, R. W.; Klein, M. L. *J Chem Phys* **1983,** *79*, 926-935
(354) Feller, S. E.; Zhang, Y.; Pastor, R. W.; Brooks, B. R. *J Chem Phys* **1995,** *103*, 4613-4621
(355) Essman, U.; Perera, L.; Berkowitz, M. L.; Darden, T.; Lee, H.; Pederson, L. A. *J Chem Phys* **1995,** *103*, 8577-8593
(356) Andersen, H. C. *J Comp Phys* **1983,** *52*, 24-34
(357) Lopez, C. A.; Rzepiela, A. J.; De Vries, A. H.; Dijkhuizen, L.; Hunenberger, P. H.; Marrink, S. J. *J Chem Theory Comput* **2009,** *5*, 3195-2310
(358) Khalid, S.; Bond, P. J.; Holyoake, J.; Hawtin, R. W.; Sansom, M. S. *J R Soc Interface* **2008,** *5 Suppl 3*, S241-50
(359) Gautieri, A.; Russo, A.; Vesentini, S.; Redaelli, A.; Buehler, M. J. *J Chem Theory Comput* **2010,** *6*, 1210-1218
(360) Kirkwood, J. G. *J Chem Phys* **1935,** *3*, 300-313
(361) Lyubartsev, A. P.; Jacobsson, S. P.; Sundholm, G.; Laaksonen, A. *J Phys Chem B* **2001,** *105*, 7775–7782
(362) Svergun, D. I.; Richard, S.; Koch, M. H.; Sayers, Z.; Kuprin, S.; Zaccai, G. *Proc Natl Acad Sci U S A* **1998,** *95*, 2267-72
(363) Gohon, Y.; Giusti, F.; Prata, C.; Charvolin, D.; Timmins, P.; Ebel, C.; Tribet, C.; Popot, J. L. *Langmuir* **2006,** *22*, 1281-90
(364) Guinier, A.; Fournet, G., *Small-angle scattering of X-rays*. Wiley: New York, 1955; p 268.
(365) Liu, R. C. W.; Pallier, A.; Brestaz, M.; Pantoustier, N.; Tribet, C. *Macromolecules* **2007,** *40*, 4276-4286
(366) Gohon, Y. Etude des interactions entre un analogue du fragment transmembranaire de la glycophorine et des polymeres amphiphiles: les amphipols. Univ. Paris VI, Paris, 1996.
(367) Martinez, K. L.; Gohon, Y.; Corringer, P.-J.; Tribet, C.; Merola, F.; Changeux, J. P.; Popot, J.-L. *FEBS Lett* **2002,** *528*, 251-6
(368) Ladaviere, C.; Toustou, M.; Gulik-Krzywicki, T.; Tribet, C. *J Colloid Interface Sci* **2001,** *241*, 178-187
(369) Ladaviere, C.; Tribet, C.; Cribier, S. *Langmuir* **2002,** *18*, 7320-7327